

NUMERICAL STUDY OF MECHANICAL BEHAVIOUR OF
TUBULAR STRUCTURES UNDER STATIC AND DYNAMIC
COMPRESSION

NUMERICAL STUDY OF MECHANICAL BEHAVIOUR OF TUBULAR
STRUCTURES UNDER STATIC AND DYNAMIC COMPRESSION

By Amir Partovi

A Thesis

Submitted to the School of Graduate Studies

In Partial Fulfillment of the Requirements

For the Degree

Master of Applied Science

McMaster University

© Copyright by Amir Partovi, May 2019

Master of Applied Science
(Mechanical Engineering)

McMaster University
Hamilton, Ontario

TITLE: Numerical Study of Mechanical Behaviour of Tubular
Structures Under Static and Dynamic Compression

AUTHOR: Amir Partovi

SUPERVISOR: Professor Peidong Wu

NUMBER OF PAGES: xii, 114

ABSTRACT

Finite element analysis (FEA) is a tool used to predict responses, reproduce experiments, and improve the performance of devices. Modern production techniques, such as 3D printing, enable researchers to investigate structures with complicated shapes and made of mixed materials, thereby increasing the application of simulation and FEA. In this thesis, finite element package ABAQUS is used to numerically investigate the behavior of components subjected to axial static and dynamic loadings.

The effect of cladding a ductile material during ring compression test and energy absorption (EA) of circular tubes is evaluated. The addition of layers of a ductile material to the cross section of a ring increases its compressibility. The EA of circular tubes is improved when the layers of a soft material are located in the model.

Rings with various geometric ratios and shape factors are subjected to axial static loading. The calibration curves for different friction coefficients are plotted. The behavior of the rings and their calibration curves are predictable when the geometric ratio and shape factor of the models are the same. For the rings with the same shape factor but different geometric ratios, the calibration curves can be located lower or higher in the diagram regardless of their size.

The application of hydrostatic pressure to the inner and outer walls of a ring increases its compressibility by changing the tangential and radial stress distributions. Cladding the outer wall of a ring with a soft material changes the stress distribution and increases

compressibility. The state of radial stress is easier to change from tensile to compressive in comparison with tangential stress.

The force–displacement diagrams of corrugated tubes with different number of grooves and groove sizes are divided into three parts. The optimum model that shows the best performance has the same area under the curve of each part. The grooves as triggers can control the location and value of the peak force in the diagram. The size and shape of these triggers should be optimized. The model with regular fluctuations and without any peak force can be considered the optimum model.

The addition of layers of a ductile material to the base model improves the crashworthiness of structures. The volume fraction of clad material and its location should be optimized. For the circular tubes as energy absorbers, the addition of some layers at a 45° angle increases EA and crush force efficiency.

ACKNOWLEDGEMENTS

I would like to express my great appreciation toward my supervisor Dr. Wu for his support, patience and helpful suggestions. The door to his office was always open whenever I needed his valuable advice. I would also like to thank him for his financial support and giving me this opportunity.

I would also like to thank Dr. Lightstone for her kind guidance and support during my master's studies. Without her support I could not finish this program.

Furthermore, I would like to thank Dr. Bruhis for his encouragement. His kind advice and guidance are highly appreciated. Working with him was a pleasure.

Many thanks to my professors, office staff at the Department of Mechanical Engineering and my friends at McMaster University especially Mehdi Shahzamanian.

Last but not least, special thanks to my wife, Shabnam, and my son, Arshia, for their patience and continuous encouragement. This accomplishment would not have been possible without them.

TABLE OF CONTENTS

ABSTRACT.....	iii
ACKNOWLEDGEMENT	v
TABLE OF CONTENTS.....	vi
LIST OF FIGURES	viii
LIST OF TABLES.....	xii
Chapter 1 Introduction	1
1.1 Dynamic loading and impact test.....	1
1.1.1 Importance of energy absorbers in vehicles.....	1
1.1.2 EA systems.....	2
1.1.3 Design parameters of energy absorbers	2
1.1.4 Thin-walled structures as energy absorbers	4
1.1.5 Production of thin-walled tubes	5
1.2 Static loading and ring compression test.....	7
1.3 Thesis outline	8
Chapter 2 Literature review	11
2.1. Dynamic loading and energy absorbers	11
2.1.1 Circular thin-walled tubes as energy absorbers.....	12
2.1.2 Deformation modes in circular tubes	12
2.1.3 Average force in static loading	16
2.1.4. Other tube shapes as energy absorbers.....	18
2.1.5 Effects of strain-rate and strain hardening parameter	19
2.1.6 Miscellaneous topics	22
2.2. Ring compression test	23
2.3. Conclusion	29
Chapter 3 Static axial compression of rings.....	31
3.1 Introduction.....	31
3.2 FE configuration of ring compression test.....	31
3.3 Effect of shape factor on ring compression test.....	34
3.4 Calibration curves for determining the friction coefficient.....	39
3.5 Effect of geometry on calibration curves	41
3.6 Effects of material and test parameters	44

3.6.1 Effect of strain hardening parameter.....	46
3.6.2 Effect of strain rate sensitivity parameter	47
3.6.3 Effect of temperature	49
3.7 Effect of hydrostatic pressure on deformation mechanism of the ring	50
3.8 Conclusion	53
Chapter 4 Thin-walled tubes under dynamic axial loading	55
4.1 Introduction.....	55
4.2 FE configuration of the base model in ABAQUS.....	57
4.2.1 Verification of simulation process in ABAQUS.....	57
4.2.2 Selection of base circular model for FEA.....	61
4.3 Effects of test conditions.....	63
4.3.1 Effect of coefficient of friction	63
4.3.2 Effects of test speed and mass.....	65
4.3.3 Effect of temperature	67
4.4 Effects of material properties	68
4.4.1 Strain rate sensitivity.....	68
4.4.2 Strain hardening	72
4.4.3 Temperature exponent.....	73
4.5 Effect of geometry	74
4.5.1 Number of tubes.....	74
4.5.2 Corrugated samples.....	78
4.6 Conclusion	87
Chapter 5 Effects of composite materials on the response of rings and thin-walled tubes.....	89
5.1 Introduction.....	89
5.2 Effect of ductile layer on the f-d curve of compressed rings	90
5.3 Effect of cladding on EA	95
5.3.1 Simple circular tubes.....	95
5.3.2 Supported circular tubes.....	99
5.3.3 Circular tubes with oriented ductile layers.....	102
5.4 Conclusion	105
Chapter 6 Conclusions	107
Bibliography	109

LIST OF FIGURES

Figure 1.1: Energy absorbers and occupant compartment in a passenger car [Tarlochan et al., 2013].	2
Figure 1.2: Typical f–d curve of an energy absorber [Guillow et al., 2001].....	4
Figure 1.3: Thin-walled components in a typical unibody structure of a car [http:// www. Naaamap . com].	5
Figure 1.4: HSS welding manufacturing methods: (a) rolling and electric resistance welding; (b) form-square weld-square process [http://www.cim.mcgill.ca].	6
Figure 2.1: Common modes of deformation in circular tubes: (a) concertina mode (axisymmetric); (b) and (c) diamond mode (non-axisymmetric) [Abramowicz et al., 1984a].	14
Figure 2.2: Simulations of circular tubes with different L/D ratios and impact velocities [Karagiozova et al., 2008].....	15
Figure 3.1: Typical ring compression system in ABAQUS.....	32
Figure 3.2: (a) Swapping diagonals of the upper half of CAX3 elements to obtain symmetry; (b) comparison of CAX8R and CAX8 elements with approximately 1% difference.....	32
Figure 3.3: Effect of element aspect ratio on deformation: aspect ratio (β) (a) = 1; (b) = 1.5; (c) = 2; (d) = 3.....	33
Figure 3.4: Mesh convergence study.	33
Figure 3.5: Definition of shape factor.....	34
Figure 3.6: F–d curves for different shape factors.	35
Figure 3.7: Proportioned f–d curves for different shape factors.	36
Figure 3.8: F–d curves for different geometries with the same shape factor.	37
Figure 3.9: (a) Force versus reduction in height, and (b) proportioned force with volume versus displacement for the three cases.....	38
Figure 3.10: Deformation modes of (a) Case I (OD:ID:H ratio of 20:4:16 mm), (b) Case II (OD:ID:H ratio of 20:8:12 mm), and (c) Case III (OD:ID:H ratio of 20:12:8 mm). ...	38
Figure 3.11: Calibration curves for determining the friction coefficient.	40
Figure 3.12: Similarity of ring compression and uniaxial tensile tests with friction coefficient of zero.....	41
Figure 3.13: Calibration curves for different rings with the same shape factor of $\lambda = 2$	42
Figure 3.14: Calibration curves for different rings with the same geometric ratio (6:3:2).	43

Figure 3.15: Effect of friction on f–d diagrams for the 17:7.5:5 mm (OD:ID:H) model.....	44
Figure 3.16: Comparison of results in ABAQUS/Standard and Explicit.....	45
Figure 3.17: Comparison of (a) the result of experiment from a paper [Hartley et al., 1981] with (b) the result of simulation for the verification of procedure in ABAQUS.	46
Figure 3.18: Effect of strain hardening on (a) stress–strain and (b) f–d curves.....	46
Figure 3.19: Effect of strain rate sensitivity on stress-strain curves.	47
Figure 3.20: Effect of strain rate sensitivity on f–d curves.	48
Figure 3.21: Effect of velocity on f–d curves for $C = 0.500$	48
Figure 3.22: Effect of working temperature on (a) stress–strain and (b) f–d curves.	49
Figure 3.23: Effect of hydrostatic pressure on plastic strain localization.	51
Figure 3.24: Plastic strain localization of more than 40%: (a) $P_i = 0, P_o = 0$; (b) $P_i = 0, P_o = 300$ MPa; (c) $P_i = 300$ MPa, $P_o = 0$; (d) $P_i = 500$ MPa, $P_o = 0$	52
Figure 3.25: Distribution of radial stress; compressive stress in grey, and tensile stress in yellow.	52
Figure 3.26: Distribution of tangential stress; compressive stress in grey, and tensile stress in yellow.....	53
Figure 4.1: Typical f–d diagram [Tarlochan et al., 2013].	55
Figure 4.2: Typical FE model in ABAQUS for axial impact test.	58
Figure 4.3: Comparison of (a) the result of FEA from a paper [Tarlochan et al., 2013] with (b) the result of simulation for the verification of procedure in ABAQUS.	59
Figure 4.4: F–d diagrams for perimeter of 400 mm and lengths of (a) $L = 225\text{--}300$ mm and (b) $L = 325\text{--}400$ mm.	62
Figure 4.5: Mesh convergence study based on EA.	63
Figure 4.6: Mesh convergence study based on peak force.....	63
Figure 4.7: Mesh convergence study based on computation time.	63
Figure 4.8: Effect of friction coefficient on P400-L350; (a) $f = 0.0$, (b) $f = 0.2$, (c) $f = 0.4$	64
Figure 4.9: F–d diagrams for P400-L350 model with different friction coefficients defined in the contact property.	64
Figure 4.10: Effects of test speed and mass on the crushing behavior of circular tubes; (a) f–d diagrams; (b)–(d) deformation modes for $V\uparrow\text{--}M\downarrow$, $V0\text{--}M0$ (base model), and $V\downarrow\text{--}M\uparrow$, respectively.	66

Figure 4.11: Effect of temperature on the crushing behavior of circular tubes; (a) f–d diagrams; (b) T = 20 °C (base model); (c) T = 50 °C; and (d) T = 100 °C.	67
Figure 4.12: Formation of concertina modes at the bottom of the model at the initial stages of deformation under high temperatures (time frame = 50).	68
Figure 4.13: EA capacity versus strain rate sensitivity at different initial velocities.	70
Figure 4.14: Effect of strain rate sensitivity with initial velocities of (a) 11.0 m/s, (b) 15.6 m/s, and (c) 31.2 m/s; (d) deformation modes.	71
Figure 4.15: F–d diagrams for investigating the effect of strain hardening parameter.	72
Figure 4.16: Effect of strain hardening parameter on (a) CFE and (b) EA.	73
Figure 4.17: Effect of temperature exponent on (a) CFE, and (b) energy absorption.	74
Figure 4.18: EA for multiple tubes with different distances of r, 2r, and 5r.	75
Figure 4.19: Deformation patterns of two tubes with different distances of (a) r, (b) 2r, and (c) 5r.	76
Figure 4.20: Effect of number of tubes on the crashworthiness of the base model.	76
Figure 4.21: Deformation pattern of quadruple tubes with distances of 4r and r/2 at different time frames.	77
Figure 4.22: Corrugated tubes. (a) D3C8 model with 8 grooves of 3 mm; (b) meshing of grooves with sections.	78
Figure 4.23: EA at different stages of deformation.	79
Figure 4.24: Deformation pattern of corrugated tubes. From left to right: D1C1, D2C2, D8C3, and D10C5.	80
Figure 4.25: SEA of corrugated tubes.	81
Figure 4.26: Transition of peak force to the end of the f–d diagram by increasing the diameter of the grooves (structural softening).	82
Figure 4.27: EA of corrugated tubes.	82
Figure 4.28: SEA of corrugated tubes.	83
Figure 4.29: Optimum corrugated tube of D7C5 model; (a) f–d diagram; (b) deformation pattern.	84
Figure 4.30: EA of tubes with different number of grooves and groove sizes.	84
Figure 4.31: Effect of the location of grooves on the deformation of corrugated tubes.	85
Figure 4.32: Effect of the location of grooves on E1, E2, and E3.	86
Figure 4.33: EA of C5 models as a function of wall thickness and diameter of grooves.	87

Figure 5.1: Stress–strain curve of the base and cladding materials.	90
Figure 5.2: (a) Plastic strain localization in 6:3:2 ring with the base material; (b) cross-section of the ring with base material and x-shape section with ductile material.....	91
Figure 5.3: F–d diagram of ring with pure base material and mixed with clad material.	91
Figure 5.4: F–d diagram of rings without friction between the contact surfaces.....	92
Figure 5.5: Cross section of rings with 30% of clad material.	93
Figure 5.6: Effect of the location of clad material on f–d diagrams.	93
Figure 5.7: Cladding layer on the inner and outer surfaces.	94
Figure 5.8: (a) Radial stress distribution; (b) tangential stress distribution; compressive stress in dark grey and tensile stress in white.	94
Figure 5.9: Results of simulation of the model with pure base material.....	95
Figure 5.10: Sketch of the laminated composite system (top view).	96
Figure 5.11: Effect of cladding layer on the crashworthiness of the base model.....	97
Figure 5.12: Effect of cladding layer on the crashworthiness of the base model.....	98
Figure 5.13: Inner surface cladding versus outer surface cladding.....	98
Figure 5.14: (a) Circular tubes supported by spiral blades; (b) deformation pattern.	100
Figure 5.15: (a) Performance of supported tubes; (b) f–d curve and deformation of w15t4.	101
Figure 5.16: (a) F–d curve of the w15t4 model with different blade materials; (b)–(d) deformation at 65%, 88%, and 100% of displacement, respectively.	102
Figure 5.17: Circular tubes with 75% base material and 25% clad material along different directions.	103
Figure 5.18: Deformation of circular tubes with 25% clad material.....	103
Figure 5.19: F–d diagram of circular tubes with 25% clad material at different angles.	104

LIST OF TABLES

Table 3.1. Input parameters for the J–C plasticity model [Systèmes, 2012].....	45
Table 4.1. Comparison of simulations in ABAQUS.....	59
Table 4.2. Input parameters for the J–C plasticity model [Tarlochan et al., 2013; Systèmes, 2012].	60
Table 4.3. Comparison of EA capacity and CFE of circular tubes for the selection of a proper tube length.....	61
Table 4.4. Comparison of EA capacity and CFE of P400-L350 model with different friction coefficients.....	65
Table 4.5. Effects of initial velocity and mass of impact on the EA capacity and CFE of P400-L350 model.....	66
Table 4.6. Effect of temperature on EA and CFE.....	68
Table 4.7. Effect of strain rate sensitivity on EA and CFE.....	69
Table 5.1. Effect of cladding layer on EA and CFE.....	96
Table 5.2. Effect of 25% cladding with different orientation of layers on EA and CFE.....	104

Chapter 1 Introduction

1.1 Dynamic loading and impact test

1.1.1 Importance of energy absorbers in vehicles

The demand for advanced transportation systems has increased in today's modern society. At present, registered vehicles in Canada have reached approximately 35 million. This number rapidly increases every day, which consequently results in the increase in the number of accidents. Approximately 160,000 car accidents occur each year in Canada, of which approximately 3,000 have resulted in deaths [<https://www.thestar.com>]. Meanwhile, the number is higher in the United States where approximately 37,000 deaths occur due to road crashes each year [<https://www.iihs.org>]. These statistics on fatal or serious injuries in traffic collisions indicate the importance of designing safe motor vehicles.

Regarding safety, crashworthiness is a main factor in designing a vehicle. The kinetic energy of a moving vehicle should be absorbed and converted into inelastic (nonrecoverable) form of energy when an accident occurs. Crashworthiness is the degree to which a component or a vehicle absorbs the energy during impact to reduce the damage to the structure of interest, such as the occupant compartment in a passenger car. Thus, energy absorption (EA) systems with high crashworthiness capacity or efficiency have been the focus in the automotive industry [Mirzaei et al., 2012]. Figure 1.1 illustrates the schematic of energy absorbers and occupant compartment in a passenger car.

1.1.2 EA systems

Energy absorbers are used in the automotive industry and motor vehicles traveling on the road daily. These components have been widely used in trains, ships, and machineries where the mass or speed of a moving object is considerable. Any mechanism or system that dissipates kinetic energy during an impact or an accident can be considered an EA device or system. During a car crash, kinetic energy is converted into an inelastic or nonrecoverable form of energy, such as plastic deformation, viscous energy, and friction or fracture energy [Olabi et al., 2007].

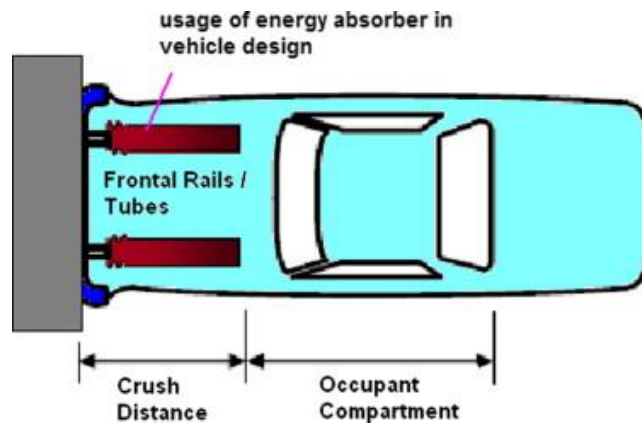


Figure 1.1: Energy absorbers and occupant compartment in a passenger car [Tarlochan et al., 2013].

1.1.3 Design parameters of energy absorbers

Researchers and design engineers should have an extensive knowledge of related topics, such as mechanics of materials, structural mechanics, impact dynamics, and plasticity theory, to develop and design efficient EA devices. An energy absorber is required to withstand dynamic loads upon impact and collapses with large plastic deformation [Olabi

et al., 2007]. Several principles should be considered in the design of energy absorber components. Some of the main factors are presented as follows.

1.1.3.1 Force–displacement (f–d) graphs

Plotting an f–d curve is the first step in investigating the behavior of an energy-absorbing component. The energy absorbed is the area under this curve. The reaction force and stroke (displacement) play important roles in the efficiency of devices. A typical f–d graph obtained from an impact test is shown in Figure 1.2. The maximum reaction force that usually occurs at the beginning of the strike should be held under a threshold. Increase in the amount of this force results in high deceleration, which is unfavorable and causes huge damage to the protected structure and the occupants. The reaction force should be kept relatively constant with minimal fluctuation during deformation [Morris et al., 2005]. The energy absorbed has a direct relation to the stroke length. A large amount of kinetic energy can be absorbed by increasing the stroke length or displacement during plastic deformation of the energy absorber when the reaction force is maintained to a constant value.

1.1.3.2 Production factors

Weight and cost of energy absorbers are important factors in design and manufacturing processes. The heavier the structure is, the more fuel consumption will be. Fuel consumption is a key factor in air pollution. Nearly 30% of Canada’s total emission is produced by transportation systems [<https://www.canada.ca>].

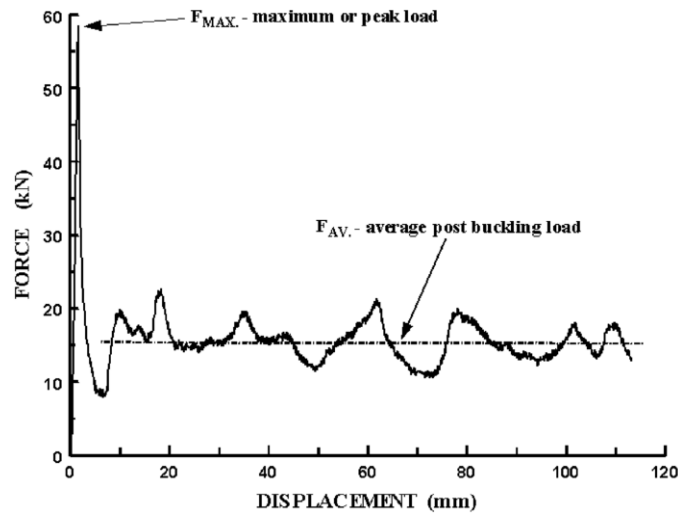


Figure 1.2: Typical f - d curve of an energy absorber [Guillow et al., 2001].

Energy absorbers are a one-time use device. The major purpose of such devices is to sustain the impact energy during large plastic (nonrecoverable) deformation. These devices are unusable when they are deformed. Therefore, efficient energy absorbers should be developed with minimal cost.

1.1.4 Thin-walled structures as energy absorbers

Thin-walled structures have been widely used in civil construction, pressure vessels, storage units, cranes, automobiles, ships, aircrafts, and trains. Such components are widely used in the automotive industry due to their lightweight, simple operation, and low cost. They are also extensively promoted as energy absorbers because of their favorable behavior and performance under various types of loadings. Figure 1.3 illustrates some of the main applications of thin-walled components, such as front rails, rockers, and pillars, in a typical unibody structure of a car. The crash box of an automobile is a good example of the usage of thin-walled tubes as energy absorbers because it dissipates kinetic energy into plastic

deformation during impact in an accident. This condition results in low repair costs in low-speed vehicle collisions and small damage to the passenger compartment and the occupants.

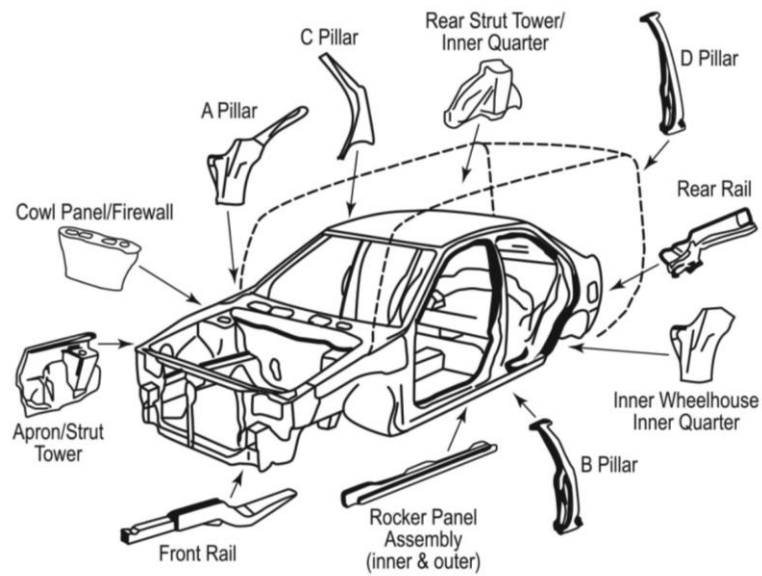


Figure 1.3: Thin-walled components in a typical unibody structure of a car [http://www.naaamap.com].

A crash management system is mounted behind the vehicle bumper. Circular, triangular, conical, square, or polygonal tubes made of aluminum alloys, steel alloys, or composite materials are some examples of thin-walled components utilized in a crash box [Mahbod et al., 2018].

1.1.5 Production of thin-walled tubes

Generally, two types of production methods, namely, welding and seamless processes, are used for the fabrication of thin-walled tubes or hollow structural sections (HSSs). The two processes can be combined in which one cross section can be transformed into another, such as circular into square or rectangular section. Welding involves a series of operations,

such as sheet metal forming and different types of welding and sizing. The welding method depends on the material characteristics and thickness of the sheet metal.

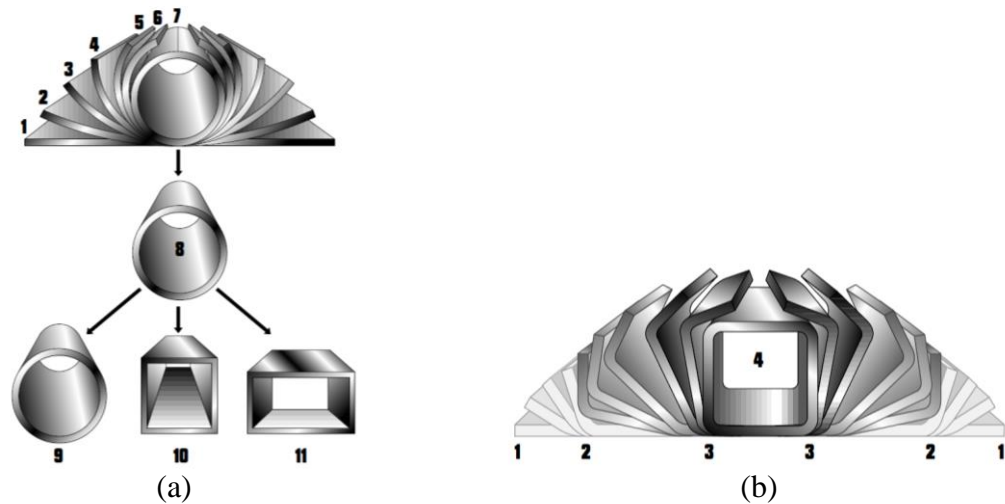


Figure 1.4: HSS welding manufacturing methods: (a) rolling and electric resistance welding; (b) form-square weld-square process [<http://www.cim.mcgill.ca>].

Extrusion and drawing are the main seamless processes in which a thin-walled structure is produced. During extrusion, hot or cold materials are pushed through dies that can have complex cross sections. This process can be performed on different materials, such as metals, polymers, ceramics, and concrete. During drawing, materials are pulled using a mandrel through a die. This process is also used for tube sizing. Most seamless circular tubes are fabricated by drawing.

The extensive temperature produced during welding can change the mechanical properties and microstructure of the base material in the heat-affected zone [Falkenreck et al., 2017]. Thus, seamless processes can be of more interest when determining the behavior of thin-walled tubes under dynamic loadings as energy absorbers. However, the effect of welding can be controlled and minimized via post weld heat treatment.

Another technique that is relatively new and can be considered a production method of energy-absorbing devices is 3D printing or additive manufacturing. By this method, many complex geometries and shapes can be produced and experimentally investigated through a computer aided design (CAD) file.

1.2 Static loading and ring compression test

Metal forming is a manufacturing process in which the material (workpiece) experiences large plastic deformations by taking the shape or geometry of the tool (die). The two main categories of metal forming are bulk and sheet metal forming, which can be performed under cold, warm, or hot conditions. A design engineer should have an extensive knowledge about the material of the workpiece and the interaction between the die and the workpiece to design an optimum tooling system and obtain an excellent product. This condition includes the plastic behavior of the workpiece under different velocities, temperatures, and frictional conditions occurring at the material–tool interface. In all metal forming processes, friction is an important factor in determining the life of the tool and quality of the final product. Major consequences of excessive friction in such processes are heat generation and wearing of the tool that can lead to its early failure. These conditions can increase the possibility of inhomogeneous deformation that results in unexpected manufacturing defects in the final product. The main strategy used to reduce the effect of friction is the usage of lubricants. However, the reduction of friction is not always a goal in such processes. Friction can be advantageous in controlling the material flow to attain the desired product with minimum effort. Rolling, extrusion, and forging are processes in which friction can be used to achieve the final product [Rao et al., 1993].

Ring compression test, originally introduced by Kunogi [1954], is widely used for the quantitative evaluation of friction. The main benefit of this technique is that it only requires dimensional measurements and does not involve the mechanical properties of the specimen or external forces. In this test, a relatively short thick-walled cylinder is axially compressed between two rigid platens. The standard geometry initially used for this purpose by Male and Cockcroft [1964] was 6:3:2 (outer diameter: inner diameter: height). The test is stopped with a percentage reduction in height, and the plastic deformation of the specimen is analyzed. Generally, the internal diameter increases when friction is negligible, and a high friction leads to an inward flow of the material and reduction in the internal diameter. High values of friction are associated with the so-called barreling effect in which the material begins to bulge from the side walls. Experimental calibration curves are obtained by measuring the dimensions of the rings before and after deformation. Here, reduction in height under different friction coefficients is plotted with the change in the internal diameter of the ring with a specific geometry and is considered a friction calibration curve. These curves are widely used by design engineers; however, they cannot be applied in different cases because they are unsuitable for all conditions [Sofuoglu et al., 1999]. The combination of tool–material with the same geometry plays an important role in the outcome of this test [Kim et al., 1990]. Temperature is another factor that should be considered in such tests.

1.3 Thesis outline

Several factors should be considered in investigating the behavior of a structure subjected to static/dynamic axial compression. In these cases, the specimens experience large plastic

deformations to either gain a desirable shape or absorb the impact energy during nonrecoverable deformation. Material properties, such as yield stress, strain rate sensitivity and strain hardening, shape and geometry of specimens, test temperature, friction coefficient at the interacting surfaces, and the speed of the tests, are some of the key points that can individually or by combination affect the outcome of a test. Numerical investigation of these parameters in quasi-static and dynamic axial loading conditions and analyzing the performance of thin-walled structures as energy absorbers are the primary objectives of this thesis.

This chapter introduces the static and dynamic compression tests and the objective of this thesis.

Chapter 2 presents a literature review of previous relevant studies. Topics related to thin-walled energy absorbers and crashworthiness of structures are discussed in the first part, and articles related to ring compression test are presented in the second part of this chapter.

Chapter 3 conducts numerical analysis and simulation of ring compression test. Different parameters, such as material properties, strain rate sensitivity, strain hardening, and geometry of the specimens that affect the results of ring compression test are discussed.

Chapter 4 investigates the energy-absorbing behavior of circular thin-walled tubes under dynamic loading conditions using finite element (FE) models. Numerical responses of corrugated tubes with different number of grooves and groove sizes are evaluated, and the optimum geometry is presented. The effects of the mechanical properties of material,

friction coefficient, test speed, and temperature on the crush behavior of thin-walled tubes are numerically assessed.

Chapter 5 evaluates the effect of clad and core material properties and volume fraction of cladding material on the crashworthiness of thin-walled tubes. The EA capacity of circular tubes supported by spiral blades made of different materials (clad/core material) is numerically investigated.

Lastly, Chapter 6 summarizes the conclusions of this thesis.

Chapter 2 Literature review

2.1. Dynamic loading and energy absorbers

Analysis of energy-absorbing devices has attracted the interest of many engineers and researchers since the second half of the 20th century. Many papers focusing on the EA of structures, especially thin-walled components, have been published. Some of the published papers are the International Symposium on Structural Crashworthiness (established in 1983), International Journal of Impact Engineering (founded in 1983), and books presenting papers, such as Structural Failure by Wierzbicki and Jones [Wierzbicki et al., 1989], Structural Crashworthiness and Failure by Jones and Wierzbicki [Jones et al., 1993], and Crashworthiness of Vehicles by Johnson and Mamalis [Johnson et al., 1978]. Extensive review papers on crashworthiness and impact behavior of energy absorbers, such as Alghamdi [Alghamdi, 2001], Olabi [Olabi et al., 2007], Yuen [Yuen et al., 2008], and Shinde [Shinde et al., 2018], have also been published.

Pugsley and Macaulay [Pugsley et al., 1960] and Alexander [Alexander, 1960] first investigated the behavior of thin-walled tubes under axial loading. They started with the analysis of the collapse of cylindrical tubes. Pugsley and Macaulay [Pugsley et al., 1960] evaluated the geometry of crushed samples during and after loading. They discussed the formation of diamond patterns around the tube and the change of the shape of these diamond patterns from square to rhomboid. They introduced an approximate theory to relate the axial load and the shape or mode of the deformations based on the yield stress, shear stress, and geometry of the samples. Alexander [Alexander, 1960] evaluated cylindrical shells as energy absorbers, derived an approximate theory with an empirical

relationship to predict the collapse load based on the geometry of the material, and compared it with the experimental results.

In 1978, Johnson and Mamalis [Johnson et al.,1978] gathered considerable valuable information regarding plastic deformation and mechanics of impact in cars, ships, aircrafts, motorcycles, trucks, locomotives, and elevators. They illustrated different types of damage to vehicle structures that may occur during a crash and discussed the reduction of catastrophic consequences of a collision using airbags and energy absorbers or improving the frame structures.

2.1.1 Circular thin-walled tubes as energy absorbers

Circular tubes are a common type of thin-walled structures investigated under axial loading and used in energy absorber systems [Sadeghi, 1984; Alghamdi, 2001]. Circular tubes are widely used because they provide a relatively constant operating load, which is a favorable characteristic of energy absorbers. In comparison with other geometric structures, circular tubes provide higher EA capacity and displacement per unit mass [Alghamdi, 2001].

2.1.2 Deformation modes in circular tubes

Andrews [Andrews et al., 1983] investigated the deformation modes of aluminum alloy cylindrical tubes under quasi-static axial loading. They crashed 189 tubes and then classified the modes of collapse in seven categories as follows: (a) concertina, in which the tube starts to fold with back-to-back axisymmetric ring-shaped plastic hinges perpendicular to the tube axis; (b) diamond, in which the tube folds with back-to-back nonaxisymmetric multicorner plastic hinges perpendicular to the tube axis; (c) Euler, in which the tube bends;

(d) mixed mode or concertina and diamond, in which the tube begins to fold in concertina mode and then changes to diamond configuration; (e) multi concertina, in which the tube begins to fold by more than one concertina pattern; (f) multi diamond, in which the tube begins to fold by more than one diamond pattern; and (g) tilting of tube axis, in which transverse displacement occurs at one end. The mixed mode relatively occurred in long tubes. In this case, the diamond pattern was initiated after several folds of concertina configuration. The authors provided some expressions for the calculation of energy per fold for concertina and diamond configurations in terms of net area of the tube and volume of folds. On the basis of the classification chart that the authors provided for the collapse of the 189 aluminum tubes, a tube with a diameter-to-thickness ratio of approximately 70 ($D/t \approx 70$) and length-to-diameter ratio of less than 3 ($L/D < 3$) is likely to collapse with a concertina deformation mode. A sample is highly probable to reach diamond, mixed, or Euler (bending) modes of deformation with the decrease of D/t ratio and increase of L/D ratio. Thornton [Thornton et al., 1977] showed that small thickness-to-diameter (t/D) ratios result in the formation of diamond patterns with many corners. They proposed an empirical relationship for the estimation of specific EA (SEA) in terms of t/D ratio and material constants. This equation was obtained by curve fitting based on the experimental results. Figure 2.1 illustrates the deformation modes of concertina and diamond.

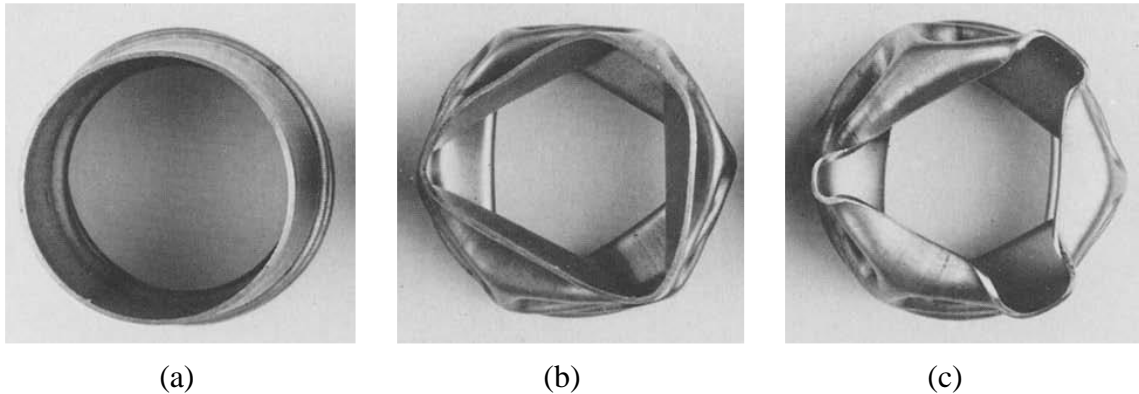


Figure 2.1: Common modes of deformation in circular tubes: (a) concertina mode (axisymmetric); (b) and (c) diamond mode (non-axisymmetric) [Abramowicz et al., 1984a].

Two typical modes of collapse, namely, progressive buckling, which is the desirable mode of collapse and can be controlled, and Euler bending, which is inefficient and can result in instant and large deformations with disastrous outcomes, can occur on a tube under axial loading [Hsu et al., 2004]. Abramowicz and Jones [Abramowicz et al., 1997] performed an experimental study on the response of circular tubes made of mild steel under static and dynamic loadings and analyzed their transition mode from global (Euler) bending to progressive buckling. They observed that even small L/D ratios can initiate plastic deformation through global plastic bending. They also found that the specimen can complete its collapse through global bending, although it developed progressive buckling in the beginning of collapse (for example at both ends). They concluded that the transition point depends on several factors, such as geometry of the tubes (L/D and D/t ratios), material properties, strain hardening effect, strain rate sensitivity, and type of the supports at both ends. The authors noted that inertia forces can be ignored during progressive buckling but should be considered when the tube is under global bending.

Karagiozova and Jones [Karagiozova et al., 2008] investigated the behavior of long circular tubes made of aluminum alloys under dynamic loading. They performed numerical simulations for various geometries with different D/t and L/D ratios and four different material properties. Their main objective was to determine the mechanisms of buckling transition, global bending, and progressive buckling in the tubes. They indicated that the velocity of impact tests plays an important role in the deformation model of the tubes. The dynamic transition mode from global bending to progressive buckling varied for different samples on the basis of the geometry of the samples, material properties, and impact velocity. Some of their results in which this conclusion is made are presented in Figure 2.2.

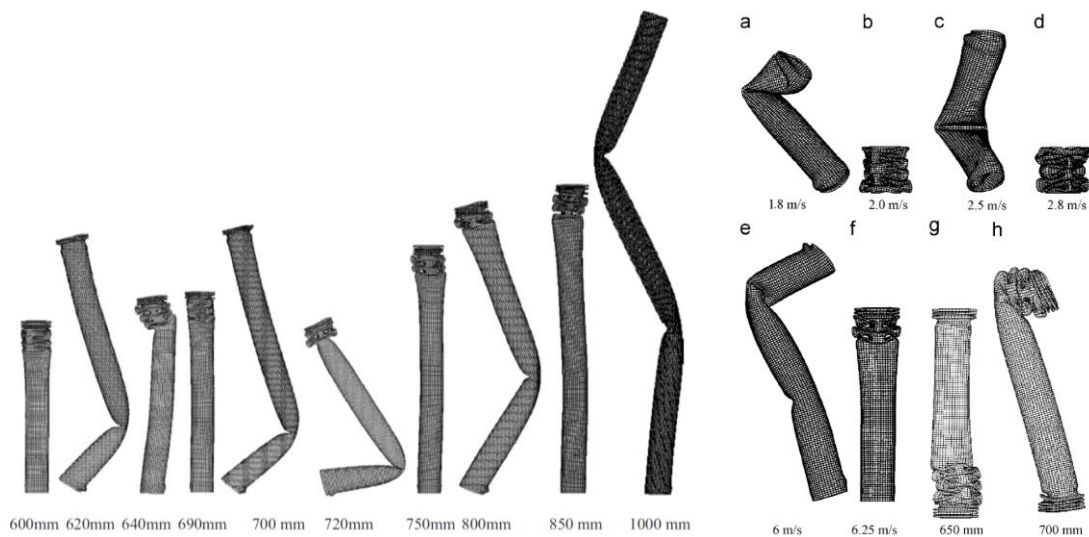


Figure 2.2: Simulations of circular tubes with different L/D ratios and impact velocities [Karagiozova et al., 2008].

The authors concluded that increasing the velocity of impact tests and/or increasing the tube lengths does not necessarily converge to a transition zone. The deformation of their numerical models agreed with the experimental results. However, they assumed frictionless contact between the surfaces of the tubes in their FE analysis (FEA).

2.1.3 Average force in static loading

2.1.3.1 Average force in concertina deformation mode

Alexander [Alexander, 1960] conducted experiments to determine the average crushing force of mild steel tubes under axial loading. He considered each fold as a wide beam with three joints deforming under plane strain conditions. He assumed that the material was rigid and perfectly plastic, used von Mises criteria, and proposed an expression for the average force, which is expressed as:

$$F_{avg} = K S_y t^{1.5} \sqrt{D} \quad (2.1.1)$$

where K is the material constant, S_y is the yield stress of the material, t is the wall thickness, and D is diameter of the tube. In the analysis, the author assumed a value of $K = 6.08$ for the mild steel material. He concluded that changing this value to 6.2 would lead to a more accurate result. On the basis of this work and Alexander's theoretical solution, Abramowicz and Jones [Abramowicz et al., 1984a] derived an equation for predicting the average crushing force under dynamic loading for axisymmetric deformation mode (concertina mode), which can be expressed as follows:

$$F_{avg} = S_y t (6\sqrt{Dt} + 3.44t) \quad (2.1.2)$$

Jones and Abramowicz [Jones et al., 1985] improved their previous prediction in the following form:

$$F_{avg} = S_y t (6\sqrt{Dt} + 3.44t) / (0.86 - 0.568\sqrt{t/D}) \quad (2.1.3)$$

Reid [Reid, 1993] reviewed the above studies by conducting experiments on seamless mild steel tubes. He expressed that the theory presented by Abramowicz [Abramowicz et al., 1984a] and Jones [Jones et al., 1985] provides a good estimation for concertina and diamond modes. However, he indicated that the effect of strain hardening should be considered in the theory.

2.1.3.2 Average force in diamond deformation mode

Pugsley and Macaulay [Pugsley et al., 1960] first investigated the behavior of circular tubes under axial loading. They conducted plastic hinge analysis and provided an equation for predicting the average crushing force, which can be expressed as follows:

$$F_{avg} = S_y t (10.05t + 0.38D) \quad (2.1.4)$$

In another work after approximately two decades, Pugsley [Pugsley, 1979] proposed a modified version of their prediction based on Alexander's theory, which is expressed as

$$F_{avg} = 2.286n^2 S_y t^2 \quad (2.1.5)$$

where n is the number of lobes or corners. He suggested that the above equation is a better approximation when $n = 4-6$. His work was conducted by crumpling tubes with D/t ratios of more than 100 ($D/t > 100$) under static compression loads. According to Jones [Jones et al., 1985], Wierzbicki proposed the following relation for the diamond pattern:

$$F_{avg} = 18.15 S_y t^2 (D/t)^{1/3} \quad (2.1.6)$$

The presented equations are in good agreement with the experimental results [Reid, 1993]. However, they do not predict the load versus displacement diagrams and peak load and does not include the effect of strain hardening.

2.1.4. Other tube shapes as energy absorbers

The crashworthiness of other shapes of thin-walled structures has been widely investigated. Postlethwaite and Mills [Postlethwaite et al., 1970] pioneered in investigating truncated circular cones (frusta) as energy absorbers. They predicted the average crushing load of cones with perfectly plastic rigid material, as shown as follows:

$$F_{avg} = 6S_y t^{1.5} \sqrt{d + 2x \sin \varphi} + 5.69S_y t^2 \tan \varphi \quad (2.1.7)$$

where d is the small diameter of the cone, t is the thickness of the cone, x is the displacement, and ϕ is the semi-apical angle of the cone. Mamalis [Mamalis et al., 1983] investigated the compression behavior of aluminum circular tubes and frusta with various thickness (with semi-apical angles of 5° – 20°) under axial static loading. Their main objective was to determine the different deformation modes of frusta. They concluded that the thin cone-shaped tubes deformed with diamond patterns, whereas the thick ones folded with axisymmetric rings. They also observed that the peak and mean post-buckling load parabolically increased with the increase of wall slenderness ratio or wall thickness. In another research, Mamalis [Mamalis et al., 1986] conducted an experiment on plastic in the hinges of deformed rings without the effect of the interaction between the surfaces and introduced a theoretical model for the estimation of mean crushing force, which can be expressed as:

$$F_{avg} = 6S_y t^{1.5} (\sqrt{d} + 0.95\sqrt{t} \tan \varphi) \quad (2.1.8)$$

Multicorner tubes have also been investigated by many researchers. Square tubes are the most investigated structures under this category. Wierzbicki and Abramowicz [Wierzbicki et al., 1983] evaluated square tubes as energy absorbers in 1983. They assumed a perfectly plastic rigid material in their theory and proposed an equation for the average crushing force, as shown as follows:

$$F_{avg} = 9.56S_y t^{5/3} D^{1/3} \quad (2.1.9)$$

where D is the length of each side of the square. This equation was designed for square tubes with symmetrical deformation mode. Subsequently, Abramowicz and Jones [Abramowicz et al., 1984b] presented an equation for the asymmetric behavior of square tubes in the form:

$$F_{avg} = S_y t (9.96D^{1/3} t^{2/3} + 0.84D^{2/3} t^{1/3} + 0.58t^2) \quad (2.1.10)$$

Abramowicz and Wierzbicki [Abramowicz et al., 1989] collaborated again in 1989 and proposed another equation for predicting the average force under symmetrical collapse deformation mode, which was in good agreement with the experimental results. The equation is shown as follows:

$$F_{avg} = 13.06S_y t^{5/3} D^{1/3} \quad (2.1.11)$$

2.1.5 Effects of strain-rate and strain hardening parameter

Postlethwaite and Mills [Postlethwaite et al., 1970] and Abramowicz and Jones [Abramowicz et al., 1997] investigated metal tubes subjected to axial dynamic loads and

observed the influence of strain rate sensitivity on the behavior of their specimens. Jones [Jones, 2012] expressed that the effect of material strain rate sensitivity plays an important role on how the structure responds to dynamic loading and should be considered for the strain rate sensitive materials. Cowper–Symonds uniaxial relation is a common empirical equation used to address the rate sensitivity in theoretical and numerical studies, which can be expressed as follows:

$$S_y^d = S_y \left[1 + \left(\frac{\dot{\epsilon}}{k} \right)^{\frac{1}{p}} \right] \quad (2.1.12)$$

where S_y^d is the yield stress at dynamic loads (dynamic yield stress), and p and k are material constants obtained experimentally. For mild steel, these values are determined from dynamic uniaxial tests as $k = 40.4 \text{ s}^{-1}$ and $p = 5$ [Jones et al., 1985]. However, the same authors obtained $k = 802 \text{ s}^{-1}$ and $p = 3.585$ for mild steel in another work [Abramowicz et al., 1986]. They expressed that this discrepancy could be caused by the different test equipment and conditions. Abramowicz and Jones [Abramowicz et al., 1984a] estimated the average strain rate for concertina and diamond deformations, as shown respectively as follows:

$$\dot{\epsilon} = v / [2D(0.86 - 0.57\sqrt{t/D})] \quad (2.1.13)$$

$$\dot{\epsilon} = 0.74v/D \quad (2.1.14)$$

where v is the impact velocity.

Jones [Jones, 2012] indicated that the effect of strain hardening is small and should only be considered when the material has strong hardening properties. He conducted some

experiments on mild steel samples and expressed that any error in the calculations was less than 10% because the flow stress was approximately 10% larger than the yield stress. His main conclusion was based on the fact that the maximum stress would be reached only in some parts of the samples. Hsu and Jones [Hsu et al., 2004] investigated the behavior of stainless steel, mild steel, and aluminum alloy circular tubes under quasi-static and dynamic loadings. The three materials were selected because of their individual features to determine the effects of strain rate sensitivity, strain hardening, and inertia. The authors selected SS304 to analyze the effects of strain hardening and strain rate sensitivity of the material, AA6061 to assess the inertia effects (with negligible strain hardening and strain rate sensitivity), and mild steel to determine the influence of strain rate (when strain hardening of the material is negligible). The dimensions of the tube (L/D and t/D ratios) were used to cover progressive buckling and global bending. The authors doubled the mass in the input energy and observed that the EA rate of stainless steel tubes is strongly dependent on the initial impact velocity. They showed that stainless steel was the most efficient whereas aluminum was the least efficient material in the quasi-static tests by calculating the structural efficiency factor, $h = F_{avg}/(A_s y)$. The authors also determined a transition region between progressive buckling and global bending for mild steel based on a range of L/D ratios. However, this transition zone depended on the initial impact velocity. The authors concluded that stainless steel was the most efficient material in terms of energy absorbed per unit volume; meanwhile, aluminum was the most efficient material in terms of energy absorbed per unit mass, although it had the least energy absorbed per unit volume.

2.1.6 Miscellaneous topics

Guillow and his colleagues [Guillow et al., 2001] conducted a total of 70 quasi-static experiments on AA6061 circular tubes with various D/t ratios ($D/t = 10\text{--}450$). They normalized average forces (F_{avg}) with plastic moment (M_p) and logarithmically plotted them with D/t ratios. The plastic moment is defined as:

$$M_p = \sigma_0 (t^2/4) \quad (2.1.15)$$

where σ_0 is the flow stress, which is set to 0.2% proof stress. The authors proposed an empirical relation on the basis of their plot that formed a straight line for all modes of collapse (axisymmetric, nonsymmetric, and mixed modes), which is expressed as follows:

$$\frac{F_{avg}}{M_p} = 72.3 \left(\frac{D}{t}\right)^{0.32} \quad (2.1.16)$$

Substituting Equation (15) in (16) yields the following relation, which is similar to Equation (6) proposed by Wierzbicki for diamond (nonsymmetric) mode of deformation as follows:

$$F_{avg} = 18.08 \left(\frac{D}{t}\right)^{0.32} \quad (2.1.17)$$

Shi and his colleagues [Shi et al., 2014] performed a numerical analysis to determine the effect of rate sensitivity on the necking behavior of a laminated tube under rapid dynamic loading. They used an elastic–viscoplastic constitutive model presented by Weber and Anand [Weber et al., 1990] and assumed that the tube deformed in a plane strain condition. They used AA6111 as the base material with parameters representing a rate-independent material at the center, which was clad with a ductile rate-sensitive material on both sides. They observed that the contribution of the ductile material was significant and

delayed the necking initiation with the increase in the volume fraction of the cladding material, high loading speed, and increase of flow stress. Hu et al. [Hu et al., 2014] numerically investigated the necking behavior of a clad sheet having a rate-sensitive ductile cladding material on a rate-insensitive base material by considering a power law constitutive model for both materials. They found that a constant volume fraction of cladding layer and increasing the strain rate sensitivity of the clad material delayed the necking initiation. Moreover, the necking strain increased with the volume fraction of the clad material under a constant strain rate sensitivity.

Kohar et al. [Kohar et al., 2016] simulated the axial crushing behavior of extruded aluminum tubes using FE models. They selected SEA criterion as the optimization objective function and optimized the cross section of the extruded profiles. They concluded that the EA of an extruded profile made of AA6063-T6 could compete with those made of 7000-series aluminum alloys when an optimum wall thickness was selected for the profile.

2.2. Ring compression test

Kunogi [Kunogi, 1954] originated the ring compression test for determining friction. Male and Cockcroft [Male et al., 1964] modified this technique by introducing calibration curves on the basis of the deformation of the compressed ring. They used a ring geometric ratio of 6:3:2 (outer diameter: inner diameter: height, OD:ID:H), which was subsequently used as the standard geometry for ring compression test. Avitzur [Avitzur, 1964] presented a mathematical analysis of ring compression test. He ignored the effect of barreling; assumed

that the ring had a perfectly plastic rigid material; and proposed a relation for the friction factor based on the geometry of the ring, which is expressed as:

$$m = \frac{-1}{2\frac{R_o}{T}\left(1+\frac{R_i}{R_o}-2\frac{R_n}{R_o}\right)} \ln \left[\left(\frac{R_i}{R_o}\right)^2 \cdot \frac{\left(\frac{R_n}{R_o}\right)^2 + \sqrt{3+\left(\frac{R_n}{R_o}\right)^4}}{\left(\frac{R_n}{R_o}\right)^2 + \sqrt{3\left(\frac{R_i}{R_o}\right)^4 + \left(\frac{R_n}{R_o}\right)^4}} \right] \quad (2.2.1)$$

where R_i , R_o , and R_n are the inner, outer, and neutral radii, respectively; and T is the thickness of the ring. This equation is suitable for materials that flow inward and outward under high interfacial friction conditions. Hawkyard and Johnson [Hawkyard et al., 1967] verified this analysis.

Ring compression tests for various geometries and materials have been performed by many researchers in the last three decades. Janardhana and Biswas [Janardhana et al., 1979] investigated aluminum rings with varying ratios subjected to static axial compression under different frictional conditions. They found that the configuration of shear bands changed with the initial geometry of the specimens and plastic deformation. Plastic deformation was concentrated in the shear bands, and the width of shear bands increased with deformation. The authors noted that the band angle was more sensitive to the initial height under high friction conditions whereas less sensitive to the initial height under low friction conditions. Hartley et al. [Hartley et al., 1981] investigated the plastic deformation of tall hollow cylinders ($L/D = 1$ and 2) axially compressed under dry conditions with high interfacial friction. They observed three types of deformation during the initial stage of compression, namely, single-, double-, and triple-barreled free surfaces. They concluded that the

specimens with the initial flow mode of single barreling continued deformation in the same phase, whereas those samples with the initial phase of double barreling may change their stage to single barreling or may keep folding in the same double barreling phase. Carter and Lee [Carter et al., 1985] performed FEA of cylinder and ring compression with Coulomb friction. According to Coulomb's law,

$$\tau = \mu \cdot N \quad (2.2.2)$$

where τ is the frictional (shear) stress, μ is the friction coefficient, and N is the normal stress. The authors verified their numerical results with experiments. They noted that the calibration curves that Male and Cockcroft provided slightly changed when the effect of barreling was considered in the analysis. They plotted the load versus reduction in height graphs for two friction coefficients of $\mu = 0.17$ and 0.22 and showed that the rate in which the force was increasing was higher for specimens with larger D/L ratios (e.g., $D/L = 3$) than for those with smaller D/L ratios (e.g., $D/L = 1$).

Bhattacharyya et al. [Bhattacharyya et al., 1986] performed ring compression test to determine material anisotropy. They used Hill's yield criterion and Levy–Mises equations to show that a ring axial compression test could provide one of the three dimensionless terms for the uniaxial state of stress and has the potential to be a tool for investigating anisotropy under frictionless contact between the platens and the specimen. The authors expressed that the limitations of tensile stress, such as the range of plastic strain before necking and size of the tensile specimens, could be controlled by ring compression test. However, the friction at the interfaces of platens and ring should be kept low, in which the

neutral radius was constantly smaller than the inner radius and the material only flowed outward.

Beatty [Beatty, 1987] discussed several topics in elasticity, including Willis instability phenomenon. Experiments by Willis [1948] showed that the inner and outer surfaces began to bulge at the initial stage of deformation in hollow rubber cylinders subjected to axial loads. As the compression increased, the inner surface changed its deformation mode and formed a concave surface.

Singh et al. [Singh et al., 1991] performed ring compression tests on different materials at room and elevated temperatures. They used aluminum and steel for room temperature and lead and tin–lead alloy at elevated temperatures. Compressive yield stress was determined by plotting observed stress (σ_{obs}) against the initial diameter–height ratio (D_0/H_0) and extrapolating the values of stress to $D_0/H_0 = 0$ where the samples were compressed by a fixed amount. Two relations were used as follows:

$$\sigma_{obs} = \sigma_0 [1 + (\mu/3)(D/H)] \quad (2.2.3)$$

under the conditions of Coulomb friction for cold working, and

$$\sigma_{obs} = \sigma_0 [1 + (m^*/3 \times 3^{1/2})(D/H)] \quad (2.2.4)$$

for hot working, where σ_0 is the compressive yield stress, μ is the friction coefficient, and m^* is the interfacial shear stress (that can vary from zero to one for frictionless to sticky cases, respectively). The authors concluded that ring compression test could be used to determine the compressive yield stress in cold working. However, other methods could be more reliable in hot working conditions because ring compression test ignores the effect of

strain rate sensitivity. Singh et al. also indicated that the value of friction coefficient was constant at all strains for aluminum and steel and was independent of strain rate and grain size for aluminum.

Bontcheva et al. [Bontcheva et al., 1992] performed a numerical investigation of plastic localization bands in aluminum rings under static axial compression. They used four-node rectangular elements and verified their simulations with the experimental results of Janardhana and Biswas [Janardhana et al., 1979]. The authors concluded that the formation of plastic localization bands depended on the initial geometry of the specimens. Sahi et al. [Sahi et al., 1996] investigated the influence of strain rate sensitivity parameter (m) on friction factor through analytical analysis and plotting reduction in inner diameter (ID) (R_i^*) against reduction in height (h^*) curves. They showed that their results for perfectly plastic materials ($m = 0$) were consistent with Avitzur's [Avitzur, 1964] work. They indicated that as m increased, the R_i^*/h^* ratio decreased for each given value of friction factor.

Sofuoglu et al. [Sofuoglu et al., 1999] used power law constitutive equations in modeling and simulating the behavior of two soft materials in ABAQUS to investigate the ring compression test. They concluded that although the test is a reliable method for determining the friction coefficient, using available generalized friction calibration curves should be avoided. They expressed that these curves must be provided for the material of interest, and the type of material, rate of deformation, and the effect of barreling must be considered under the specific condition of the experiment. Robinson et al. [Robinson et al., 2004] performed similar FE simulations using power law models in ABAQUS to compare the

efficiency of three lubricants and their combinations. Ring compression test has been widely used for evaluating the friction factor in different alloys, such as Al–4%Cu [Desalegn et al., 2014], Ti–6Al–4V [Zu et al., 2011; Mirahmadi et al., 2015], and TA15 titanium alloy [Zhang et al., 2012].

Liu et al. [Liu et al., 2006] investigated the influence of hydrostatic pressure on the compression limit of AA7075 rings. They performed their experiments in a chamber and controlled the hydrostatic pressure on the inner and outer surfaces of the rings. They showed that the cracks began to initiate from the outer-top corner of the wall and grew to the middle of the inner wall. The tensile stress in the outer wall changed to compressive stress by introducing hydrostatic pressure. The authors concluded that a hydrostatic pressure of 100 MPa considerably affected the material flow and deformed contours and could increase the maximum compressive strain by approximately 30% for the specimens used.

To 2011, researchers had mostly used the standard geometries of rings (6:3:2) or macro size specimens, in which the dimensions depended on the range of centimeters. Chan et al. [Chan et al., 2011] investigated the effect of sample size on the deformation behavior of micro size rings. They performed compression test on AA6061 rings with IDs of 0.75–2 mm. They observed that the flow stress decreased for small specimens and that the shape of samples changed from circular (samples with ID of 2 mm) to irregular (samples with ID of 0.75 mm). The amount of friction coefficient and springback considerably increased with the decrease in specimen size. Fann et al. [Fann et al., 2017] experimentally evaluated the effect of grain size on ring compression test at elevated temperatures. They used AA6061

rings with a standard geometry of 6:3:2 at temperatures from 400 °C to 500 °C and concluded that the effect of lubricants on the friction coefficient was considerably greater than the effect of working temperature.

Cristino et al. [Cristino et al., 2015] focused on the effects of oxide films and surface roughness on friction evaluation. They isolated ring compression tests using argon and oxygen shields in a gas chamber and compared their results with those unprotected ring compression tests. They concluded that surface roughness had a great influence on friction coefficient and that the effect of gas shields was impractical for surfaces with $Ra \geq 0.4$. However, for smooth surfaces and under dry conditions, an oxygen-rich environment (test with oxygen shield) could increase the friction coefficient by 30% compared with those protected by argon shield. Veganzones et al. [Veganzones et al., 2014] used FE models and investigated the effect of shape factor (height-to-diameter ratio) on contact pressure profiles to determine the area of highest wear in short cylinders subjected to axial compression. They showed that the locations of maximum and minimum contact pressures entirely depended on the geometry of the specimens. For small shape factors, the maximum pressure occurred in the middle of the die, whereas for large shape factors, the minimum pressure occurred at this location and the area of maximum wear changed its place at the end of the contact edge.

2.3. Conclusion

Axial compression tests have been widely used in the past few decades in analyzing structural behavior under static and dynamic loadings. In such cases, the material

(workpiece) experiences large plastic deformations to obtain a desirable shape (in metal forming and static loading case) or to absorb the kinetic energy of the impact during nonrecoverable deformation (in dynamic loading case). The energy-absorbing characteristics of thin-walled structures were first investigated in 1960s. Subsequently, different parameters, such as the mechanical properties of the material and geometry of the specimens, have been evaluated in many numerical and experimental investigations.

Yield stress, strain rate sensitivity and strain hardening of the material, shape and geometry of specimens, test speed and temperature, and friction coefficient at the interacting surfaces play important roles in the outcome of the tests. These factors can individually or by combination affect the test results and should be considered when investigating structural behavior under static/dynamic axial compression.

Chapter 3 Static axial compression of rings

3.1 Introduction

Ring compression test was originally introduced by Kunogi [Kunogi, 1954] for determining friction. One decade later, Male and Cockcroft [Male et al., 1964] modified the test by producing calibration curves based on the deformation of the compressed ring. They used a ring geometric ratio of 6:3:2 (OD:ID:H), which was subsequently used as the standard geometry for ring compression test. This technique has been widely used by many researches.

In this thesis, ABAQUS software was used to numerically investigate the effect of different parameters, such as friction coefficient, strain rate sensitivity, strain hardening, test speed, and temperature, on the outcome of ring compression test. In the last section of this chapter, the deformation mechanism of rings subjected to hydrostatic pressure will be investigated.

3.2 FE configuration of ring compression test

Figure 3.1 shows a typical ring compression system in ABAQUS. The top and bottom platens were considered rigid bodies with reference points to extract the values of force and displacement. A ring with dimensions of 20:8:20 mm (OD:ID:H) was used to prepare a base model for the numerical studies. The model for these initial studies had an elastic–linear plastic material model with a yield stress of 390 MPa, Young’s modulus of 70 GPa, and Poisson’s ratio of 0.33. Several factors, such as element type, mesh size, mesh or element aspect ratio, and time incrementation, were evaluated in ABAQUS/Standard.

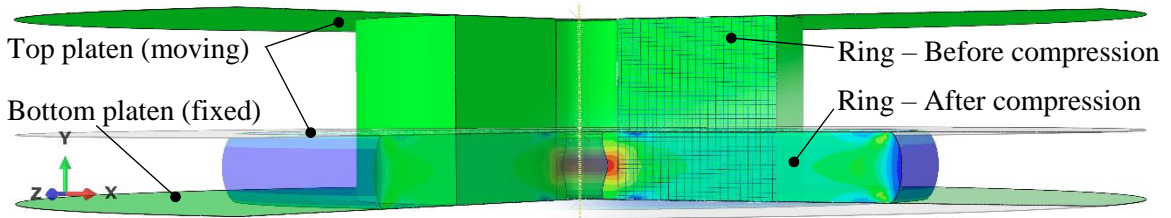


Figure 3.1: Typical ring compression system in ABAQUS.

The model was simulated with CAX3, CAX6, CAX4, and CAX8 elements. For the triangular elements (CAX and CAX6), diagonals of the top-half elements were swapped to achieve symmetry in the deformed model, as shown in Figure 3.2.a. The results were nearly the same (with approximately 2% difference), although an eight-node biquadratic axisymmetric quadrilateral (CAX8) element produced a slightly smooth f–d curve. Figure 3.2.b illustrates the comparison of CAX8R and CAX8 elements.

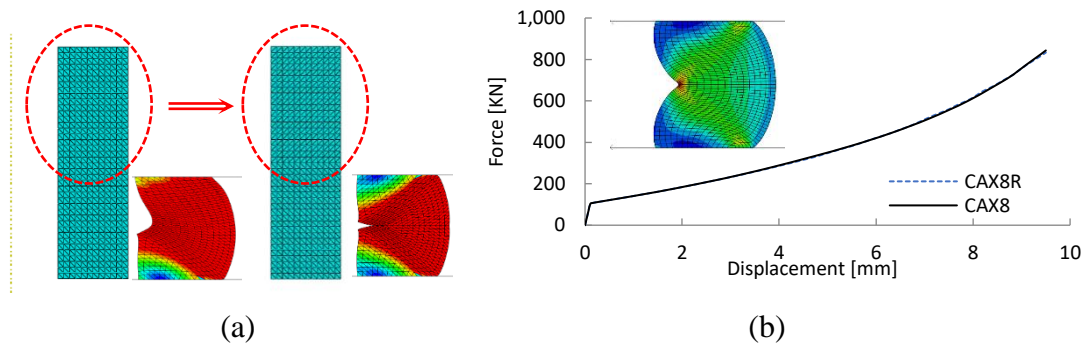


Figure 3.2: (a) Swapping diagonals of the upper half of CAX3 elements to obtain symmetry; (b) comparison of CAX8R and CAX8 elements with approximately 1% difference.

Elements with four aspect ratios of $\beta = h/r = 1, 1.5, 2,$ and 3 (where h and r denote the height and width of the element, respectively) were used in ABAQUS. Although a reasonable mesh pattern regarding the original geometry of the ring was produced when β

= 3, it did not result in an acceptable deformation, as shown in Figure 3.3. The aspect ratio of $\beta = 1$ provided a smooth shape regardless of the ring dimensions.

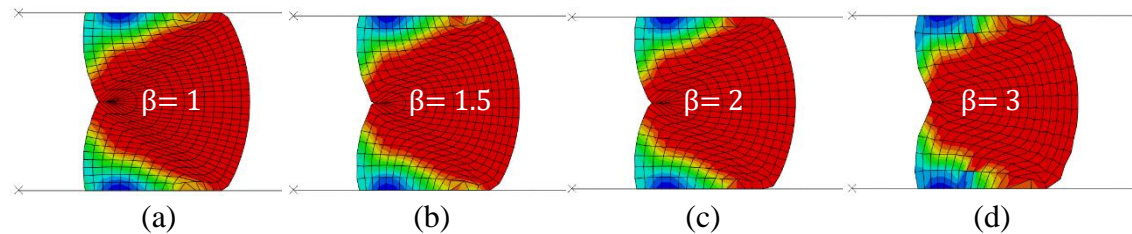


Figure 3.3: Effect of element aspect ratio on deformation: aspect ratio (β) (a) = 1; (b) = 1.5; (c) = 2; (d) = 3.

A mesh convergence study was conducted to select a suitable mesh size for the base axisymmetric model, as shown in Figure 3.4. A mesh size of 0.3 mm did not affect the results and considerably reduced the computation time compared with a mesh size of 0.1 mm.

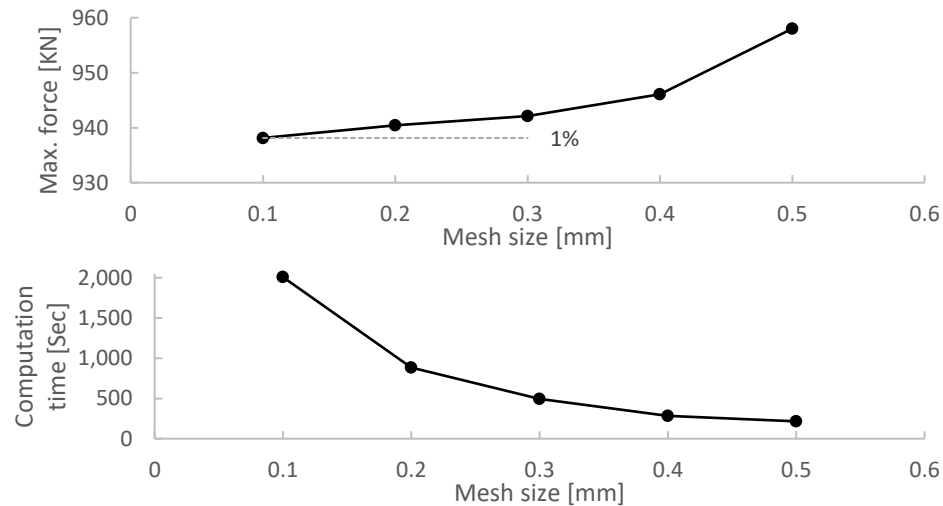


Figure 3.4: Mesh convergence study.

Several simulations were conducted with different time increments during compression. The size of the initial increment was given to the software, and ABAQUS automatically

selected the subsequent increment for the calculations. The size of the maximum increment immensely affected the computation time, although it did not lead to a different result. For compression, initial increment size of $1e-7$, minimum of $1e-10$, and maximum of 0.1 were selected, with a total of 10,000 increments.

Simulations of 3D models were compared with the axisymmetric models. The numerical results were the same, although the computation time increased dramatically for the 3D models. The symmetry in the axisymmetric models could not be used to simplify the analysis because of the existence of self-contact in the middle of the inner surface of the rings. Therefore, the full axisymmetric model should be used.

3.3 Effect of shape factor on ring compression test

Shape factor (λ) is defined as the ratio of height to wall thickness of the ring, as shown in Figure 3.5.

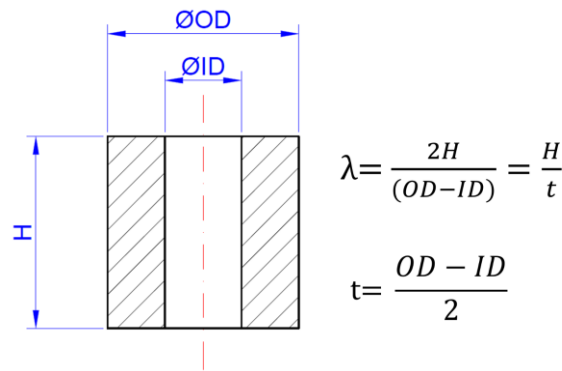


Figure 3.5: Definition of shape factor.

Five rings with initial height and outer diameter of 20 mm and IDs of 2, 4, 8, 12, and 16 mm were modeled and subjected to a quasi-static load. The shape factors for these rings

were 2.2, 2.5, 3.3, 5, and 10. The f–d diagrams of these simulations are presented in Figure 3.6.

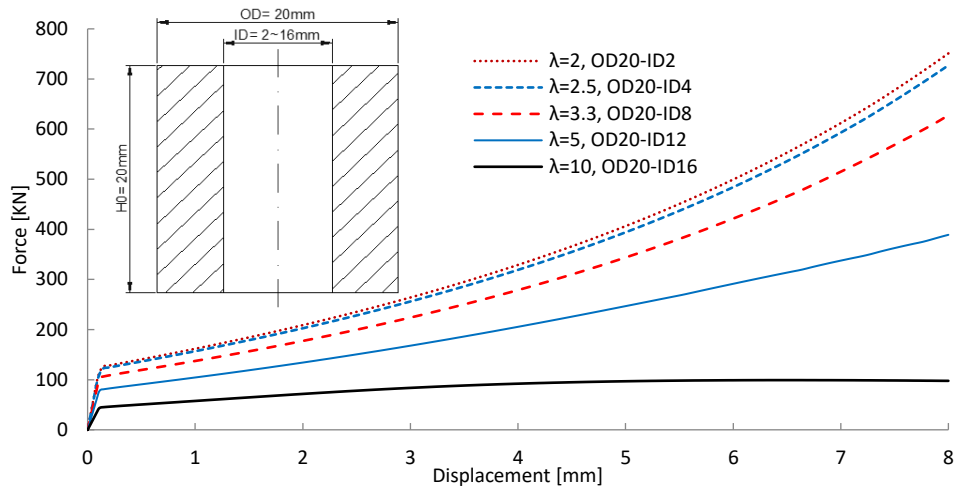


Figure 3.6: F–d curves for different shape factors.

Given that the values of height and outer diameter are fixed, small shape factor indicates a thick wall, whereas a large shape factor indicates a thin one. On this basis, considerable loads should be applied to compress many materials. As shown in Figure 3.6, the value of force is high for small shape factors at every stage of displacement or compression. The nodal values of force can be divided by contact area or volume (or mass) for comparison. The results are shown in Figure 3.7. From the figure, the order of curves in the graph is swapped. This condition indicates that considerable force per unit volume (or mass) is required to compress a cylinder with a large shape factor. The different trends in the shape of the black curve in this figure are due to different deformation modes (for the model with OD:ID:H ratio of 20:16:20 mm). Buckling occurred in this model with $\lambda = 10$, which resulted in less stiffening (or considerable softening) in the structure of the thick-walled cylinder, as shown in Figure 3.7.

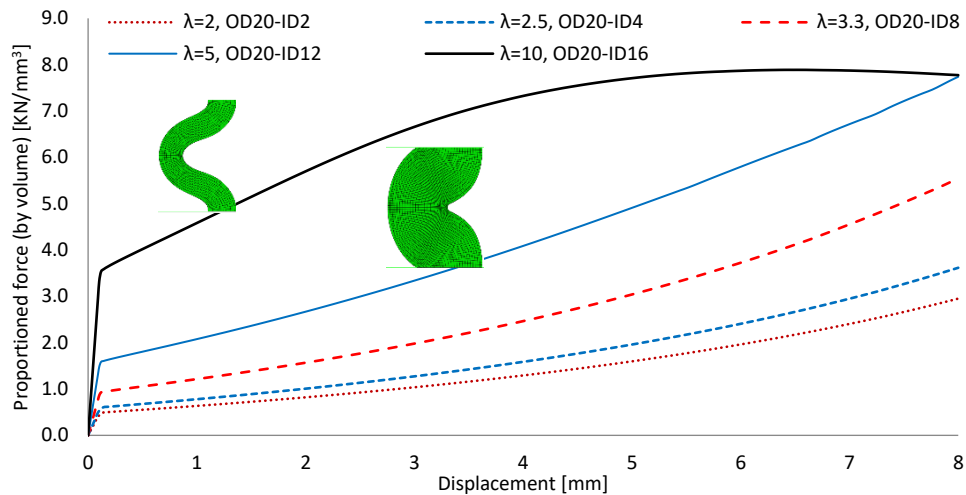


Figure 3.7: Proportioned f - d curves for different shape factors.

In another set of simulations, three rings with different dimensions but the same shape factor were subjected to axial loading. The outer diameter was 20 mm, which was constant for the three models. Case I had a height (H) of 16 mm and ID of 4 mm. Cases II and III had heights of 12 mm and 8 mm and IDs of 8 mm and 12 mm, respectively; the shape factor was $\lambda = 2$. Figure 3.8 shows the f - d diagrams of the three cases. From the figure, the value of force for the three cases was equal (approximately 180 kN) at the stroke of approximately 1.2 mm. This condition indicated that a point may exist in which the amount of work done for compression of these cylinders was equal. By numerical integration of the three curves, it was found that the same amount of energy (approximately 350 kJ) was consumed to compress the three geometries at the displacement of 2 mm (for the same amount of displacement). The two transition points are specified in Figure 3.8.

Given that the heights of these models were different, plotting the force against the percentage of reduction in height could be another means of comparison. The force could

also be proportioned by volume for comparison when the displacement is maintained at the horizontal axis. These processes are shown in Figures 3.9.a and 3.9.b.

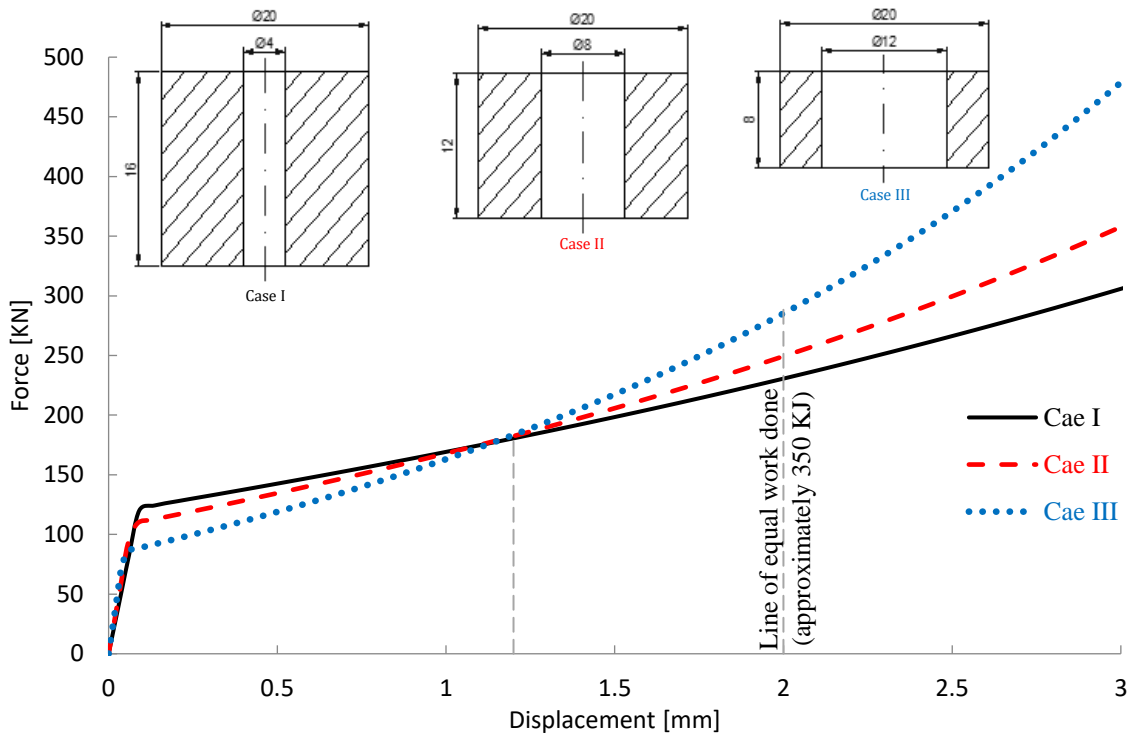


Figure 3.8: F–d curves for different geometries with the same shape factor.

The 2 mm displacement lines are shown in Figure 3.9.a. The 2 mm compression had 12.5%, 16.7%, and 25% reduction in height for Cases I–III, respectively. High values of force were obtained with the same amount of reduction in height in Case I, and high values of force per unit volume were obtained at the same displacement in Case III. In these simulations, the friction coefficient was 0.1. Different patterns could be obtained for other values of friction coefficient because friction plays an important role in the deformation of compressed rings. Figure 3.10 shows the three cases compressed at 50%. Barreling is more visible in the deformation of Case III compared with the other two cases.

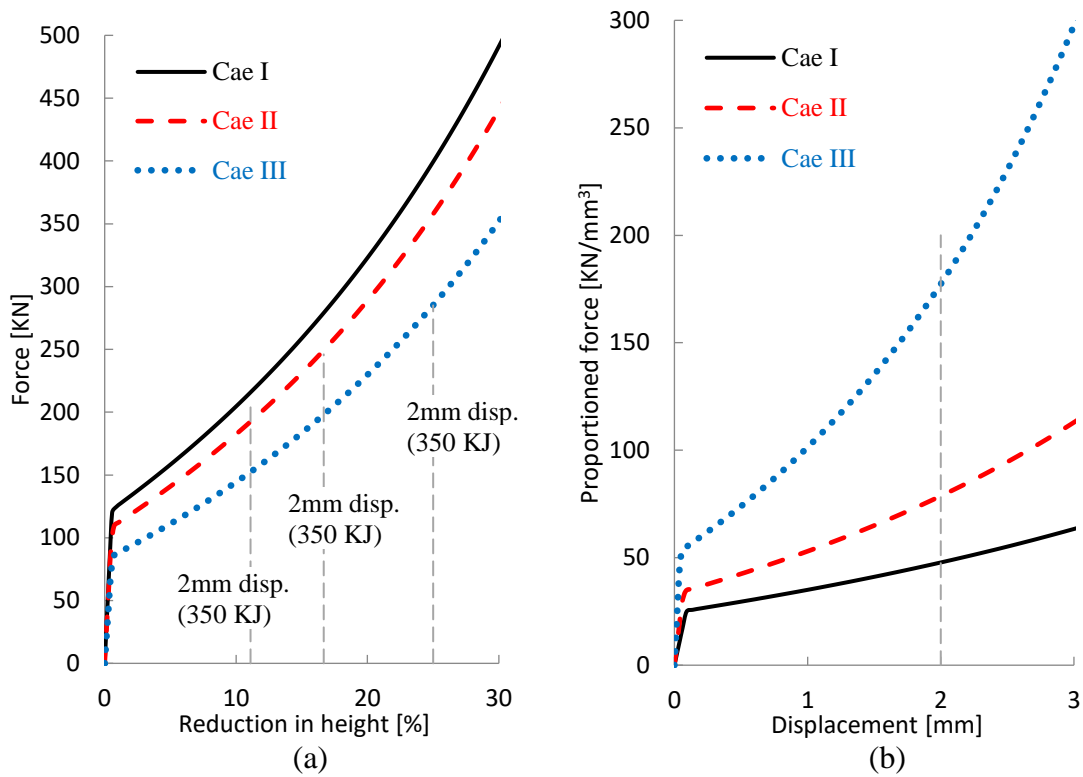


Figure 3.9: (a) Force versus reduction in height, and (b) proportioned force with volume versus displacement for the three cases.

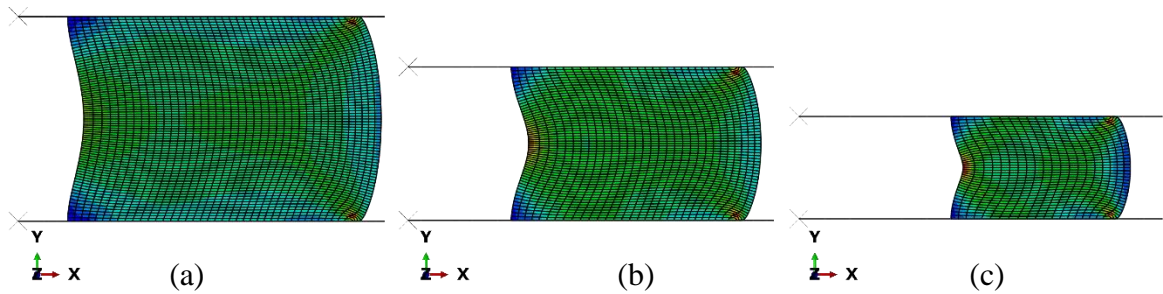


Figure 3.10: Deformation modes of (a) Case I (OD:ID:H ratio of 20:4:16 mm), (b) Case II (OD:ID:H ratio of 20:8:12 mm), and (c) Case III (OD:ID:H ratio of 20:12:8 mm).

3.4 Calibration curves for determining the friction coefficient

One of the main objectives of ring compression test is to produce calibration curves for determining the friction coefficient. To this end, the reduction in the ID is plotted against the reduction in height. The so-called standard geometry for this test has a ratio of 6:3:2 (OD:ID:H). This ratio is widely used by researchers and engineers.

A ring with dimensions of 18:9:6 mm (OD:ID:H) was modeled in ABAQUS. The dimensions were consistent with the standard geometry. The same elastic–linear plastic material used in the previous section was assigned to the model. Half of the axisymmetric model was used in ABAQUS because these simulations aimed to plot the calibration curves for up to 50% of compression (reduction in height). With this geometric ratio and material model, self-contact was not observed at the inner surface for up to 60%–70% of compression. Friction coefficients of 0 to 0.5 were assigned to the interaction properties of contact areas. Figure 3.11 shows the results.

The results of compression test were similar to that of uniaxial tensile test when friction did not exist between the ring and the platens. In this case, the only nonzero stress component was axial stress ($\sigma_y \neq 0$, $\sigma_x = \sigma_z = 0$), as illustrated in Figure 3.12. Figure 3.12.a shows a ring before and after compression. The material used in this simulation is shown in Figure 3.12.b. As expected, the equivalent stress was equal to the axial component of stress (in this case, σ_{22}) at the plastic strain of 49%.

As shown in Figure 3.11, the material only flowed outward with friction coefficients of 0 and 0.05. The material only flowed outward when the friction coefficient was 0.1 and the

compression was approximately 40%. Then, from 40% to the end of the compression, some materials moved inward, which decreased the ID at this compression rate. For $m \geq 0.2$, the inner surface went inward from the beginning of compression. For high values of friction coefficient, reduction in ID was increased with low rates. Figure 3.11 shows the deformation patterns in the upper half of the rings.

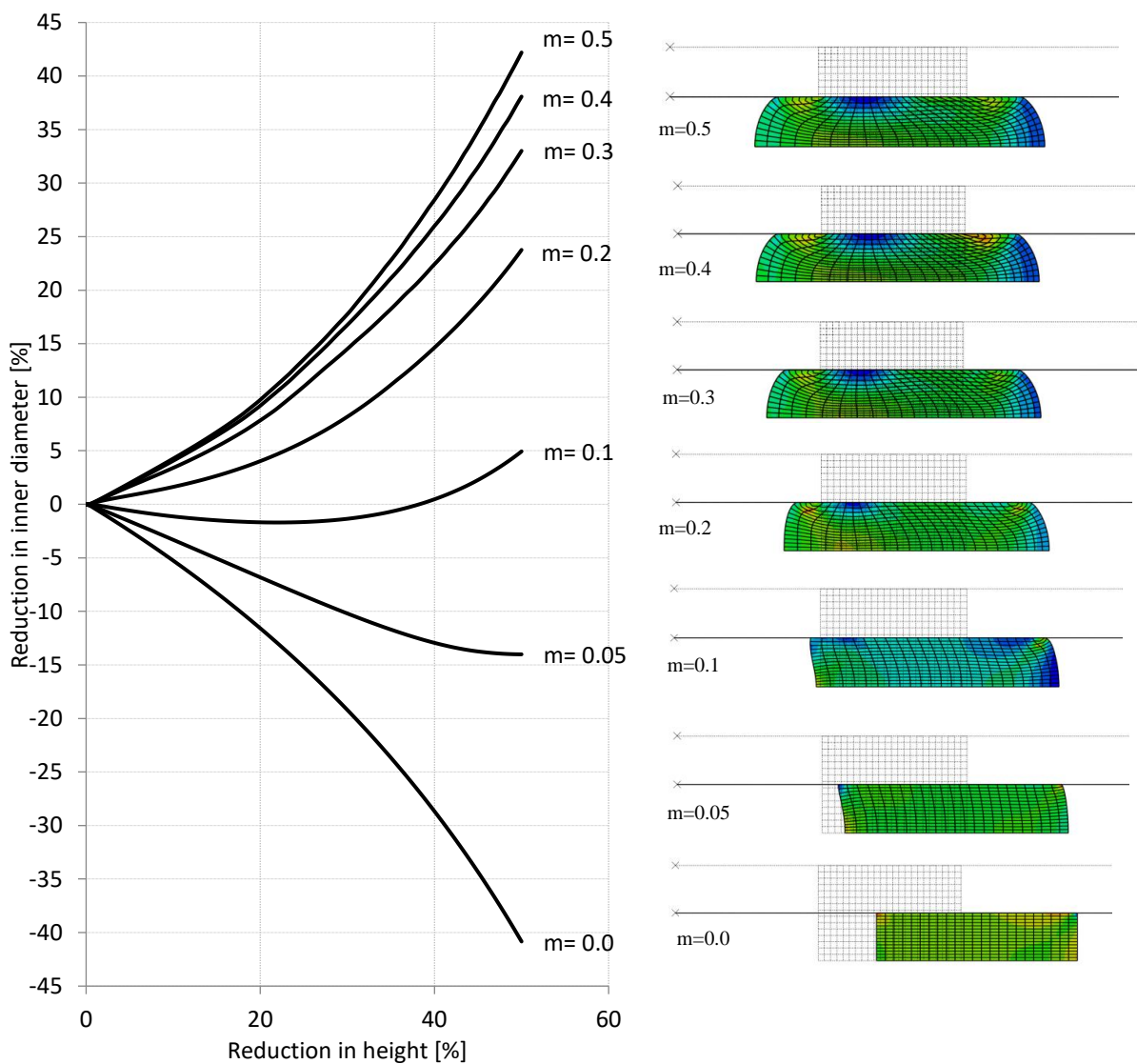


Figure 3.11: Calibration curves for determining the friction coefficient.

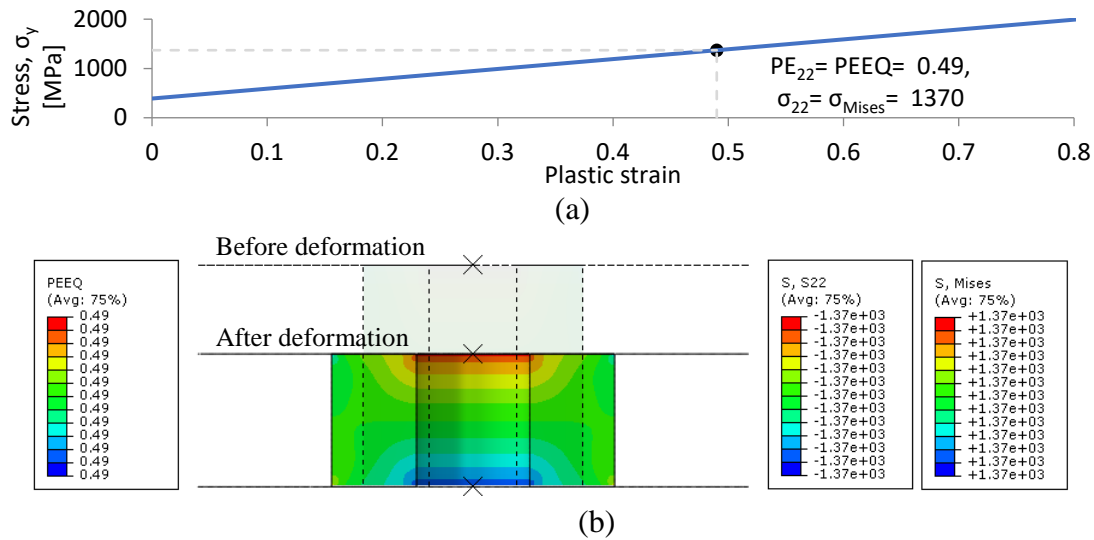


Figure 3.12: Similarity of ring compression and uniaxial tensile tests with friction coefficient of zero.

3.5 Effect of geometry on calibration curves

Here, the three cases in Section 3.2 were used to investigate the effect of shape factor on calibration curves. The three models had an outer diameter of 20 mm and shape factor of $\lambda = 2$. These rings had initial heights of 16, 12, and 8 mm, and IDs of 4, 8, and 12 mm. Figure 3.13 shows the calibration curves of these models. Although the shape factor was the same, the calibration curves were considerably different. For $m \leq 0.15$, the curve of Case III was located between the curves of Cases I and II. For $m > 0.15$, Case I had the highest curve, Case II was in the middle, and Case III had the lowest curve. Case I had the highest curve for all the values of friction coefficient. As discussed in Section 3.2, this result could be due to the force and displacement of these models and could be different for different geometries or materials. Thus, different rings with the same shape factor produce entirely different calibration curves.

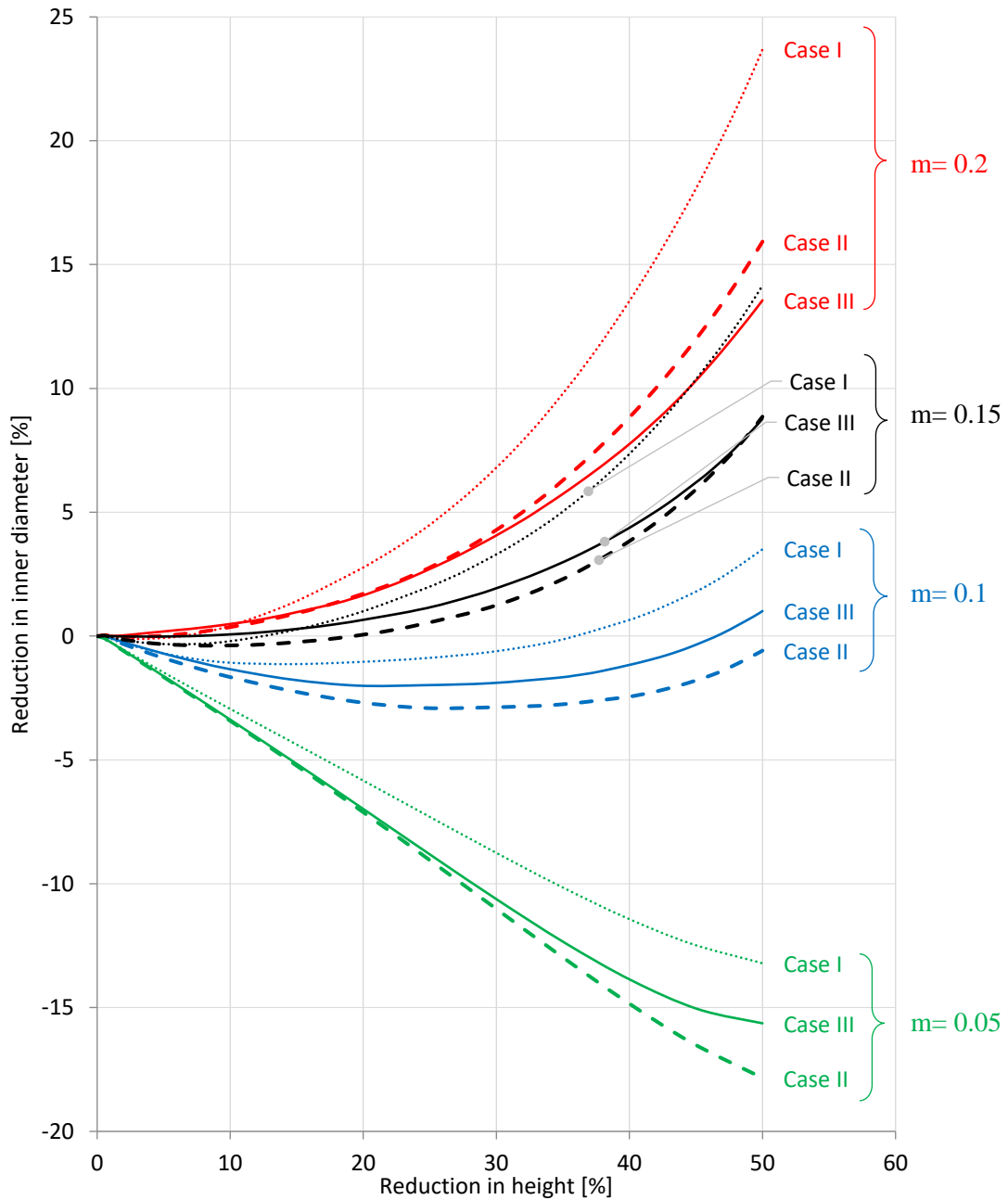


Figure 3.13: Calibration curves for different rings with the same shape factor of $\lambda = 2$.

Figure 3.14 compares the calibration curves of two rings with the same geometric ratio (6:3:2), that is, 18:9:6 mm and 15:7.5:5 mm (OD:ID:H). The models had a shape factor of $\lambda = 1.3$. Both models provided the same curve when $m = 0$. However, the difference was

considerable for other friction coefficients. For example, the difference was approximately 14% when $m = 0.3$ at 50% compression.

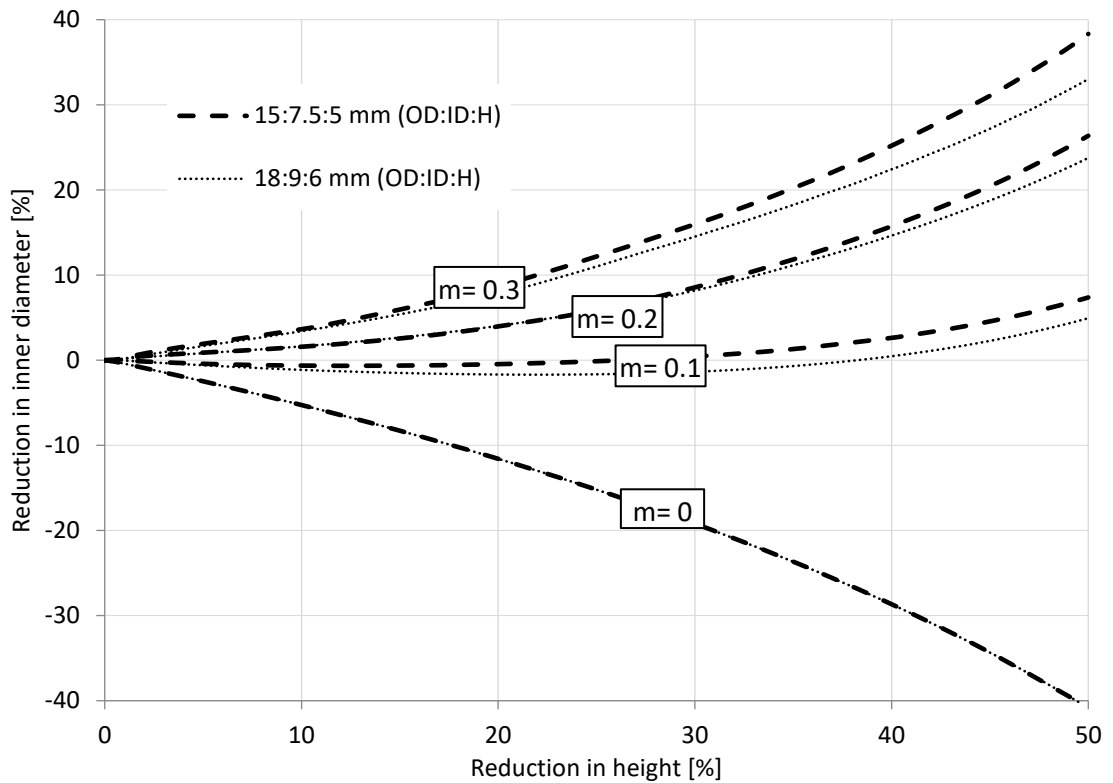


Figure 3.14: Calibration curves for different rings with the same geometric ratio (6:3:2).

The effect of friction on the f - d curve of compressed rings is shown in Figure 3.15. As expected, the higher the friction was, more load and consequently energy was required to compress the parts.

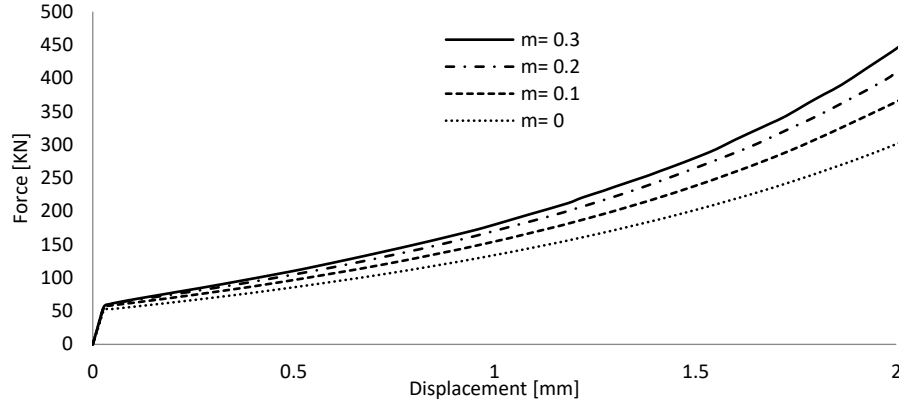


Figure 3.15: Effect of friction on f–d diagrams for the 17:7.5:5 mm (OD:ID:H) model.

3.6 Effects of material and test parameters

A Johnson–Cook (J–C) material model was used to investigate the effect of material and test parameters, such as strain hardening, strain rate sensitivity, and temperature, on the ring compression test. The corresponding J–C equation is expressed as follows:

$$\sigma_{eq} = [A + B\varepsilon_p^n] \left[1 + C \ln \left(\frac{\dot{\varepsilon}_p}{\dot{\varepsilon}_0} \right) \right] \left[1 - \left(\frac{T - T_0}{T_m - T_0} \right)^m \right] \quad (3.1)$$

where σ_{eq} is the effective stress; A, B, C, n, and m are the material parameters; ε_p is the effective plastic strain; $\dot{\varepsilon}_p$ is the effective plastic strain rate; $\dot{\varepsilon}_0$ is the reference strain rate; T is the working temperature; T_0 and T_m denote the room and melting temperatures, respectively.

The constants of this model for aluminum alloy 6061-T6 are presented in Table 3.1 [Lesuer et al, 2001].

Table 3.1. Input parameters for the J–C plasticity model [Systèmes, 2012].

Material	A (MPa)	B (MPa)	n	C	m	$\dot{\epsilon}_0$ (1/s)	T_m (K)	T_0 (K)
AA6061-T6	324	114	0.42	0.002	1.34	1.0	925	293.2

ABAQUS/Explicit package was used in the studies. To verify the simulations, a ring with a power law material and axisymmetric model was compressed in ABAQUS/Standard and Explicit, and the results were compared. The comparisons are shown in Figure 3.16 for stress–strain, reduction in diameter–reduction in height, and f–d curves. A simulation was conducted on another geometry, and the result was compared to that of Hartley et al. [Hartley et al., 1981]. The comparison is shown in Figure 3.17. The result was acceptable for the verification of the simulation in this thesis. A better material model and mesh could lead to a more accurate result. The J–C model was assigned to the part section as the base material of the 18:9:6 mm (OD:ID:H) model.

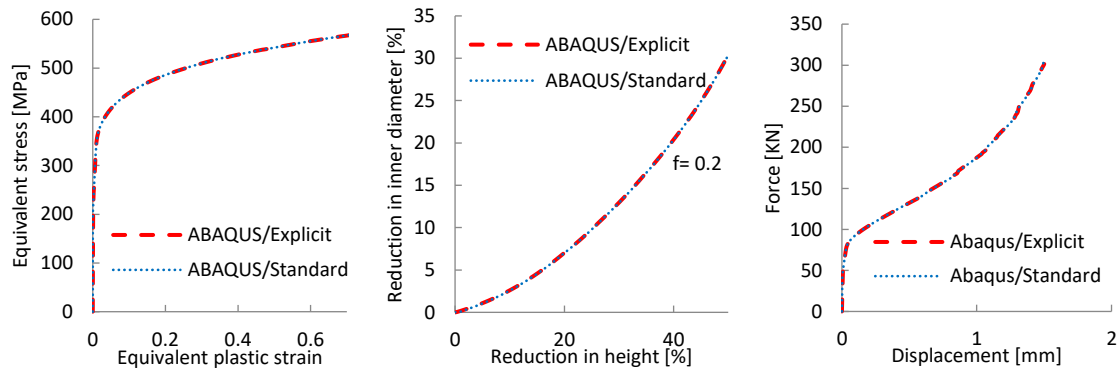


Figure 3.16: Comparison of results in ABAQUS/Standard and Explicit.



Figure 3.17: Comparison of (a) the result of experiment from a paper [Hartley et al., 1981] with (b) the result of simulation for the verification of procedure in ABAQUS.

3.6.1 Effect of strain hardening parameter

Three values of $n = 0.21, 0.42$ (base model), and 0.63 were used in the J–C material model to determine the effect of strain hardening on the compression tests. The results are shown in Figure 3.18. The ring had an OD of 18 mm, ID of 9 mm, and H of 6 mm, and the symmetry along the x-direction was used to simulate the model. Therefore, the displacement of 1.5 mm (in the y-direction) was equivalent to 50% compression.

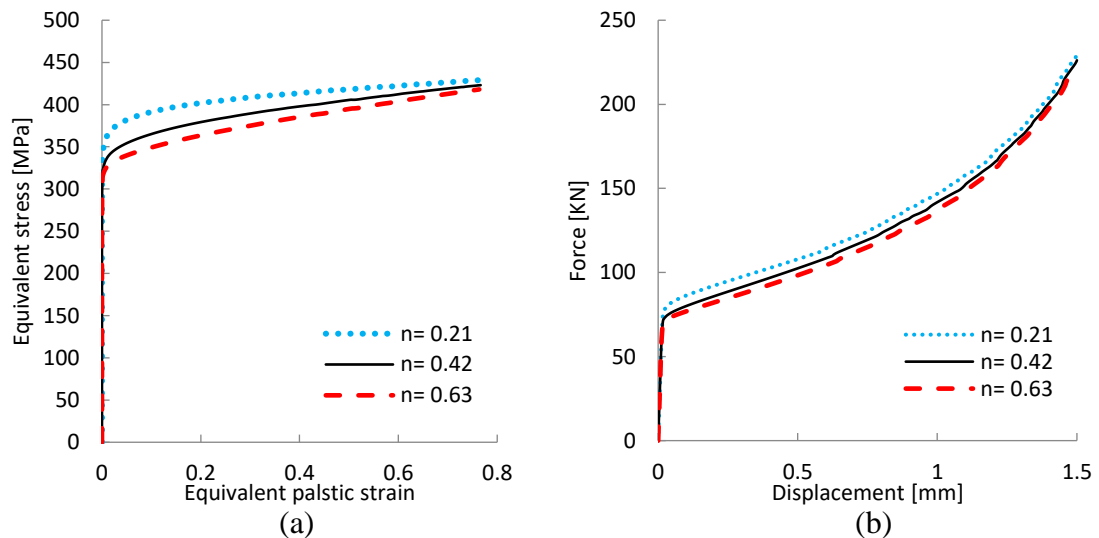


Figure 3.18: Effect of strain hardening on (a) stress–strain and (b) f–d curves.

As shown in Figure 3.18.b, the model with lower value of strain hardening parameter required more load under the same amount of compression. This condition is in agreement

with the corresponding stress–strain curve because applying considerable forces in the same conditions would result in greater stress in the structure. The effect of strain hardening was not evident at the end of compression. However, tripling the strain hardening parameter (from 0.21 to 0.63) resulted in approximately 15% less force at 3% compression.

3.6.2 Effect of strain rate sensitivity parameter

The selected material in these studies had a relatively low value of strain rate sensitivity parameter ($C = 0.002$). The strain rate sensitivity of the material should have high values to determine its effect, and the test speed should increase. On this basis, three values of $C = 0.002$ (base model), 0.500, and 0.850 were selected. The compression tests were conducted at three different speeds of $v = 0.15, 1.5, \text{ and } 15 \text{ mm/s}$. These velocities were constant during compression. The results are shown in Figures 3.19 and 3.20.

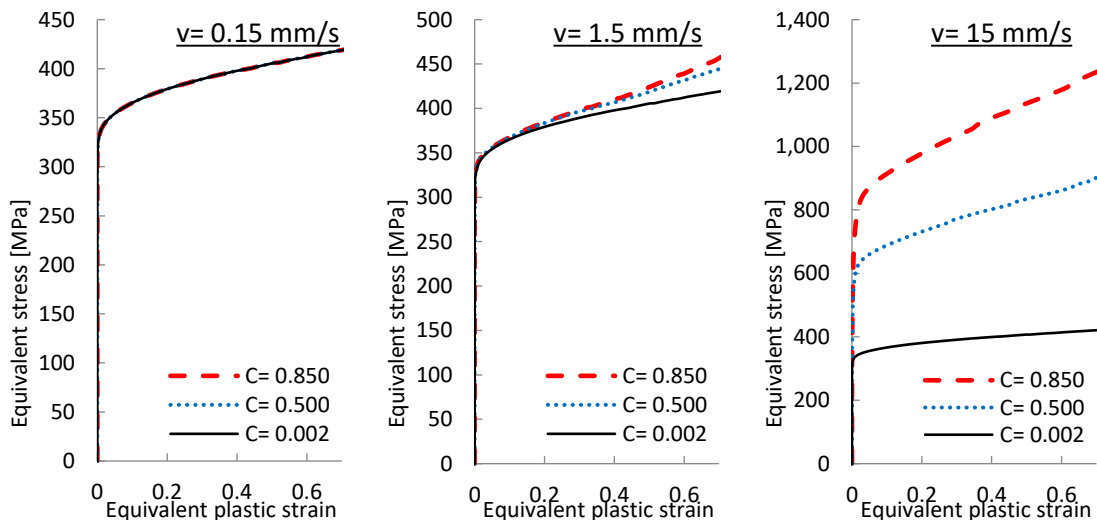


Figure 3.19: Effect of strain rate sensitivity on stress-strain curves.

The effect of strain rate sensitivity parameter was not observed unless the velocity was high. In this case, no difference was observed for $v = 0.15 \text{ mm/s}$. This finding indicated

that this speed was relatively low for this test to affect the results. The difference became prominent at the velocity of 1.5 mm/s. As shown in Figure 3.20, the difference between the f - d curves was not considerable at $v = 1.5$ mm/s. However, the strain rate sensitivity parameter had become more than 400 times larger (from the black line to the red one), as shown in Figure 3.21. A relatively high speed of 15 mm/s made it possible to observe the effect of these changes. The values of stress-strain and f - d curves had become approximately three times larger when C is increased from 0.002 to 0.85.

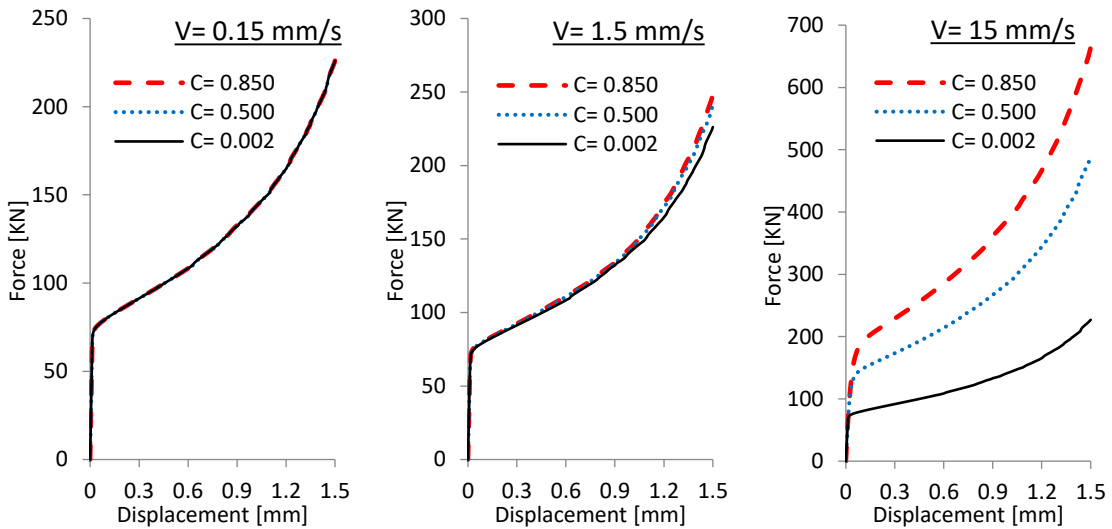


Figure 3.20: Effect of strain rate sensitivity on f - d curves.

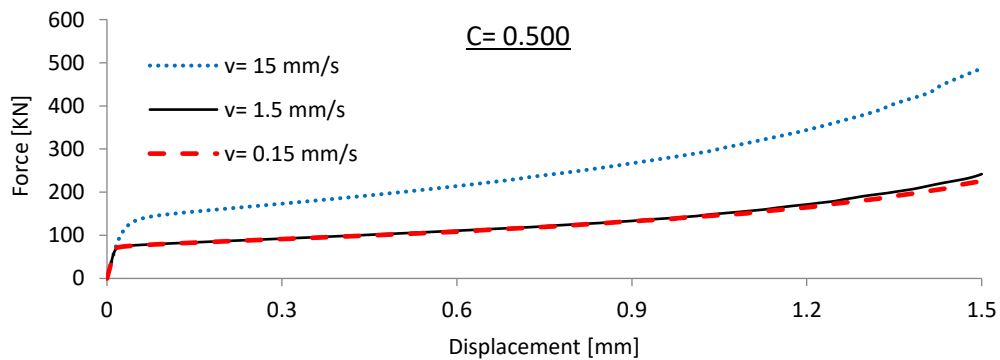


Figure 3.21: Effect of velocity on f - d curves for $C = 0.500$.

3.6.3 Effect of temperature

Temperature was directly added to the calculations as a constant predefined field in ABAQUS. The initial temperature was considered the room temperature in the third bracket of J–C material model. Here, the values of 200 °C and 300 °C were selected. Figure 3.22 shows the effect of elevated temperatures on stress–strain and f–d curves. As expected, the material became soft and required few loads to be compressed at high temperatures. Consequently, the curves were located lower at high temperatures. In comparison with the other two parameters (n and m) that did not affect the results evenly, the temperature change created nearly parallel curves (for stress–strain) or curves scaled at a constant rate (for f–d). For example, the value of force dropped by 31% at displacements of 0.5 and 1.5 mm from room temperature to 300 °C.

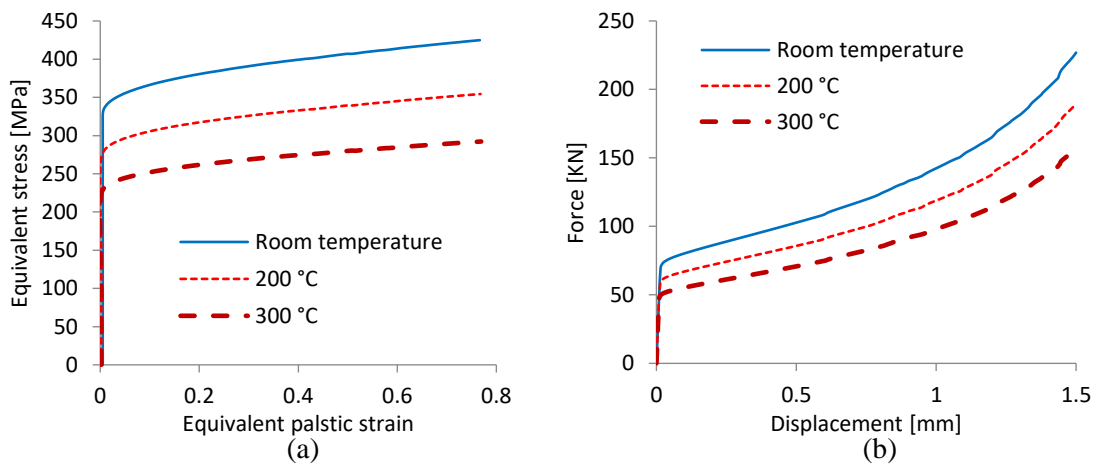


Figure 3.22: Effect of working temperature on (a) stress–strain and (b) f–d curves.

3.7 Effect of hydrostatic pressure on deformation mechanism of the ring

Shear bands play an important role in the failure mechanism of components made of ductile materials. Therefore, the strain localization in parts subjected to extreme deformations should be investigated. This topic has been investigated by many researchers (e.g., [Li et al., 2010] and [Liu et al., 2006]) by subjecting the rings to hydrostatic pressures. This section aims to investigate the plastic strain localization in the compressed rings and determine the influence of hydrostatic pressures at the inner and outer surfaces.

Friction coefficient of 0.2 and 30% compression were selected to compare the inward and outward material flows. The ring had a geometric ratio of 6:3:2 and an OD of 18 mm. Hydrostatic pressures of 0–500 MPa were applied to the inner and outer surfaces of the ring, which was then compressed. Figure 3.23 shows the plastic strain localization in the ring with and without hydrostatic pressure. The material was pushed outward when the inner surface was subjected to hydrostatic pressure. This condition became evident with the inner pressure of 500 MPa where barreling was hardly observed.

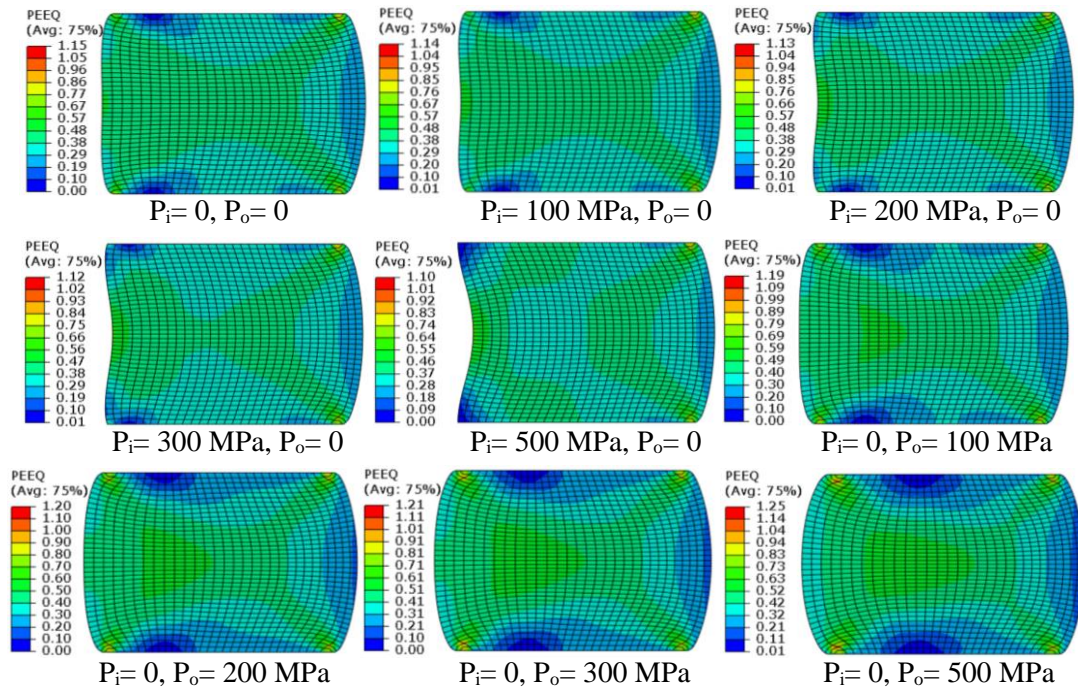


Figure 3.23: Effect of hydrostatic pressure on plastic strain localization.

Inward material flow was observed when an external pressure was applied. The material tended to flow outward under low friction conditions due to the nature of the test. This result occurred because the area of the outer surface was high, and small resistance occurred in that direction. In other words, the expansion of the outer radius of the ring was easier compared with the shrinking of the inner radius, as shown in the left image of Figure 3.25 where positive radial stress was observed more at the outer wall than the inner wall. This result showed the tendency of the material to expand at this region, indicating that outward material flow was noticeable. Figure 3.24 clearly shows the localization of plastic deformation in different cases. In this figure, regions with more than 40% equivalent plastic strain are highlighted in red. Few areas with plastic strain of greater than 0.4 were observed in the presence of internal hydrostatic pressure. The outer corners of the ring experienced

high levels of plastic strain localization nearly in all cases. These extreme plastic deformations could lead to crack initiation at these corners. These conditions were the same for the middle of the inner surface, which experienced large plastic deformations. Thus, the fracture line could connect the corners of the outer wall to the middle of the inner wall.

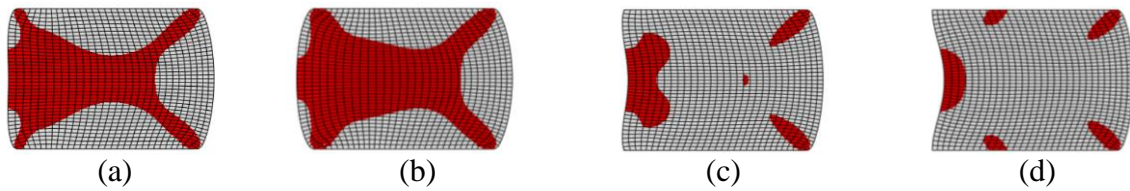


Figure 3.24: Plastic strain localization of more than 40%: (a) $P_i = 0$, $P_o = 0$; (b) $P_i = 0$, $P_o = 300$ MPa; (c) $P_i = 300$ MPa, $P_o = 0$; (d) $P_i = 500$ MPa, $P_o = 0$.

The presence of tensile stress area at the outer surface of the ring subjected to axial compression could lead to crack initiation [Liu et al., 2006]. Therefore, this state of stress should be eliminated at this region. Figures 3.25 and 3.26 show the radial and tangential stress distributions at the cross section of the ring in different cases. The state of radial stress at the outer wall changed from compressive to tensile when hydrostatic pressure of approximately 100 MPa was applied. The tensile radial stresses at the corners of the inner wall required less than 100 MPa pressure to become compressive.

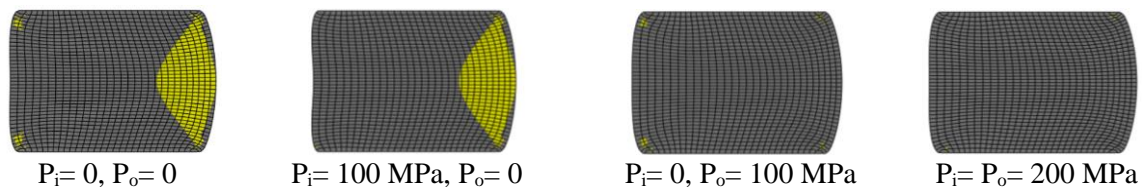


Figure 3.25: Distribution of radial stress; compressive stress in grey, and tensile stress in yellow.

As shown in Figure 3.26, the tensile state of tangential stresses were less distributed across the cross section of the ring. Although hydrostatic pressure of 200 MPa was applied at both

walls, this component did not become compressive at all areas because the direction of its vector was not directly affected by the applied hydrostatic pressure.

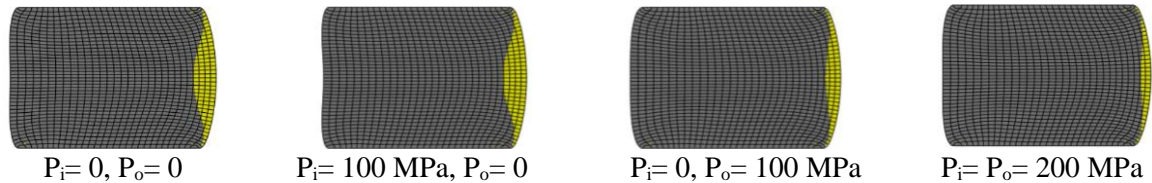


Figure 3.26: Distribution of tangential stress; compressive stress in grey, and tensile stress in yellow.

3.8 Conclusion

Rings with different shape factors but the same outer diameter were subjected to static axial loading, and their f - d curves were plotted. The f - d curves of rings with high shape factor were located lower in the plots. A similar value of displacement was obtained for the rings with the same shape factor and outer diameter, at which equal amount of work for the compression of the rings was done.

Calibration curves for different rings were produced. Rings with the same shape factor but different dimensions produced different calibration curves. Rings with the same geometric ratio but different dimensions produced entirely different calibration curves.

The effects of material properties on f - d and stress-strain curves of the rings subjected to axial loading were investigated. The increase of strain hardening parameter caused the curves to be placed lower on the plots. The corresponding parameter in the material model and test speed should be sufficiently high to observe the effect of strain rate sensitivity. The more rate sensitive the material is, the higher the values of force and stress will be obtained.

The effect of hydrostatic pressure on the deformation mechanism of the rings was evaluated. The application of hydrostatic pressure at the inner and outer walls played an important role in the stress distribution and plastic strain localization in the cross section of the ring. The tensile state of radial and tangential stresses could be transformed to compressive. Therefore, subjecting the ring to a hydrostatic pressure during compression could delay crack initiation and result in the enhancement of ring compressibility.

Chapter 4 Thin-walled tubes under dynamic axial loading

4.1 Introduction

Crashworthiness of thin-walled structures as energy absorbers have been widely investigated in the past few decades. Tubes with different geometries have been subjected to axial static-quasi and dynamic loads. Among the other cross sections, circular tubes are the most common specimens used for analysis because they can be easily manufactured at a low cost [Jones, 2012; Tarlochan et al., 2013]. Crash response analysis of a device is started by plotting its corresponding f - d curve, as shown in Figure 4.1.

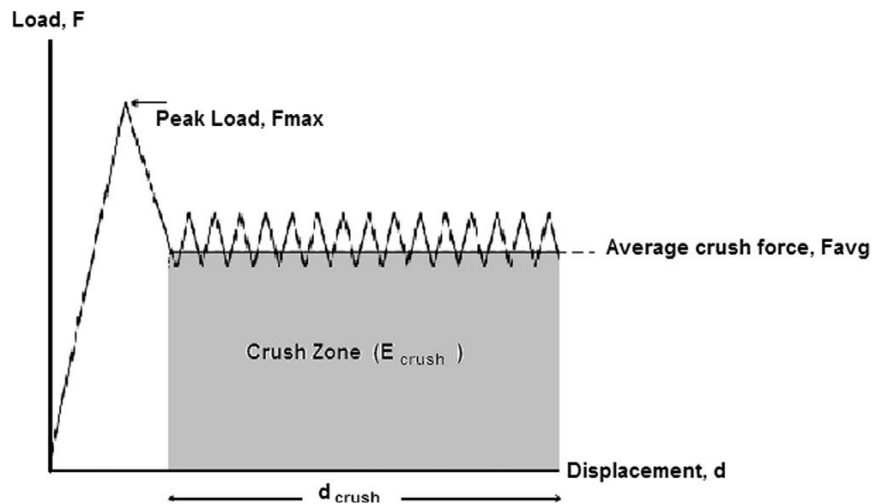


Figure 4.1: Typical f - d diagram [Tarlochan et al., 2013].

For the crash response of structures, the following parameters are used as performance indicators [Lu et al., 2006; Tarlochan et al., 2013; Eyvazian et al., 2014]:

- EA : The area under the f - d diagram is considered the total energy that a structure dissipates during impact, which is expressed as

$$E = \int_{d_0}^{d_{max}} F \cdot ds \quad (4.1)$$

where d_0 is the initial deformation point, and d_{max} is the maximum displacement.

This value is obtained by numerical integration of the f - d curve.

- *Peak force (F_{max}):* This parameter denotes the maximum value of load in the diagram that results in plastic deformation of the structure. Peak load can occur in the beginning or at the end of the stroke when it is relatively high depending on the geometry and material properties of the energy absorber. The peak load should be kept low as the average force.
- *Mean crushing force (F_{avg}):* Mean force is the average of crash force response of the structure during plastic deformation., which can be expressed as:

$$F_{avg} = \frac{EA}{d_{max}} \quad (4.2)$$

- *Crush force efficiency (CFE):* CFE is the ratio of the average load to the peak load as follows:

$$CFE = \frac{F_{avg}}{F_{max}} \quad (4.3)$$

Keeping this ratio close to one results in small changes in the deceleration and a good performance of an energy absorber. An ideal structure should cause a uniform deceleration during the entire impact.

- *Stroke efficiency (SE):* Stroke efficiency is considered a measure of geometric performance and is the ratio of crush length or displacement to the initial length (L), that is expressed as follows:

$$SE = \frac{d_{max}}{L} \quad (4.4)$$

- *SEA*: *SEA* is an important parameter in the design of energy-absorbing devices and is defined as the ratio of the energy absorbed to the mass of the structure, which is expressed as:

$$SEA = \frac{EA}{m} \quad (4.5)$$

where m is the mass of the energy absorber. This indicator, energy absorbed per unit mass, is used to compare the performance of structures with different weights.

In general, the value of peak force should be kept low and close to the mean force with high values of EA and SEA [Shinde et al., 2018].

In this chapter, the effects of different parameters, such as material strain rate sensitivity, strain hardening, friction coefficient, test speed, and temperature, on the crushing behavior of circular tubes are numerically investigated using ABAQUS software. In addition, crashworthiness of corrugated tubes with different number of grooves and groove sizes is evaluated. In the last section of this chapter, the effect of wall thickness on EA capacity of corrugated tubes is assessed.

4.2 FE configuration of the base model in ABAQUS

4.2.1 Verification of simulation process in ABAQUS

ABAQUS/Explicit software was used to numerically investigate the behavior of structures subjected to axial dynamic loading. In this case, a typical FE model comprising a top platen, a specimen, and a bottom platen was used, as shown in Figure 4.2. The top platen had an isotropic mass of 275 kg assigned to its reference point with an initial velocity of 15.6 m/s.

Impact velocity of 15.6 m/s (35 mph) was selected in accordance with the National Highway Traffic Safety Administration front crash standard [Tarlochan et al., 2013]. The top and bottom platens were considered rigid bodies during the simulations. Thin-walled tubes were modeled using four-node shell elements with five integration points through the wall thickness, enhanced hourglass control, and reduced integration, as suggested by Tarlochan [Tarlochan et al. 2013]. To produce the f–d diagrams, the load was read from the reference point of the bottom platen, which was fixed, and the displacement was obtained from the movement of top platen in z-direction, as shown in Figure 4.2.

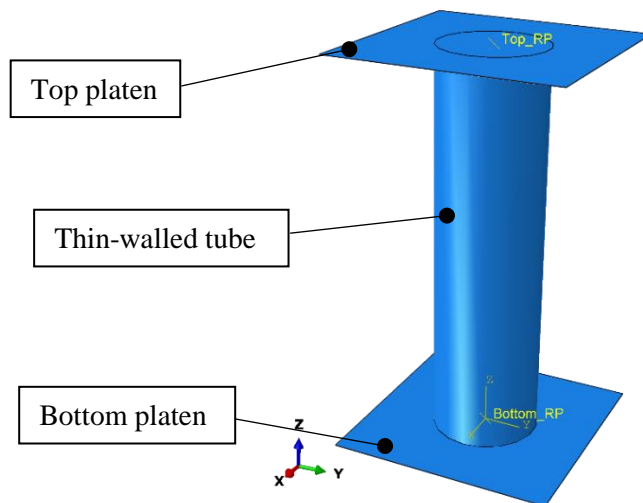


Figure 4.2: Typical FE model in ABAQUS for axial impact test.

To verify the simulations presented in this thesis, a circular tube with a diameter of 95.5 mm, length of 350 mm, and thickness of 2 mm was modeled in ABAQUS and subjected to an axial crushing load, as previously explained. The results were compared with those of Tarlochan et al. [2013]. The comparison between these simulations is shown in Figure 4.3 and Table 4.1. Evidently, the two models deformed with two concertina modes, followed by three diamond lobes. The peak force obtained in this verification simulation was 211.24

KN compared with 207.84 KN from the paper (1.5% difference), and EA was 24.18 kJ compared with 23.67 kJ (2% difference). The main source of these differences could be the mesh and sampling sizes. The curve trend and CFE (0.55) were the same in both cases.

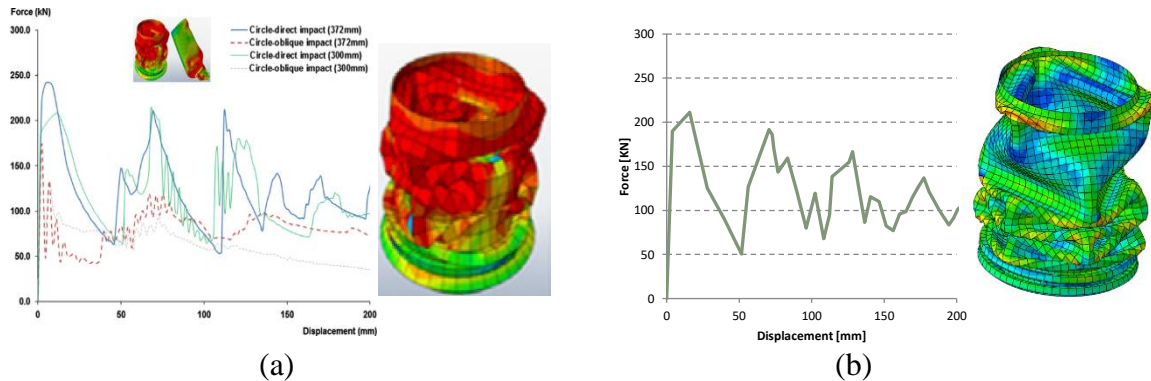


Figure 4.3: Comparison of (a) the result of FEA from a paper [Tarlochan et al., 2013] with (b) the result of simulation for the verification of procedure in ABAQUS.

The procedure was correctly defined in ABAQUS/Explicit. The comparisons are presented in Table 4.1.

Table 4.1. Comparison of simulations in ABAQUS.

Profile 	Perimeter (mm)	Length (mm)	Mass (Kg)	Dia. (mm)	Thickness (mm)	
	300	350	1.7	95.5	2	
			EA (KJ)	F_{max} (KN)	F_{avg} (KN)	CFE
Result from paper [Tarlochan et al., 2013]			23.67	207.84	114.58	0.55
Result of simulation in ABAQUS for this thesis			24.18	211.24	117.13	0.55

Table 4.2. Input parameters for the J–C plasticity model [Tarlochan et al., 2013; Systèmes, 2012].

Parameter	Material		
	ASTM A36 Steel	Aluminum Alloy 6061	AISI 4340 Steel
Yield stress, A (MPa)	146.7	324.1	792
Strain hardening parameter, B (MPa)	896.9	113.8	510
Strain hardening exponent, n	0.32	0.42	0.26
Strain rate sensitivity parameter, C	0.033	0.002	0.014
Temperature exponent, m	0.323	1.34	1.03
Reference strain rate, $\dot{\epsilon}_0$ (1/s)	1.0	1.0	1.0
Melting temperature, T_m (K)	1773	925	1793
Transition temperature, T_0 (K)	293.2	293.2	293.2

The material used in this study was ASTM A36 steel with J–C constitutive relation, with the following equation and parameters shown in Table 4.2:

$$\sigma_{eq} = [A + B\varepsilon_p^n][1 + C \ln(\dot{\epsilon}^*)][1 - T^{*m}] \quad (4.6)$$

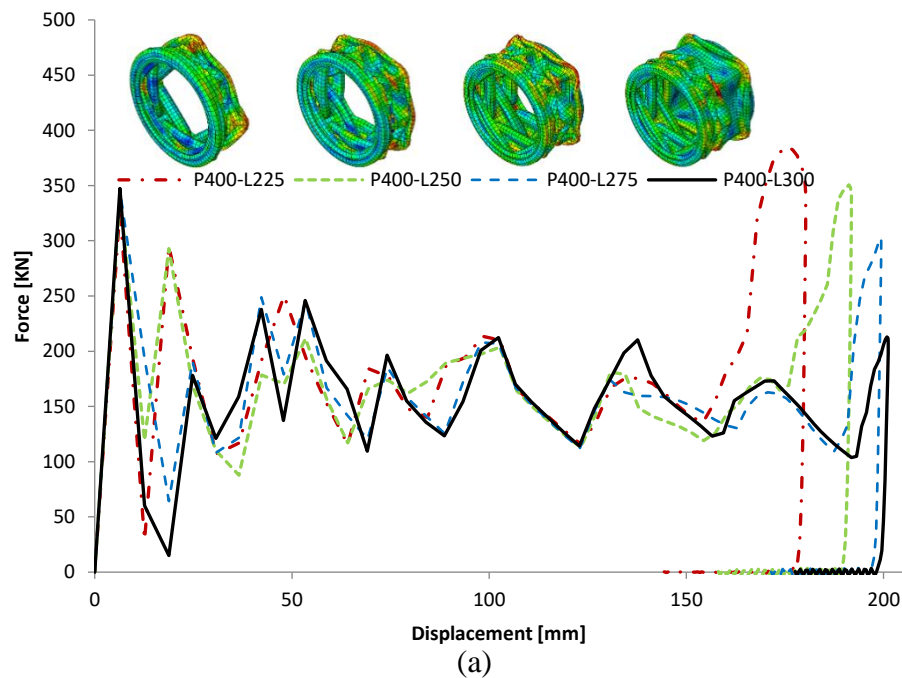
where A, B, C, n, and m are the material parameters; ε_p is the effective plastic strain; $\dot{\epsilon}^*$ ($= \frac{\dot{\epsilon}_p}{\dot{\epsilon}_0}$) is a dimensionless strain rate; $\dot{\epsilon}_p$ is the effective plastic strain rate; $\dot{\epsilon}_0$ is the reference strain rate; T^* ($= \frac{T-T_0}{T_m-T_0}$) is a dimensionless temperature; T is the working temperature; and T_0 and T_m are the transition and melting temperatures, respectively. The temperatures below the transition temperature do not affect the yield equation. The transition temperature is usually substituted by room temperature. In Table 4.2, the summary of J–C parameters for two other materials are presented for comparison with that used in this study [Systèmes, 2012].

4.2.2 Selection of base circular model for FEA

A circular tube with a perimeter of 400 mm (diameter of 127.3 mm) and thickness of 2 mm was used as the base model for FEA in ABAQUS.

Table 4.3. Comparison of EA capacity and CFE of circular tubes for the selection of a proper tube length.

Model	Shell Thickness [mm]	Profile Perimeter [mm]	Length [mm]	Peak Force [KN]	Mean Force [KN]	CFE	Energy Absorbed [KJ]
P400-L300	2	400	300	347.38	155.92	0.45	28.42
P400-L325	2	400	325	347.67	157.53	0.45	28.78
P400-L350	2	400	350	346.25	159.95	0.46	29.28
P400-L375	2	400	375	343.99	155.06	0.45	28.15
P400-L400	2	400	400	342.18	153.52	0.45	27.83
P400-L425	2	400	425	339.98	148.77	0.44	27.26
P400-L450	2	400	450	336.63	144.21	0.43	26.98
P400-L500	2	400	500	329.01	137.94	0.42	26.54



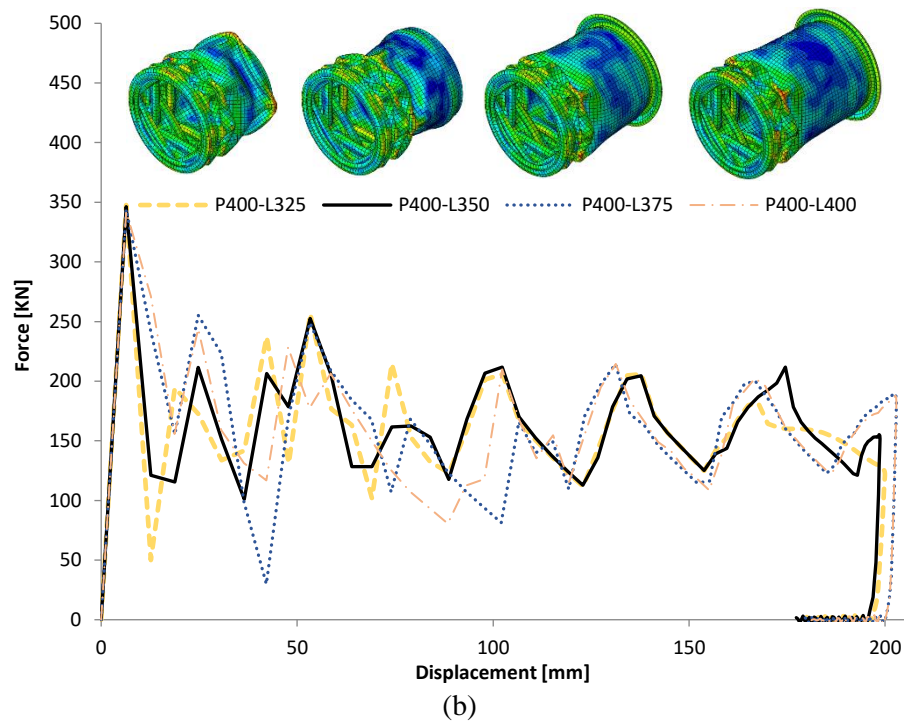


Figure 4.4: F–d diagrams for perimeter of 400 mm and lengths of (a) $L = 225\text{--}300$ mm and (b) $L = 325\text{--}400$ mm.

To select a proper tube length for the subsequent numerical studies, a series of simulations was performed on tubes with $L = 200\text{--}500$ mm by applying the FEA details stated in the previous section. A length of 350 mm was used for the model based on the EA capacity and CFE of the samples. The results are presented in Figure 4.4 and Table 4.3. A mesh convergence study was conducted to select a suitable mesh size for the base model, as shown in Figures 4.5–4.7. In comparison with a mesh size of 1 mm, a mesh size of 4 mm did not significantly affect the results and remarkably reduced the computation time.

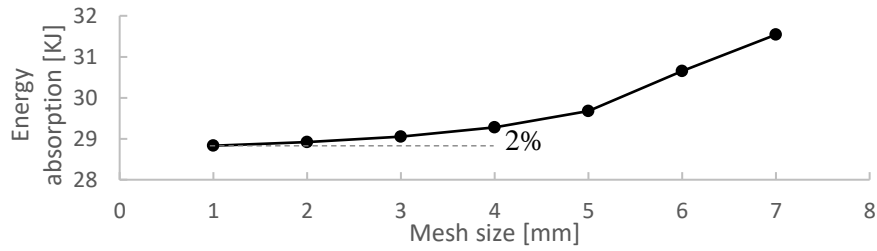


Figure 4.5: Mesh convergence study based on EA.

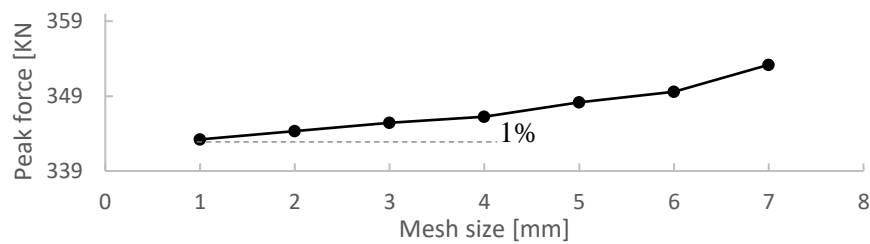


Figure 4.6: Mesh convergence study based on peak force.

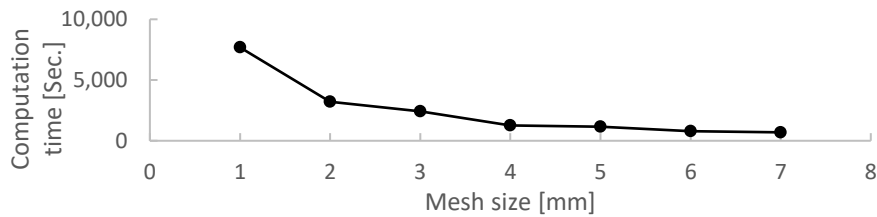


Figure 4.7: Mesh convergence study based on computation time.

4.3 Effects of test conditions

4.3.1 Effect of coefficient of friction

The base model (P400-L350) was simulated in ABAQUS/Explicit to determine the effect of friction coefficient on the EA characteristics of thin-walled tubes. Here, three friction coefficients of 0, 0.2, and 0.4 were used in the general contact property of the model. As shown in Figure 4.8, friction coefficient played an important role in the deformation pattern of the circular tube. High values of friction resulted in the formation of many concertina

patterns, whereas slip existed between the top platen and the upper edge of the tube without friction. In these simulations, the bottom platen was fixed, and the lower edge of the tube was constrained to the bottom platen. This type of constraint is used in experiments. The formation of concertina mode in progressive buckling resulted in high stroke and geometrical crush efficiency. As shown in Figure 4.9 and Table 4.4, friction coefficient of 0.4 resulted in higher EA and CFE of the model compared with $f = 0.2$; however, this effect was insignificant. The increase in EA was approximately 1% when the friction coefficient was doubled.

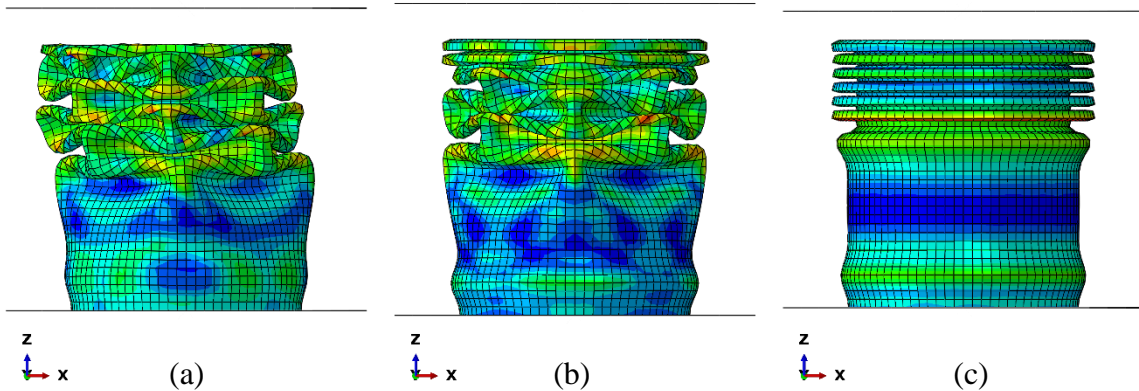


Figure 4.8: Effect of friction coefficient on P400-L350; (a) $f = 0.0$, (b) $f = 0.2$, (c) $f = 0.4$.

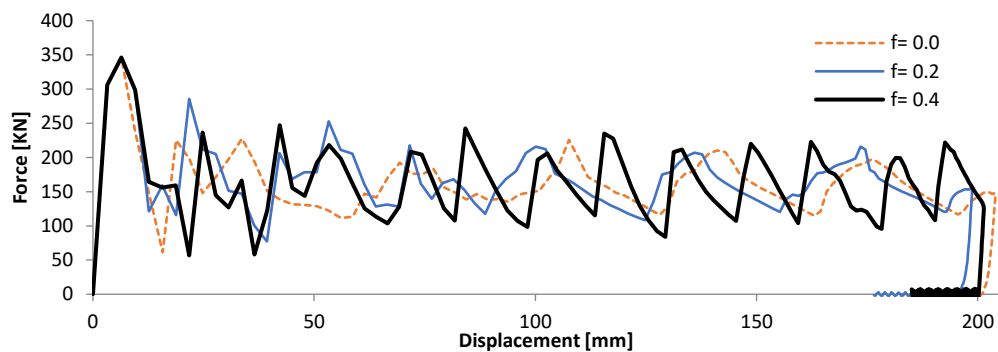


Figure 4.9: F–d diagrams for P400-L350 model with different friction coefficients defined in the contact property.

Table 4.4. Comparison of EA capacity and CFE of P400-L350 model with different friction coefficients.

Model	Coefficient of friction	Peak Force [KN]	Mean Force [KN]	CFE	Energy Absorbed [KJ]
P400-L350	0.0	345.98	153.78	0.444	28.71
P400-L350	0.2	346.25	159.95	0.462	29.28
P400-L350	0.4	346.20	161.03	0.465	29.52

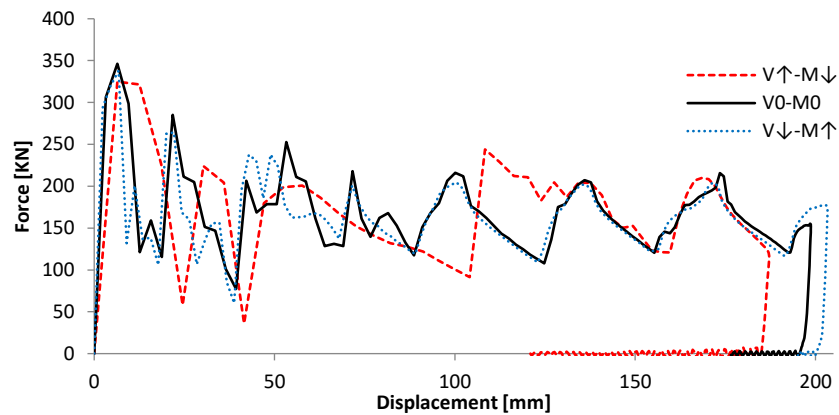
4.3.2 Effects of test speed and mass

Two simulations were conducted to determine the effect of test speed and mass, and their results were compared with the base model. In the first simulation, the initial velocity was doubled, and the mass was quartered ($V\uparrow-M\downarrow$). In the second analysis, the initial velocity was divided by the square root of 2, and the mass was doubled ($V\downarrow-M\uparrow$). The impact energy was kept constant with the selection of speed and mass. The comparison of the results with the base model (V_0-M_0) is illustrated in Figure 4.10 and Table 4.5. The response of the tube was highly dependent on the initial velocity of the impact or test speed. The differences in the peak and mean forces and in the CFE were small. However, the crush stroke was significantly affected by the impact velocity. For the case of doubling the test speed, the stroke decreased by approximately 6%, which directly resulted in approximately 12% less EA. By contrast, the crushing length increased by 2.3% when the impact velocity was divided by 1.41 (slow test), which resulted in 6.2% more EA. The response and behavior of the model under different initial impact velocities are related to the strain rate sensitivity

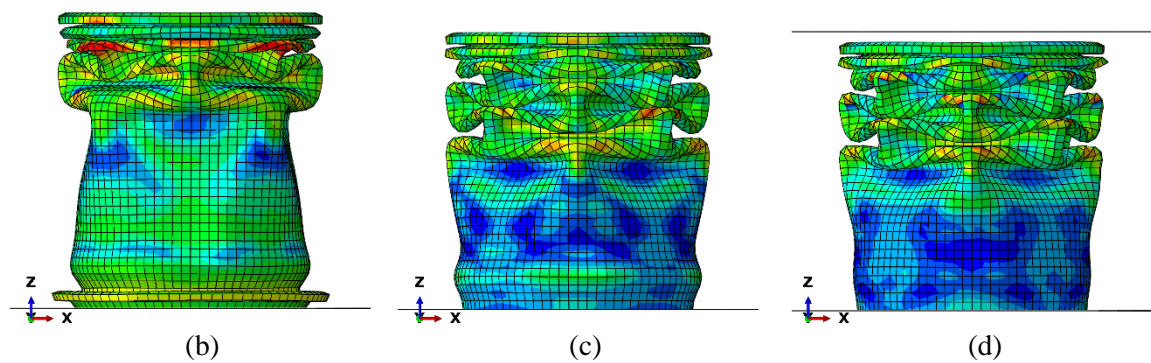
of the material. This topic will be discussed in the subsequent sections. The deformation mode in the slow and original test was the same, whereas the difference was significant in the rapid test.

Table 4.5. Effects of initial velocity and mass of impact on the EA capacity and CFE of P400-L350 model.

Model	Initial velocity [m/s]	Initial mass [Kg]	Peak Force [KN]	Mean Force [KN]	CFE	Energy Absorbed [KJ]
V0-M0	15.6	275	346.25	159.95	0.46	29.28
V \uparrow -M \downarrow	31.2	68.75	324.85	160.62	0.49	25.71
V \downarrow -M \uparrow	11.0	550	338.05	158.06	0.47	31.09



(a)



(b)

(c)

(d)

Figure 4.10: Effects of test speed and mass on the crushing behavior of circular tubes; (a) f-d diagrams; (b)–(d) deformation modes for V \uparrow -M \downarrow , V0-M0 (base model), and V \downarrow -M \uparrow , respectively.

4.3.3 Effect of temperature

Initial temperatures of 50 °C (323.2 K) and 100 °C (373.2 K) were defined in the analysis to determine the crushing behavior of circular tubes at high temperatures. The results are presented in Figure 4.11 and Table 4.6. As expected, the crushing distance increased, and high reaction force was observed at the end of the stroke at high temperatures. However, the crashworthiness of the component decreased. An initial temperature of 50 °C resulted in 3% reduction in CFE and 6% reduction in EA. At 100 °C, CFE decreased by 26% and EA decreased by 10%. The concertina patterns formed at the bottom of the tube at the initial stages of deformation with the increase in temperature. This deformation pattern is depicted in Figure 4.12. In the next section, the effect of temperature exponent will be investigated.

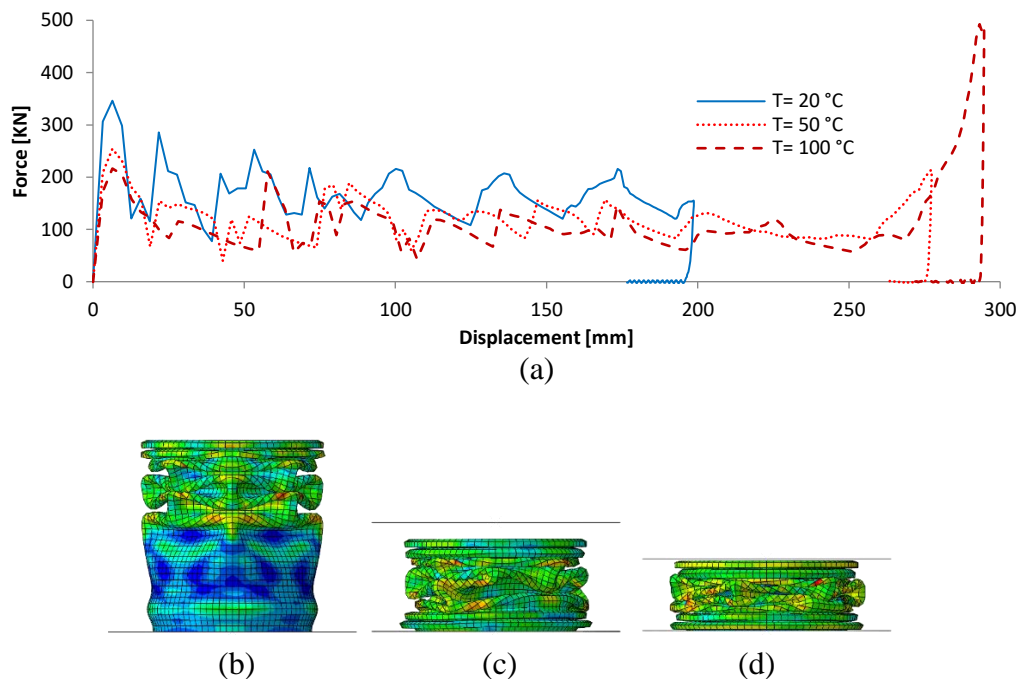


Figure 4.11: Effect of temperature on the crushing behavior of circular tubes; (a) f–d diagrams; (b) T = 20 °C (base model); (c) T = 50 °C; and (d) T = 100 °C.

Table 4.6. Effect of temperature on EA and CFE.

Model	Temperature [°K]	Peak Force [KN]	Mean Force [KN]	CFE	EA [KJ]
P400-L350	20	346.25	159.95	0.46	29.28
P400-L350	50	254.17	109.18	0.43	27.51
P400-L350	100	487.04	98.66	0.20	26.36

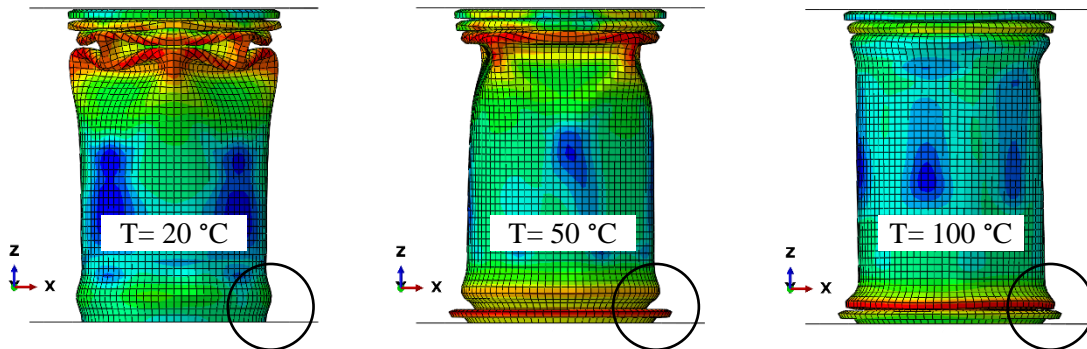


Figure 4.12: Formation of concertina modes at the bottom of the model at the initial stages of deformation under high temperatures (time frame = 50).

4.4 Effects of material properties

ASTM A36 steel from Table 4.2 was used in investigating the behavior of thin-walled tubes under dynamic loading in ABAQUS. Different parameters of the J–C material model were changed to compare their corresponding effects on the EA and CFE of the models. The other parameters and conditions were kept the same with the base model.

4.4.1 Strain rate sensitivity

Nine simulations were conducted to investigate the effect of strain rate sensitivity by combining the three values of strain rate sensitivity parameters and three initial velocities (as used in the previous section). The three initial impact velocities are V_0 (15.60 m/s), $2V_0$ (31.20 m/s), and $0.707V_0$ (11.03 m/s). The three strain sensitivity parameters are $C = 0.003$, $C = 0.033$ (base model), and $C = 0.333$. The results are shown in Figure 4.14 and

Table 4.7. The lesser strain rate sensitivity the material has, the higher EA capacity of the tube will be. The tube absorbed small energy at high impact velocities. The EA declined by 10% when the initial impact velocity was changed from 15.6 m/s to 31.2 m/s and $C = 0.333$, as shown in Figure 4.13.

Table 4.7. Effect of strain rate sensitivity on EA and CFE.

Model	Initial velocity [m/s]	Strain rate sensitivity parameter, C	Peak Force [KN]	Mean Force [KN]	CFE	EA [KJ]
V15.6-C0.003	15.6	0.003	308.27	146.24	0.47	29.46
V15.6-C0.033	15.6	0.033	346.25	159.95	0.46	29.28
V15.6-C0.333	15.6	0.333	677.21	273.25	0.40	25.97
V31.2-C0.003	31.2	0.003	298.18	147.91	0.49	26.23
V31.2-C0.033	31.2	0.033	324.85	160.62	0.49	25.71
V31.2-C0.333	31.2	0.333	774.39	299.25	0.39	23.50
V11.0-C0.003	11.0	0.003	302.90	137.05	0.46	31.42
V11.0-C0.033	11.0	0.033	338.05	154.06	0.46	31.09
V11.0-C0.333	11.0	0.333	644.45	241.37	0.37	26.95

At $C = 0.333$, the peak force was increased by 20% when the velocity was increased from 11.6 m/s to 31.2 m/s. Based on the values of CFEs, many nodal values and data should be gathered to address this ratio for small strain rate sensitivity parameters. As shown in Figure 4.14.d, changing the strain rate sensitivity resulted in the change in the progressive buckling deformation pattern of the models. Concertina deformation mode was observed at the bottom of the model with the increase in impact velocity. This result was evident for the model with the highest strain rate sensitivity parameter ($C = 0.333$).

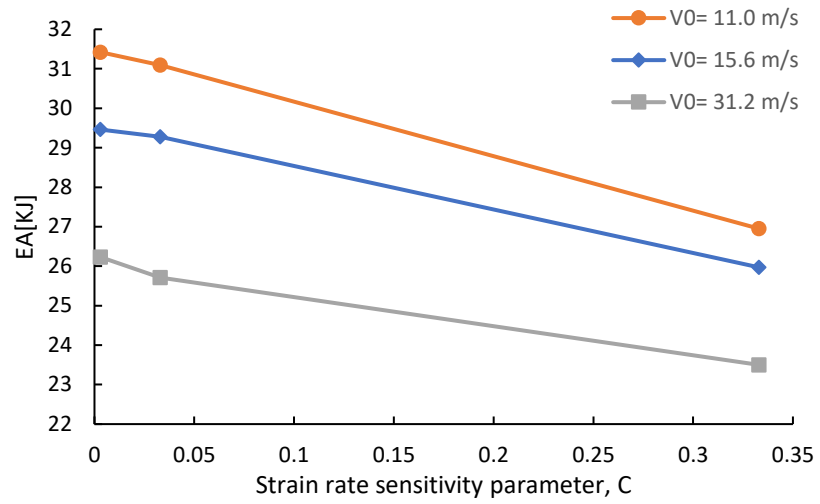


Figure 4.13: EA capacity versus strain rate sensitivity at different initial velocities.

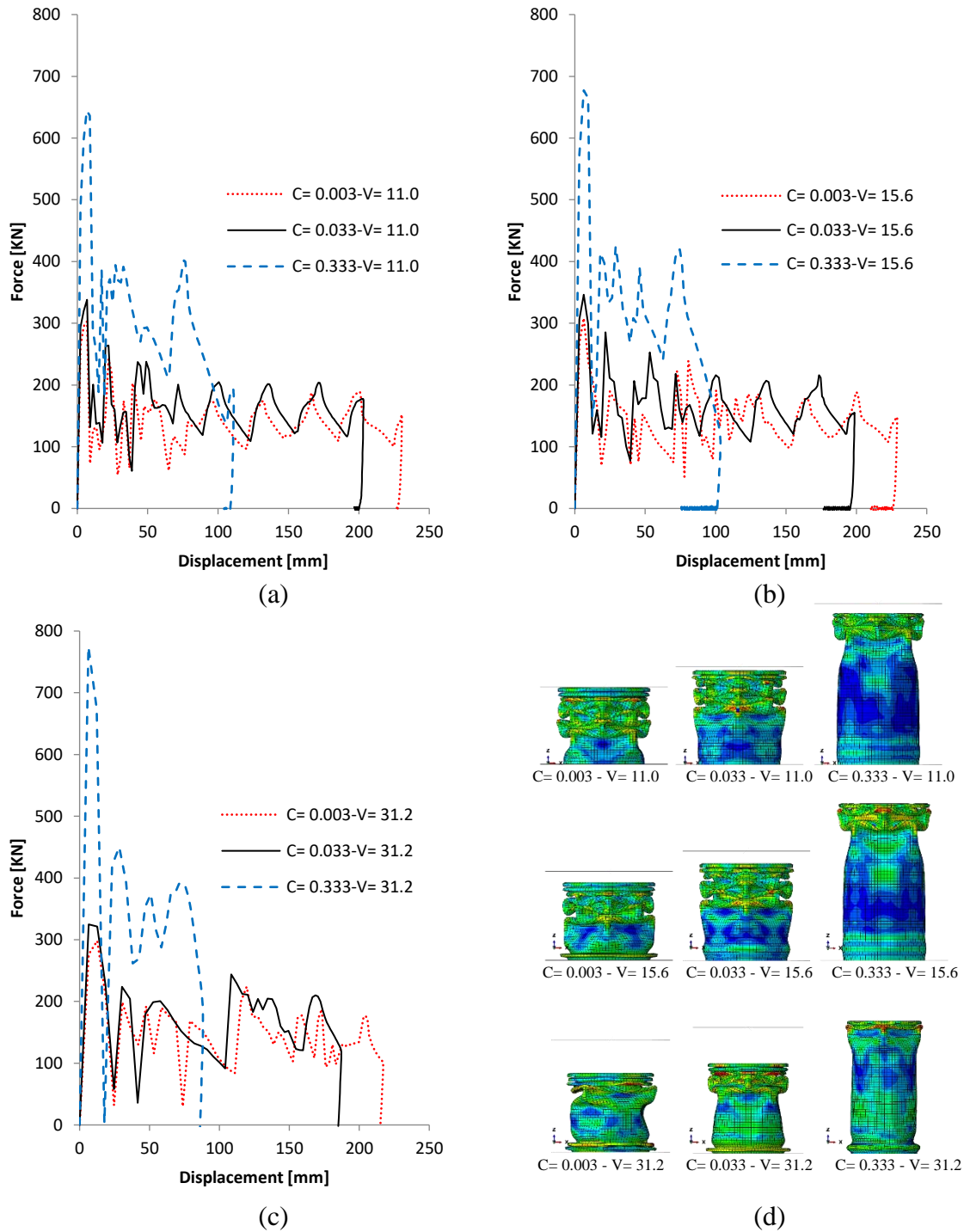


Figure 4.14: Effect of strain rate sensitivity with initial velocities of (a) 11.0 m/s, (b) 15.6 m/s, and (c) 31.2 m/s; (d) deformation modes.

4.4.2 Strain hardening

Five strain hardening parameters of $n = 0.08, 0.16, 0.32$ (base model), 0.48 , and 0.64 were defined in the J–C material model in ABAQUS. The strain hardening parameter played an important role in the EA characteristics of thin-walled tubes. As illustrated in Figure 4.15, the crushing stroke of the models increased with the strain hardening parameter, which also resulted in approximately 2% more EA when increasing from $n = 0.32$ to 0.48 . Moreover, CFE increased by 6%. However, EA decreased by 5% when strain hardening was increased to 0.64 (compared with $n = 0.48$). In this case, CFE decreased by 22%. In comparison with the strain rate sensitivity parameter that resulted in either reduction or increase of EA, an optimum value existed for the strain hardening parameter in which the maximum values of CFE and EA were obtained, as shown in Figure 14.16.

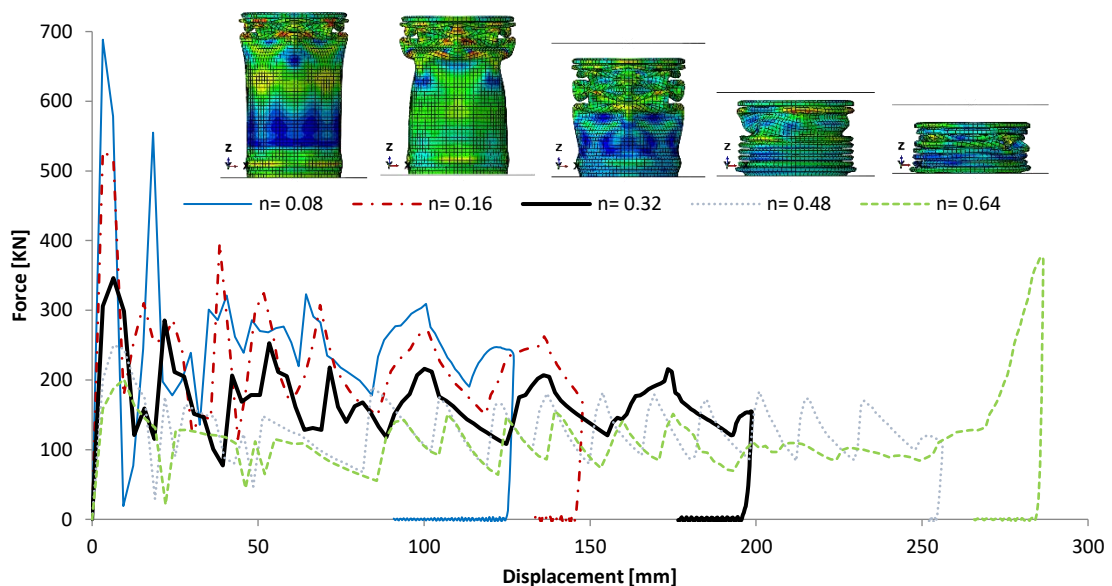


Figure 4.15: F–d diagrams for investigating the effect of strain hardening parameter.

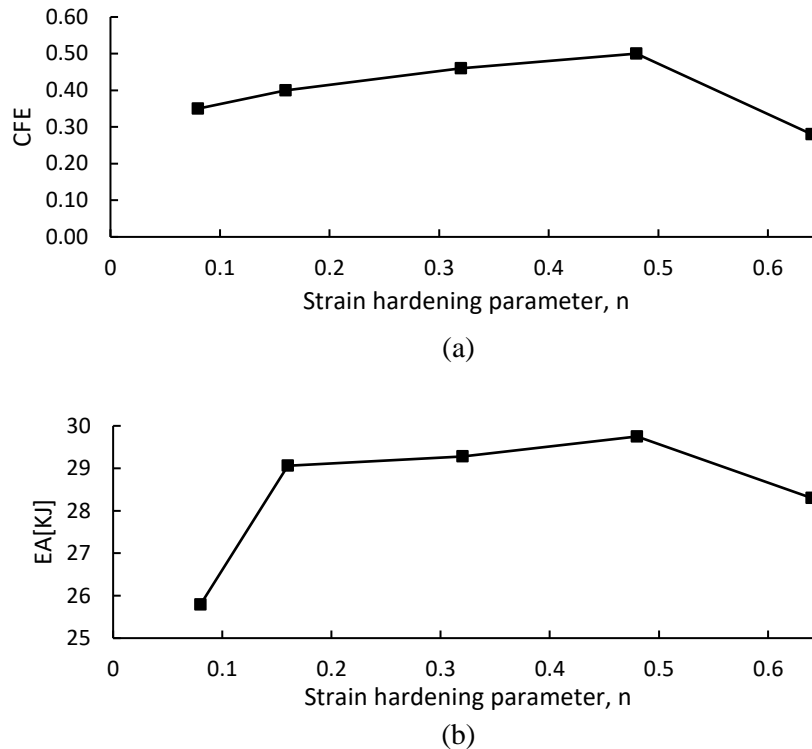


Figure 4.16: Effect of strain hardening parameter on (a) CFE and (b) EA.

4.4.3 Temperature exponent

Five exponents of $m = 0.1, 0.323$ (base model), 1.0, 1.5, and 3.0 were defined in the third bracket of the J–C model in ABAQUS. The results are shown in Figure 14.17. The EA characteristics of the model increased with the value of m . However, this improvement was less significant for values of m higher than unity. At $m \geq 1.5$, nearly no difference was observed in the EA of the model at room temperature or at 100 °C. As expected, the higher the temperature exponent is, the less temperature sensitive the model will be due to the nature of the J–C mathematical model.

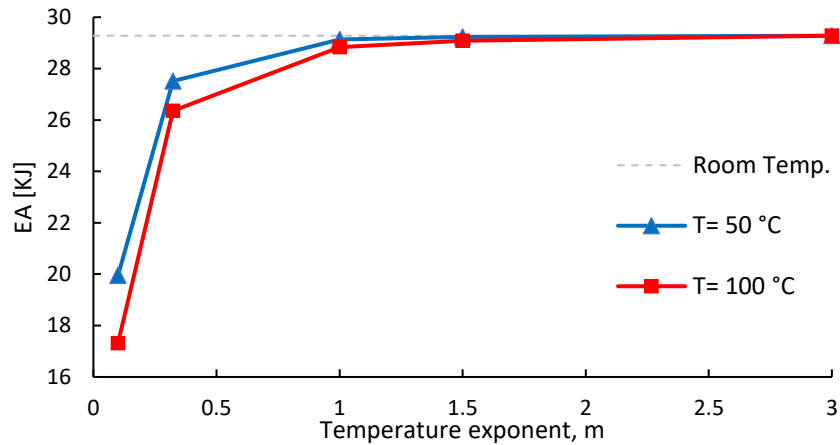


Figure 4.17: Effect of temperature exponent on (a) CFE, and (b) energy absorption.

4.5 Effect of geometry

4.5.1 Number of tubes

This section presents the results of the analysis of multiple tubes. Here, two tubes with perimeters of 200 mm each, three tubes with perimeters of 133 mm, and four tubes with perimeters of 100 mm each were subjected to dynamic load. The lengths of the tubes were kept at 350 mm. All the models had the same volume and contact surfaces. For the multiple tubes, the distance between the tubes varied to determine its effect on the results. Distances of r , $2r$, and $5r$ were considered between the adjacent tubes, where r is the radius of each tube. A total of nine simulations were conducted. The effect of distance for the two and three tubes was insignificant because until this point, the tubes were still deforming under progressive buckling mode. However, the deformation mode changed to global bending when four tubes with perimeters of 100 mm were simulated. To illustrate the effect of distance, two other models with four tubes and distances of 8 mm ($\approx r/2$) and 64 mm ($\approx 4r$) were simulated. The results are depicted in Figure 4.21 to compare the models in a frame-

by-frame manner. The model was stiff when the tubes were close to each other. This result was considerable by comparing the middle tubes in the two models in Figure 4.21. No contact existed between the tubes until the end of impact when the distance was 8 mm. However, global bending with contact between the tubes was clearly observed when the distance increased to 64 mm. This contact was observed at the initial stages of deformation (e.g., at time frame 25). Meanwhile, the distance between the tubes did not affect the numerical results when progressive deformation mode was observed on the two and three tubes. Therefore, decreasing the diameter of the tubes and increasing their number to keep the contact surface the same did not improve the crashworthiness of the models. The results are shown in Figures 4.18–4.20.

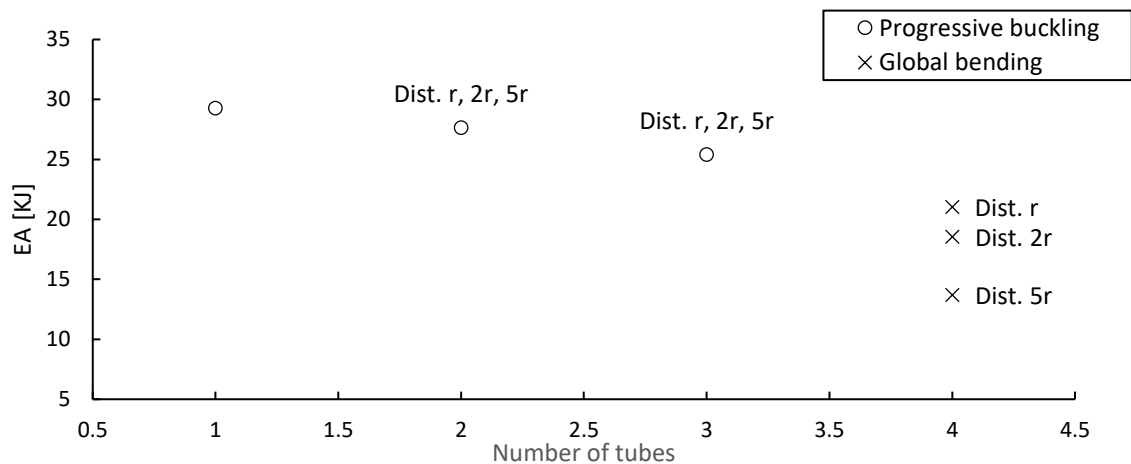


Figure 4.18: EA for multiple tubes with different distances of r , $2r$, and $5r$.

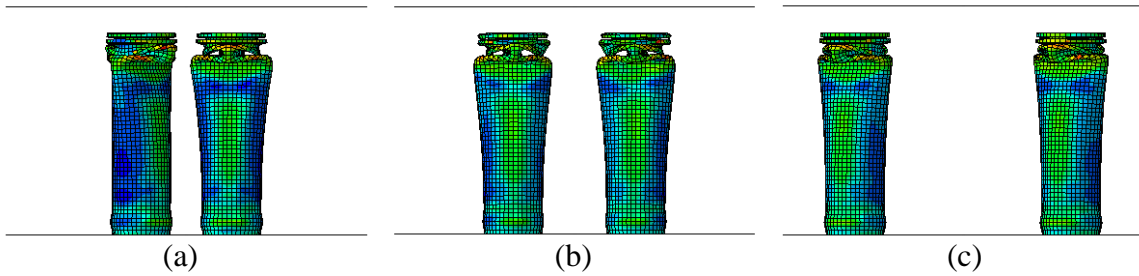


Figure 4.19: Deformation patterns of two tubes with different distances of (a) r , (b) $2r$, and (c) $5r$.

As shown in Figure 4.18, different amounts of energy were absorbed for different distances between the four tubes. This result was caused by the L/D ratio of the tubes, which led to the global bending deformation of the tubes rather than progressive buckling. However, similar EA characteristics were observed for the models with two and three tubes for the distances of r , $2r$, and $5r$. Less energy was absorbed when the number of tubes was increased. However, the CFE of the models increased. For the model with three tubes, the CFE increased to 55% compared with 46% in the case with one tube; however, this increase was more considerable for the model with two tubes where CFE reached 62%. The results are shown in Figure 4.20.

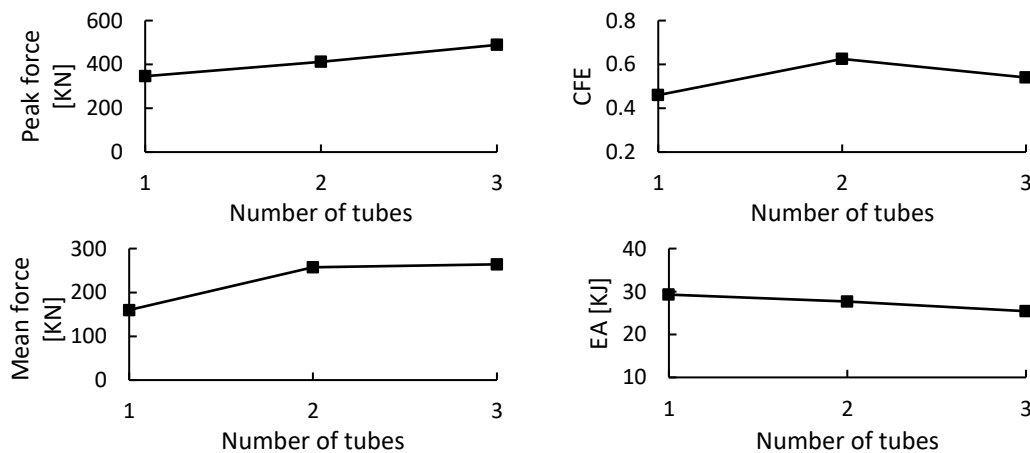


Figure 4.20: Effect of number of tubes on the crashworthiness of the base model.

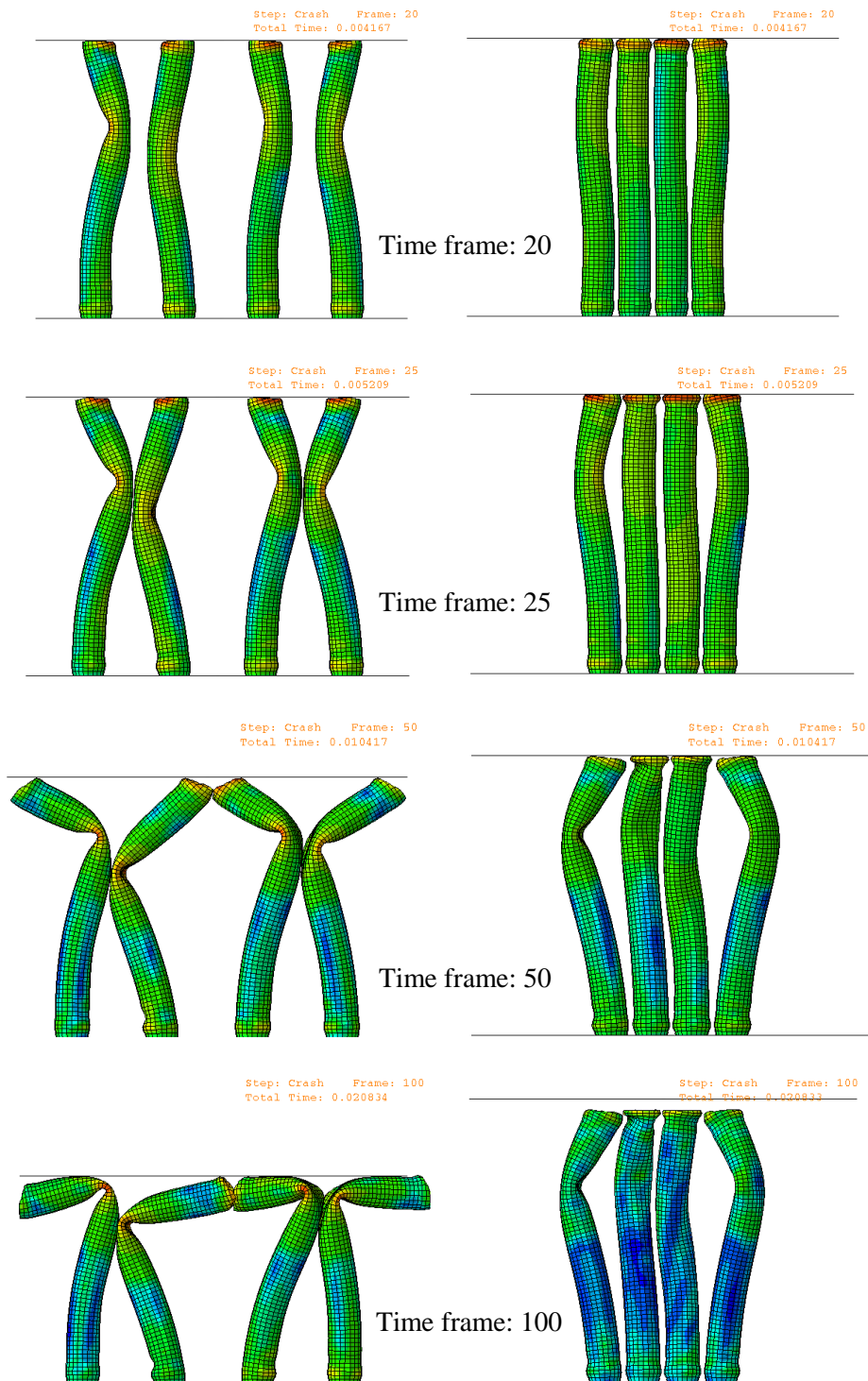


Figure 4.21: Deformation pattern of quadruple tubes with distances of $4r$ and $r/2$ at different time frames.

4.5.2 Corrugated samples

The numerical responses of corrugated tubes with different number of grooves and groove sizes are presented in this section. Three circular tubes with thicknesses of 1.5, 2, and 2.5 mm; perimeter of 400 mm; and length of 350 mm were used in these studies. Each tube was modeled with one to eight semicircular grooves with diameters of 1–10 mm. Figure 4.22.a shows the tube with eight 3 mm grooves. The code for this model is D3C8, where “D3” indicates 3 mm diameter, and “C3” indicates three corrugation geometries. Each model was sectioned, seeded, and meshed where grooves were formed by curves containing at least six edges, as shown in Figure 4.22.b.

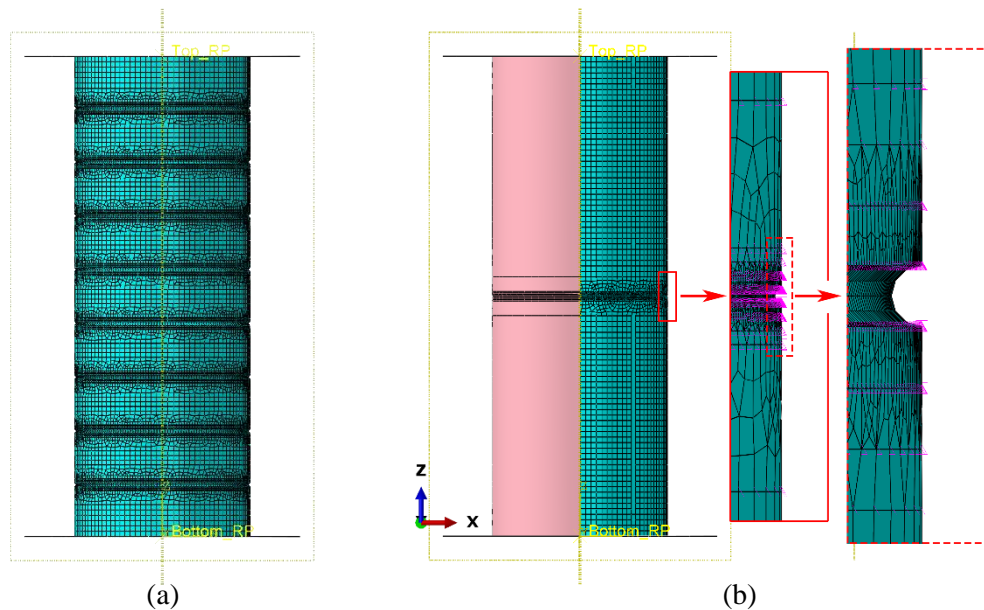


Figure 4.22: Corrugated tubes. (a) D3C8 model with 8 grooves of 3 mm; (b) meshing of grooves with sections.

The general mesh size between the grooves was set to 4 mm, as mentioned in previous sections. Seeding and section lines around the grooves led to a smooth and controlled transition from a fine mesh size (e.g., 0.3 mm) to 4 mm general mesh. The dimension

between the grooves was calculated by $d = (L - n \times D)/(n + 1)$, where L is the length of the tube, n is the number of grooves, and D is the diameter of the grooves.

The objective was to determine the EA of the models at different stages of deformation. On this basis, each f - d diagram was divided into three equal distances. A MATLAB code was used to measure the stroke of each simulation, and the matrix of f - d was divided into three parts for numerical integration. The area under each portion of the curve was considered the energy absorbed during the first, second, or last one-third of displacement (i.e., E_1 , E_2 , and E_3 , as shown in Figure 4.23). The simulation results are shown in Figure 4.24.

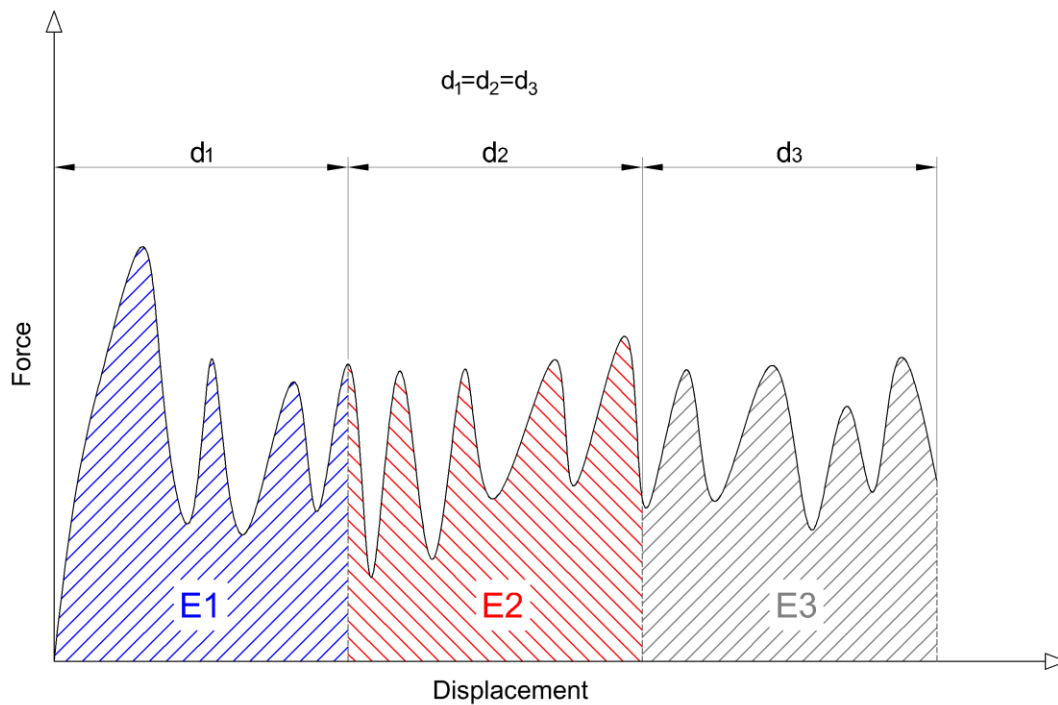


Figure 4.23: EA at different stages of deformation.

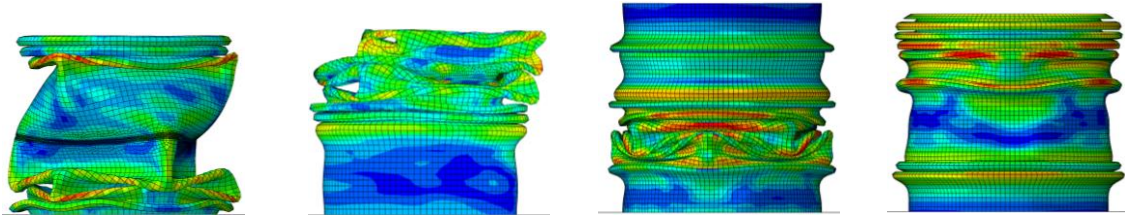


Figure 4.24: Deformation pattern of corrugated tubes. From left to right: D1C1, D2C2, D8C3, and D10C5.

The SEA of the tubes is shown in Figure 4.25 regarding E1, E2, and E3. From the figure, E1 (energy absorbed in the first one-third of the displacement) decreased and E3 (energy absorbed in the last one-third of the displacement) increased with the increase in the number and diameter of grooves. In other words, the models became soft, and the peak force traveled from beginning to the end of the f - d diagrams when they became sensitive to geometry. E2 (energy absorbed in the second one-third of the displacement) increased in most cases (C1–C4 models) and in some cases remained nearly constant (C5 models) or decreased (C8 models). C7 models provided a transition zone for E2 to begin to decrease. Specifically, E2 was nearly constant from D1C7 to D5C7 and began to decline from D7C7 to D10C7. Figure 4.26 illustrates the movement of the peak force in the f - d curve of C8 models from the beginning (D1C8) to the end (D10C8). Stroke increased during this transition, which indicated that the structure became soft; however, the mass of the tube increased with the diameter of the grooves.

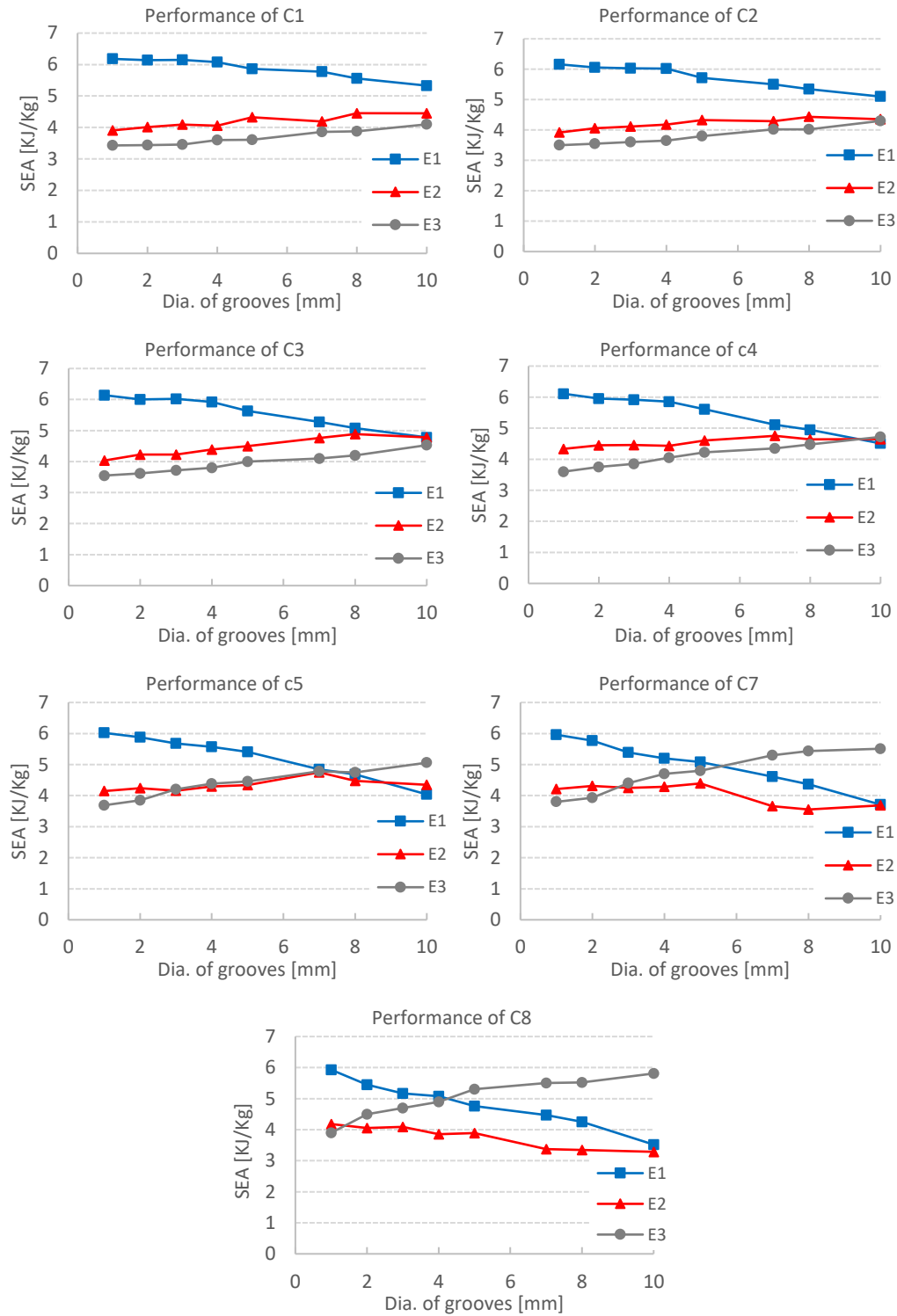


Figure 4.25: SEA of corrugated tubes.

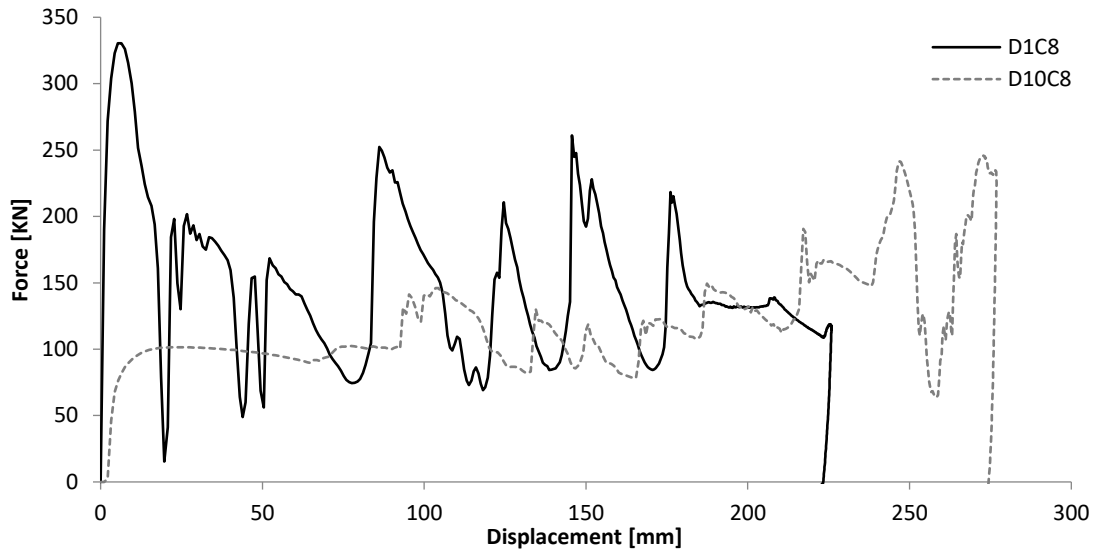


Figure 4.26: Transition of peak force to the end of the f–d diagram by increasing the diameter of the grooves (structural softening).

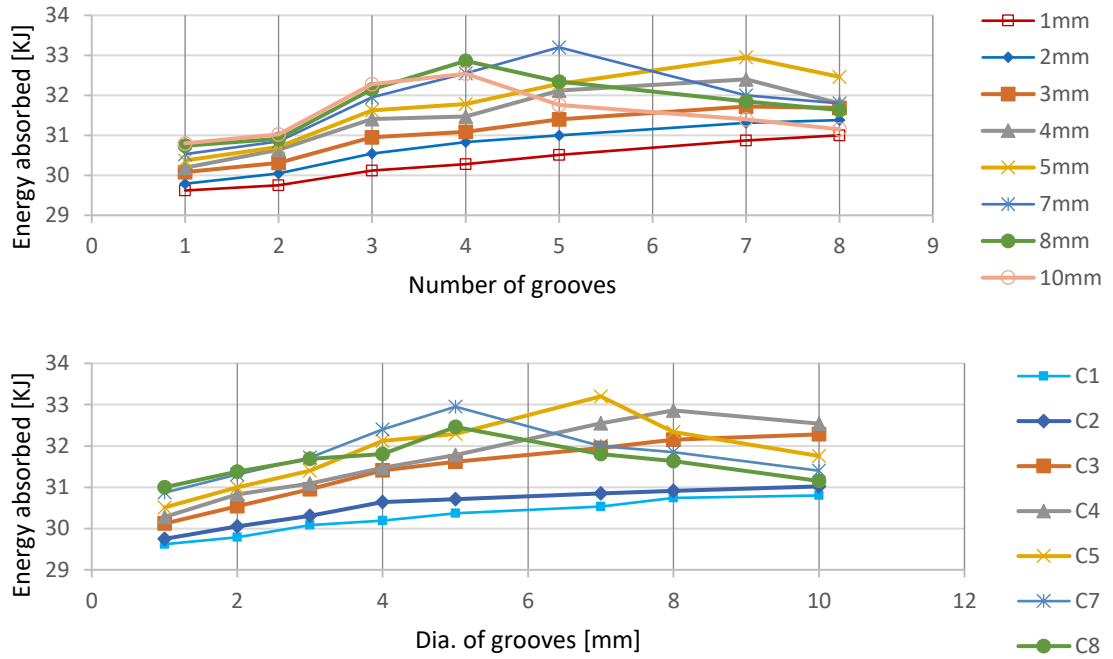


Figure 4.27: EA of corrugated tubes.

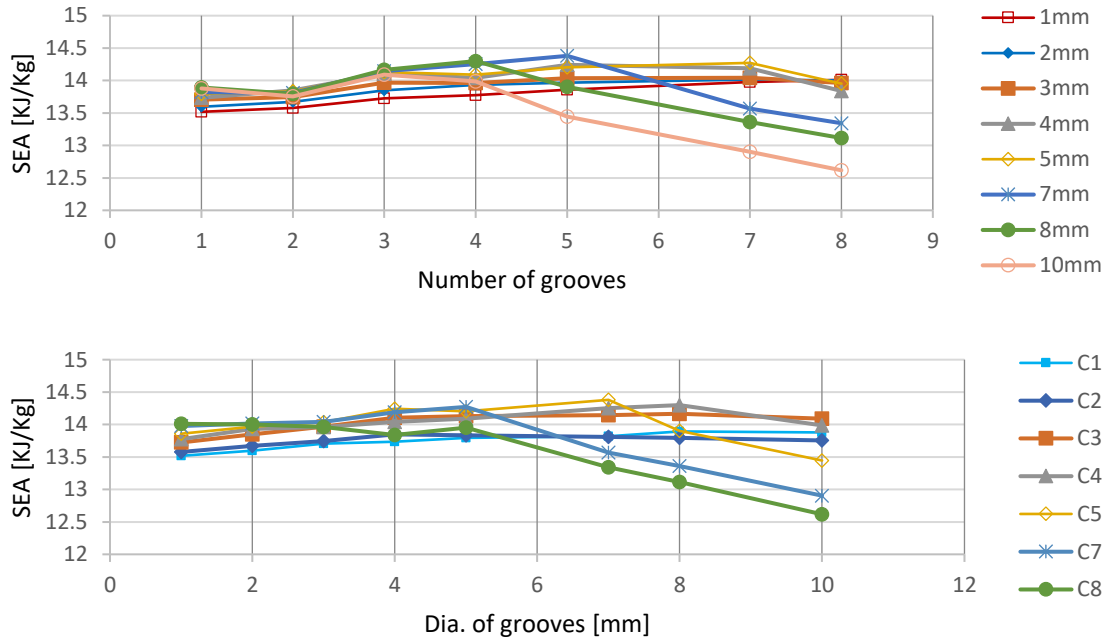
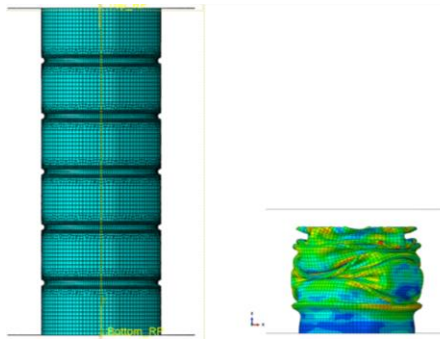
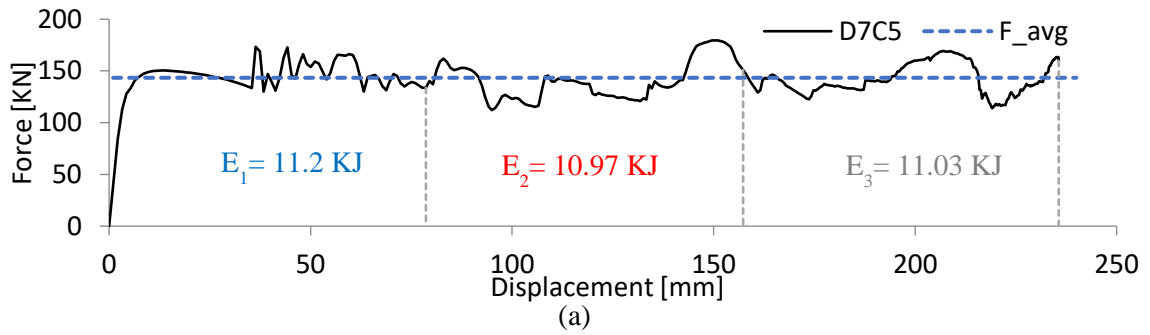


Figure 4.28: SEA of corrugated tubes.

Figure 4.27 shows the EA capacity of corrugated tubes. Although some materials were added to the tubes, EA began to decrease for some of the models when the diameter of the groove increased due to structural softening. This result led to considerable drop in the performance of heavy samples, as shown in Figure 4.28. The D7C5 model had the optimum EA characteristics. This model nearly had equal values of E1, E2, and E3, as shown in Figure 4.25 and an optimum CFE of 80%. The results are illustrated in Figure 4.29. The optimum point for each corrugated tube occurred when E1, E2, and E3 were almost equal or close to one another. This result was also observed on other corrugated samples. For example, C3 had the maximum value of EA at $D = 10$ mm, where E1, E2, and E3 were nearly equal. Figure 4.29 shows the f - d curve of the optimum corrugated tube (D7C5) and its deformation pattern.



(b)

Figure 4.29: Optimum corrugated tube of D7C5 model; (a) f-d diagram; (b) deformation pattern.

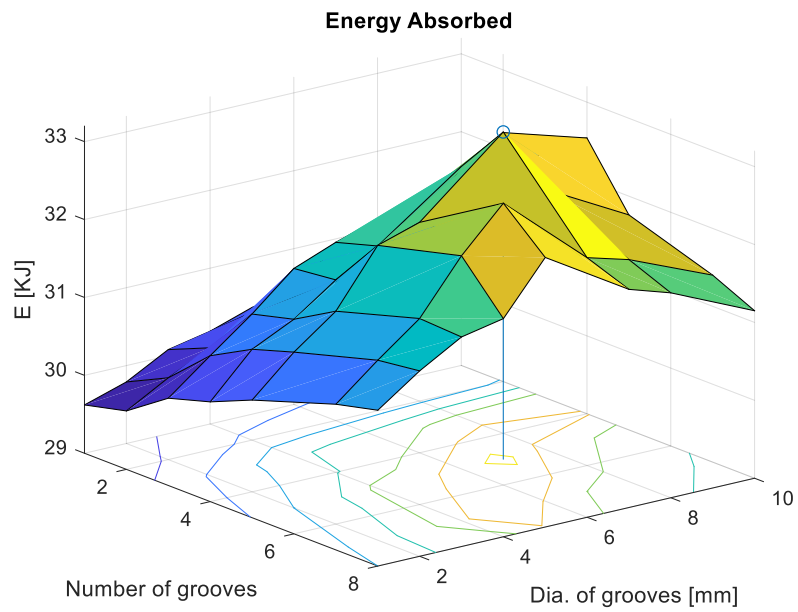


Figure 4.30: EA of tubes with different number of grooves and groove sizes.

It was observed that E1 was large for small grooves, and E3 was large for large grooves. E1 decreased and E3 increased by increasing the number of grooves. E2 remained constant for small grooves. E2 may increase or decrease for large grooves depending on the number of grooves. The optimum point for each corrugated tube existed when E1, E2, and E3 were nearly equal. A high EA value does not necessarily indicate a high CFE. However, a high CFE value is a good indicator that a high EA value can be gained. The opposite condition is also true, in which a favorable value of EA is not achieved when CFE is considerably low. The surface 3D plot of EA in terms of the number and diameter of grooves is shown in Figure 4.30.

Three tubes were modeled to determine the effect of the location of grooves on E1, E2, and E3, as shown in Figure 4.31. The location of grooves slightly affected the deformation modes. The value of stroke was the same for C3T and C3B models. The value of EA was the same, and no significant change was observed in the values of E1, E2, and E3. However, the results may differ with different sizes and number of grooves.

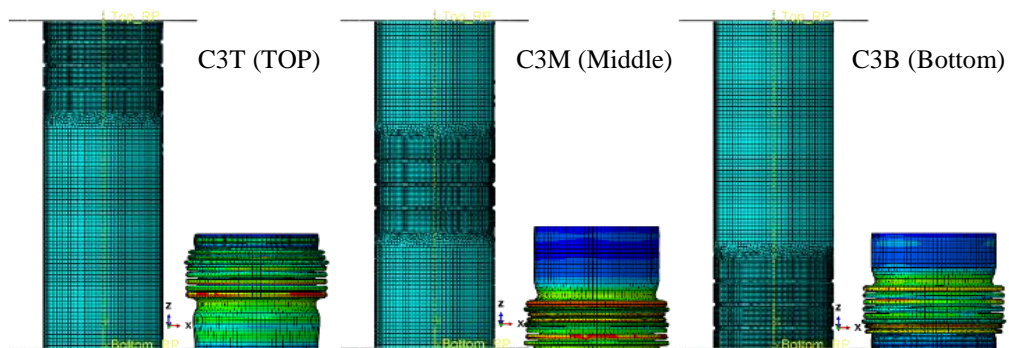


Figure 4.31: Effect of the location of grooves on the deformation of corrugated tubes.

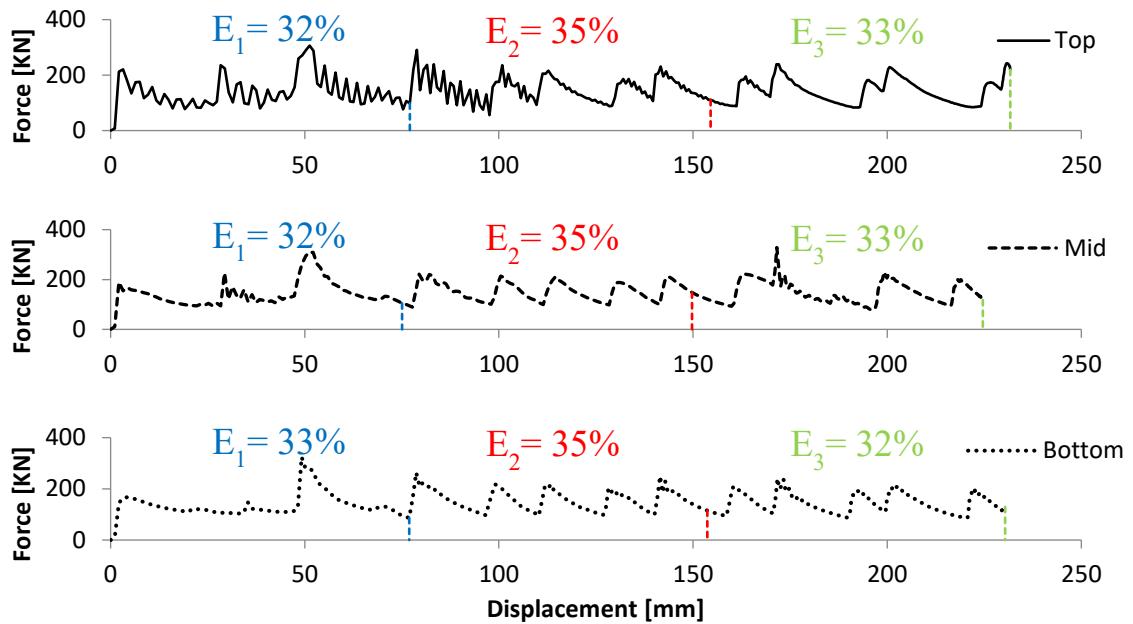


Figure 4.32: Effect of the location of grooves on E1, E2, and E3.

Similar simulations were performed with thicknesses of 1.5 mm and 2.5 mm on C5 models to determine the effect of wall thickness on the EA of corrugated tubes. The obtained EA values were quadratically interpolated using splines in MATLAB to produce a 3D plot with a smooth surface. The result is shown in Figure 4.33. The D4 model (with diameter of 4 mm) with wall thickness of 1.5 mm and the D10 model with $t = 2.5$ obtained the maximum EA values.

If this trend continues on both sides of the plot (i.e., for $t < 1.5$ mm and $t > 2.5$ mm), the optimum model could have large grooves as the wall thickness increases, and small grooves would be optimal with small wall thickness.

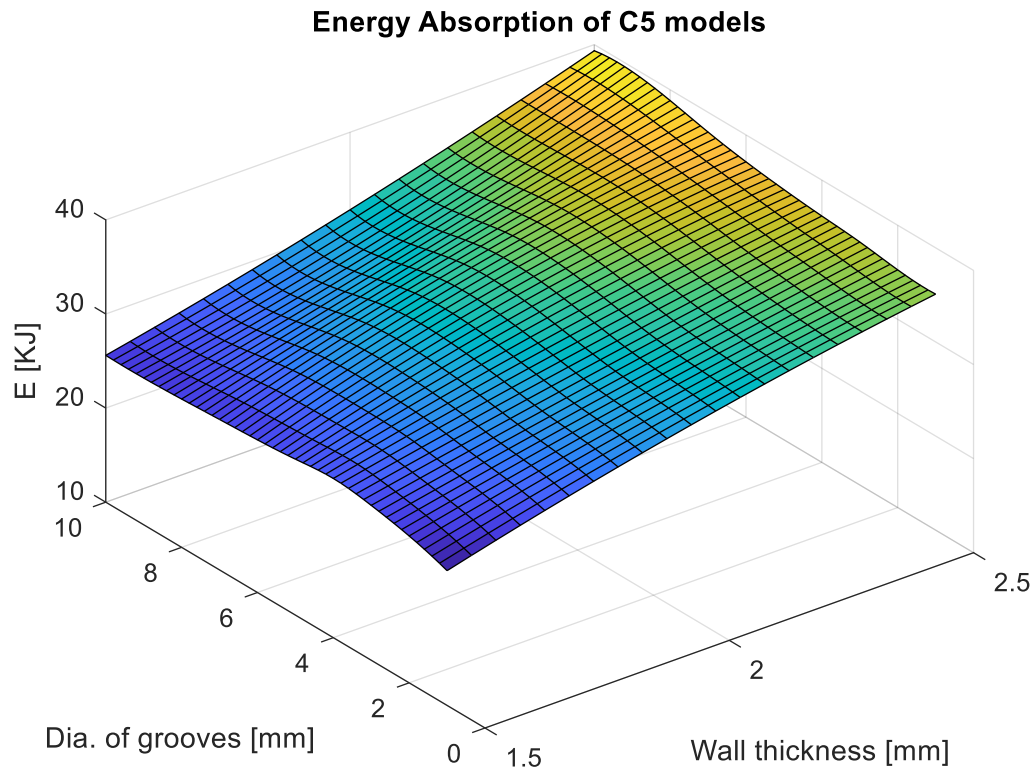


Figure 4.33: EA of C5 models as a function of wall thickness and diameter of grooves.

4.6 Conclusion

The effects of different parameters of material model and test conditions on the crashworthiness of circular tubes were investigated. Changing some of these parameters or combining them may result in an increase or decrease in energy-absorbing characteristics of the models.

Doubling the friction coefficient from 0.2 to 0.4 increased the EA of the tube by only 1%. However, the difference in the deformation mode was considerable. Initial impact velocity played an important role on the EA of the model. Increasing the initial velocity resulted in large CFE values but small EA values. As expected, increasing the working temperature

decreased the efficiency of the models. Therefore, an energy-absorbing device should be evaluated or simulated under real working temperature conditions.

Increasing the strain rate sensitivity parameter and the test speed resulted in small EA value. However, this condition was different for the strain hardening parameter. Large values of this parameter resulted in considerable EA capacity and large CFE value. An optimum point was observed on strain hardening in which the model had the best energy efficiency.

Corrugated tubes were analyzed, and an optimum model was observed regarding the number and size of grooves that resulted in large values of CFE and considerable EA. This model had nearly equal values of EA at different stages of stroke (i.e., E1, E2, and E3 in the first, middle, and last portions of deformation, respectively). Moreover, the optimum model changed under various wall thicknesses.

In conclusion, different materials or test parameters could result in improved EA of the model. However, an optimum point or value should be obtained for some of these parameters, such as shape and wall thickness. EA efficiency or enhancement (SEA or EA) is not constantly achieved with high CFE values.

Chapter 5 Effects of composite materials on the response of rings and thin-walled tubes

5.1 Introduction

Cladding or lamination is a technique in which the layers of different materials are bonded together to enhance the characteristics of the base material. The improvement can be in different shapes depending on the application of the components in different industries. Increased ductility, durability, corrosion/wear resistance, and heat or sound isolation are some of the advantages of cladding. This technique has been widely investigated by researchers and engineers from different fields in the past a few decades. Chen et al. [2010] numerically investigated the effect of cladding a ductile layer on the necking behavior in sheet metals under tension. They showed that adding a ductile layer to the base material increased necking and fracture strains. They also illustrated that the fracture behavior of the models was sensitive to the mesh size. Shi et al. [2014] developed an FE model of laminated tubes subjected to dynamic axial loading to determine the effect of rate sensitivity on necking behavior. They used a rate-dependent material for the cladding layer on a rate-independent core material. The necking behaviors of the laminated materials were directly related to the volume fraction of the cladding layer and loading speed.

In this chapter, the effect of adding a ductile layer on f - d diagram and deformation of compressed rings, and EA and deformation of thin-wall circular tubes is investigated. The materials used here were in accordance with the work of Chen et al. [2010].

The base and clad materials used a power law model, which is expressed as follows:

$$\bar{\varepsilon} = \begin{cases} \frac{\bar{\sigma}}{E} & \text{for } \bar{\sigma} \leq \sigma_y \\ \frac{\sigma_y}{E} \left(\frac{\bar{\sigma}}{\sigma_y} \right)^n & \text{for } \bar{\sigma} > \sigma_y \end{cases} \quad (5.1)$$

where σ_y is the yield stress, and n is the strain hardening exponent. The base material had high yield stress and low strain hardening rate ($\sigma_y = 243$ MPa, and $n = 10$). The clad material was soft and had a low yield stress with high strain hardening rate ($\sigma_y = 142$ MPa, and $n = 5$), as shown in Figure 5.1.

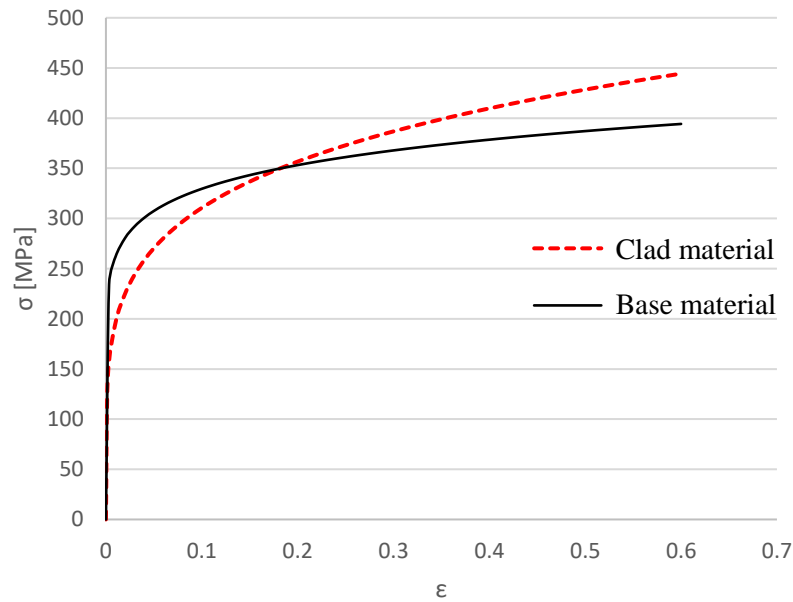


Figure 5.1: Stress–strain curve of the base and cladding materials.

5.2 Effect of ductile layer on the f-d curve of compressed rings

A ring with geometric ratio of 6:3:2, OD of 15 mm, and base material model was modeled in ABAQUS, as shown in Figure 5.1. The ring was subjected to a static load and was compressed for 30% of its height. The result is illustrated in Figure 5.2.a. As shown in

Figure 3.24.a, the plastic strain is localized and connects the four corners of the cross section and the middle of the inner surface.

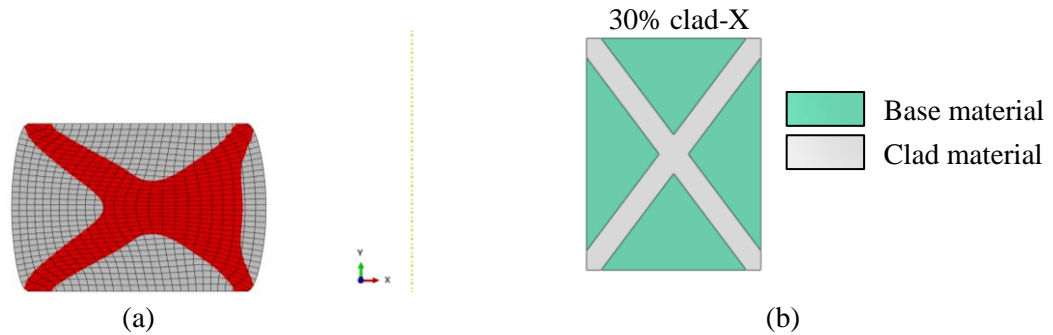


Figure 5.2: (a) Plastic strain localization in 6:3:2 ring with the base material; (b) cross-section of the ring with base material and x-shape section with ductile material.

The ductile material was assigned to an x-shaped area in the cross section of the ring. The width of this section was 0.5 mm. The total area of this section was nearly one-third of the entire area of the cross section. This region covered the localization of plastic strain. Figure 5.3 compares the f–d diagram of the compressed rings with and without the clad material.

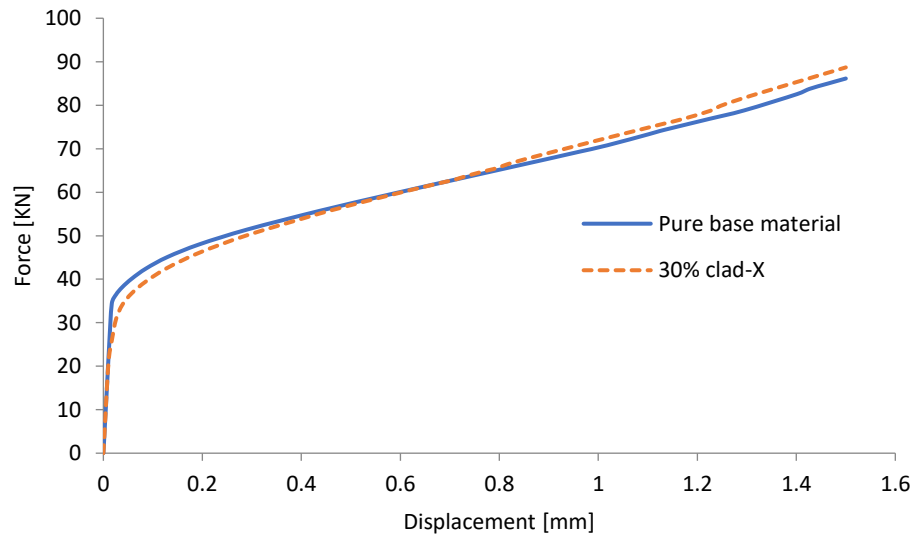


Figure 5.3: F–d diagram of ring with pure base material and mixed with clad material.

At the beginning of compression, the f–d curve of the X-sectioned model was located below the one with the base material. After approximately 0.6 mm of compression (12%), more load was required to compress this ring compared to the pure base model. At the end of compression, the maximum force of the X-sectioned ring was approximately 3% more than the maximum force of the model with the base material. This behavior was also observed in the stress–strain curve of the two materials, as shown in Figure 5.1, indicating the participation of the ductile material in the model. The energy required for 30% compression of the model with ductile material was approximately 1% more than the base model.

The friction coefficient was 0.2 in the two simulations. The friction coefficient was set to zero to determine its effect. As shown in Figure 5.4, the overall behavior was similar, and the values of force decreased as expected. The f–d curve of the X-sectioned model was lower until 16% of compression, and the values of the maximum force were different by 2%.

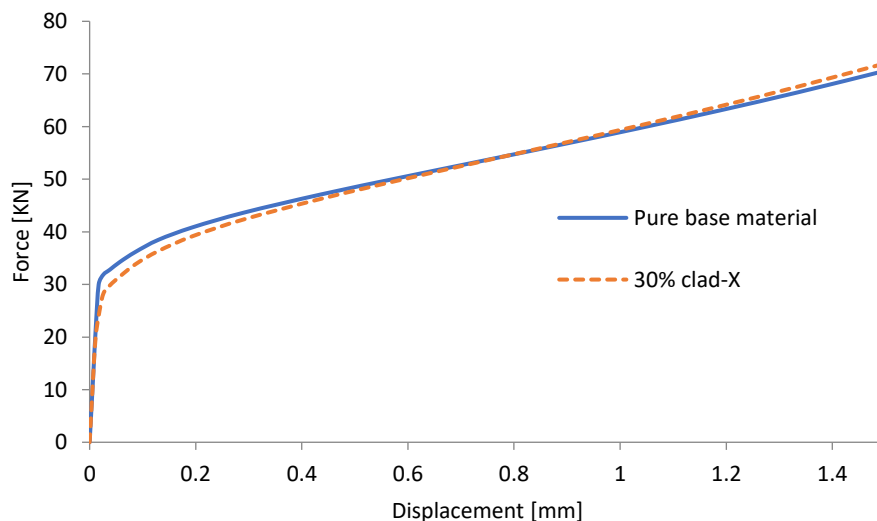


Figure 5.4: F–d diagram of rings without friction between the contact surfaces.

Three other models with different cross sections but similar volume fraction of clad material were constructed, as shown in Figure 5.5. The comparison of f–d curves is shown in Figure 5.6. The X-model was softer than the two other models, and the ring with the vertical layer of clad and base material was the hardest model. However, the difference was small and could be ignored.

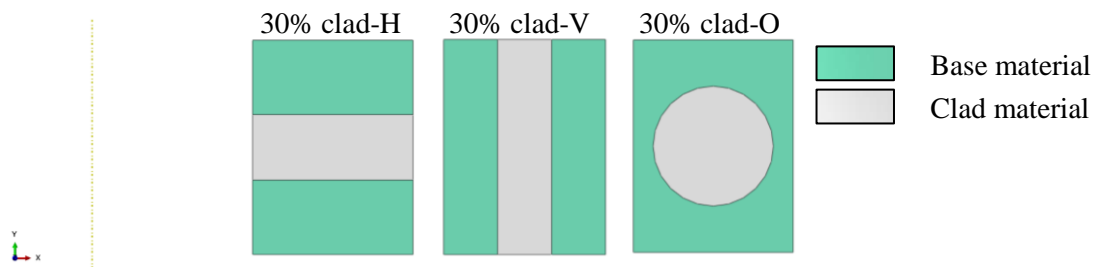


Figure 5.5: Cross section of rings with 30% of clad material.

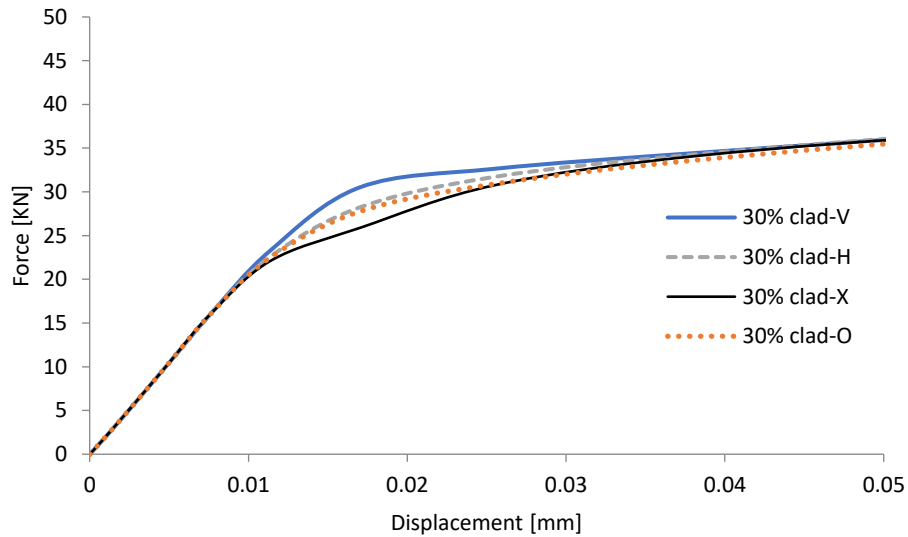


Figure 5.6: Effect of the location of clad material on f–d diagrams.

Two other models with 30% cladding layer on the inner and outer surfaces were constructed, as shown in Figure 5.7. The effect of this layer on radial and tangential stress distributions is shown in Figure 5.8.

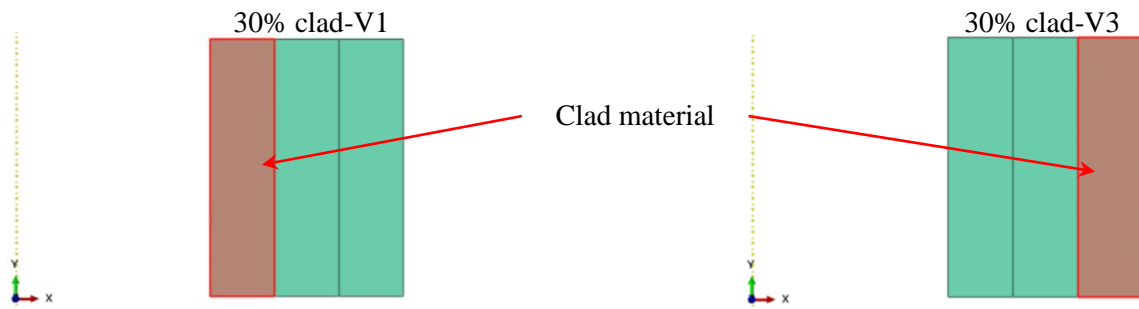


Figure 5.7: Cladding layer on the inner and outer surfaces.

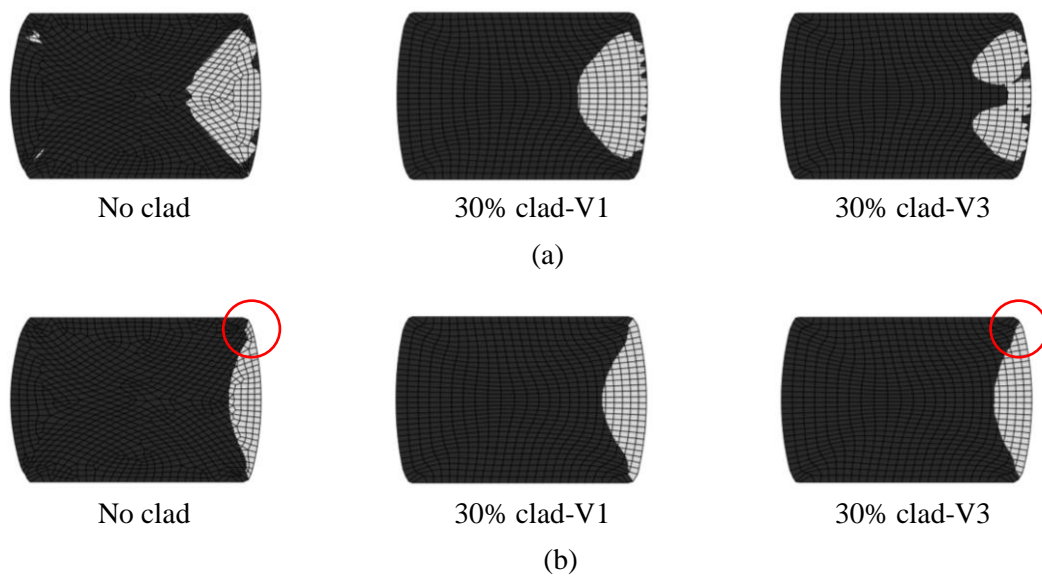


Figure 5.8: (a) Radial stress distribution; (b) tangential stress distribution; compressive stress in dark grey and tensile stress in white.

The tensile radial stress at the corners of the inner wall disappeared with the presence of the cladding layer regardless of its location. Less tensile radial stress was formed in the cross section in both cases. This condition was more considerable when the outer wall was cladded. The distribution pattern for the tangential stress was different. More tensile tangential stress was formed at the outer wall in both cases, whereas less tensile tangential stress was formed in the cladded outer surface. The corners of the outer wall experienced less tangential tensile stress in the V3 model compared with the base model. These regions

are indicated by the red circles in Figure 5.8.b. Therefore, cladding the outer wall could delay fractures because cracks initiate from the corners of the outer wall.

5.3 Effect of cladding on EA

5.3.1 Simple circular tubes

A series of simulations was conducted on tubes with perimeters of 400 mm and different thicknesses and lengths to select the suitable dimensions for the base model. A length of 450 mm provided a good deformation pattern for the base model with 100% base material. A thickness of 2.5 was selected to enable each layer to stack 0.25 mm (or 10% of the entire thickness). Figure 5.9 shows the deformation and f–d curve of this model.

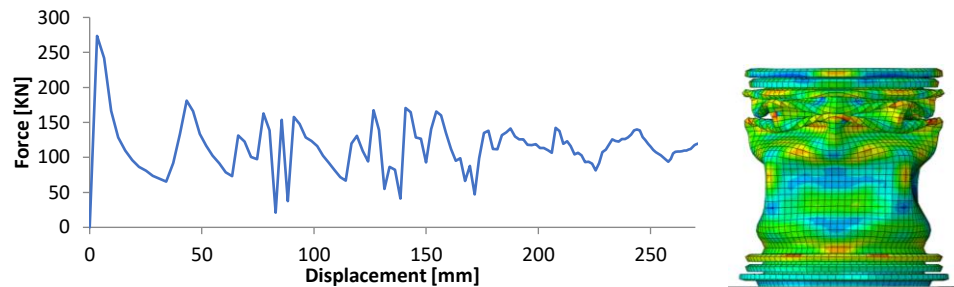


Figure 5.9: Results of simulation of the model with pure base material.

Volume fraction of cladding material was defined as the ratio of thickness of the cladding layer to the total wall thickness, as shown in Figure 5.10.

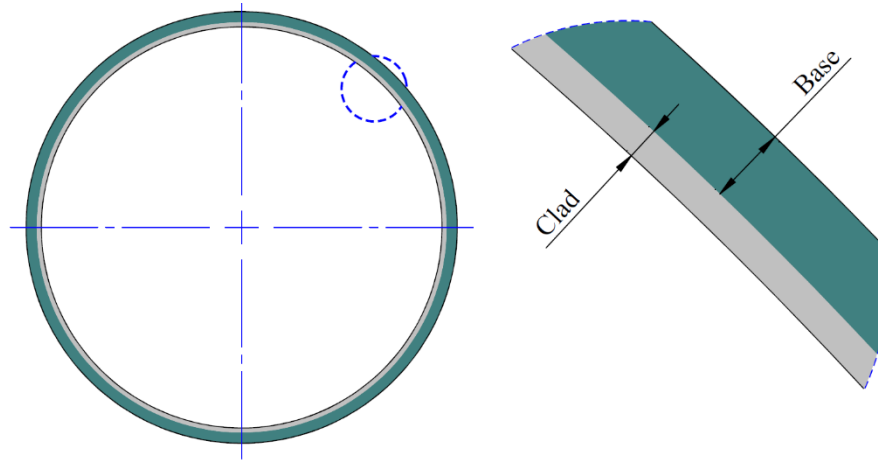


Figure 5.10: Sketch of the laminated composite system (top view).

The clad material was defined in ABAQUS through the continuum shell section as a composite layer. The orientation angle was set to zero for all the layers, and each layer had three integration points through the wall thickness. Different thicknesses of clad material were given to the composite layers to define the cladding percentage. The results are presented in Table 5.1.

Table 5.1. Effect of cladding layer on EA and CFE.

Model	Crush Length [mm]	Stroke Efficiency [%]	Peak Force [KN]	Mean Force [KN]	CFE	EA [KJ]
Pure base (0% clad)	289.09	64.2	273.58	114.34	0.42	29.82
10% clad	314.15	69.8	256.56	105.21	0.41	30.54
25% clad	292.38	65.0	256.10	109.28	0.43	31.02
50% clad	290.21	64.5	240.07	105.35	0.44	29.83
75% clad	333.82	74.2	223.97	99.76	0.45	29.43
90% clad	316.56	70.3	212.01	102.51	0.48	28.86
Pure clad	296.72	65.9	213.76	106.71	0.50	28.71

As shown in Figure 5.11, 25% cladding on the base layer provided the maximum EA. The peak force decreased with the increase of the contribution of the soft cladding layer. However, the variation of mean force was small. The peak force decreased by approximately 22% from the pure base material to the pure clad material. The difference between the lowest to the highest value of mean force was 12%. This trend resulted in high CFE values with the increase in the percentage of cladding layer.

Here, a high CFE value does not necessarily result in a high EA value. An optimum ratio of cladding to base thickness existed in which the highest EA value was obtained. The CFE of pure clad material was the highest in this particular model and geometry. However, this point had the lowest EA value. The model with 25% of clad material had a moderate CFE value and the highest EA value.

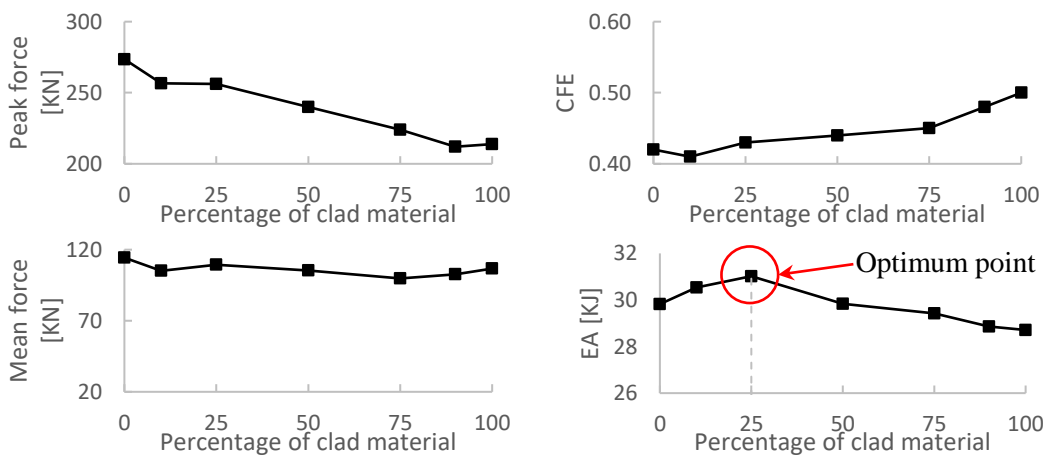


Figure 5.11: Effect of cladding layer on the crashworthiness of the base model.

The simulation results of the optimum model are shown in Figure 5.12. From the figure, the fluctuation moved from the middle to the beginning of the f - d curve when the thickness of the clad material was increased. This result led to approximately 4% more EA and 6%

more stroke efficiency. These values would be different for different models; nevertheless, an optimum point could be achieved.

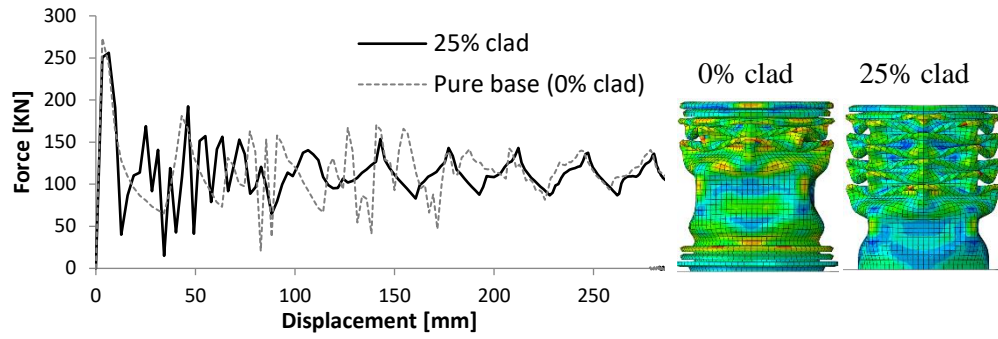


Figure 5.12: Effect of cladding layer on the crashworthiness of the base model.

Circular tubes are cladded to enhance the corrosion or wear resistance of the base material. In such cases, the inner surface that is in contact with other substances is laminated. On this basis, the cladding layer started to grow from the inner radius in the previous section. Here, another model with 25% cladding layer on the outer surface was constructed. Figure 5.13 shows the results of 25% cladding on the inner and outer surfaces.

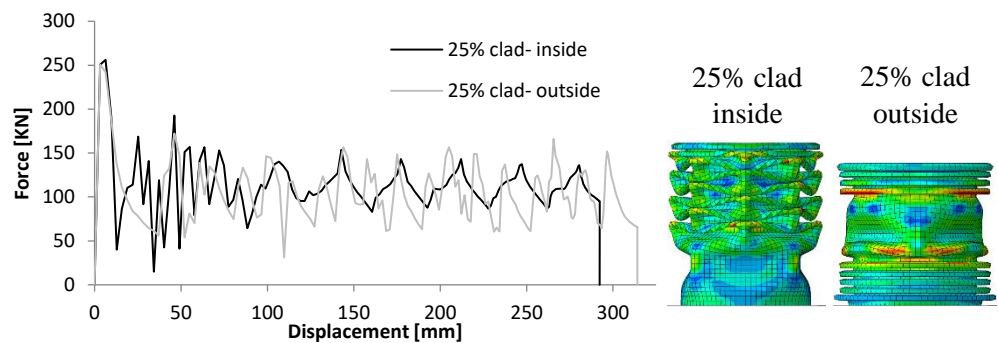


Figure 5.13: Inner surface cladding versus outer surface cladding.

The crush length increased from 292 mm to 314 mm, and the stroke efficiency increased by approximately 5%. The deformation pattern completely changed. One concertina and eight diamond modes were observed in the case of inner surface cladding. One diamond and nine concertina modes were observed when the outer surface was laminated with ductile material. Although the stroke efficiency increased, the EA and CFE values decreased by approximately 0.5% and 4%, respectively. The cladding area through the cross section increased by 3% (from 246 mm² to 254 mm²) when 25% of wall thickness was laminated from the outside. This condition resulted in more contribution of the ductile material to the total mass. Therefore, cladding the inner surface led to better EA characteristics in this model.

5.3.2 Supported circular tubes

A series of simulations was conducted on circular tubes supported by spiral blades. The tubes had 2.5 mm wall thickness, 63.7 mm radius, and 450 mm height. The blades had 0.5 mm thickness, 15 mm and 20 mm widths (*w*), and 45–900 mm pitch (*P*), as shown in Figure 5.14.a. The spiral blades had 1/2–10 revolutions (with increments of half-turn) around the tubes. Symmetry was kept through the cross section of the tube at different heights to avoid global bending. On this basis, the same support with 180° difference in the starting point was modeled on the other side of the tube. The base material model shown in Figure 5.1 was assigned to the tubes, and the tubes were subjected to dynamic loading. Figure 5.14.b shows the results of some of the simulations. The w20t8 model had a blade width (*BW*) of 20 mm and number of rotations (*NORs*) of 8.

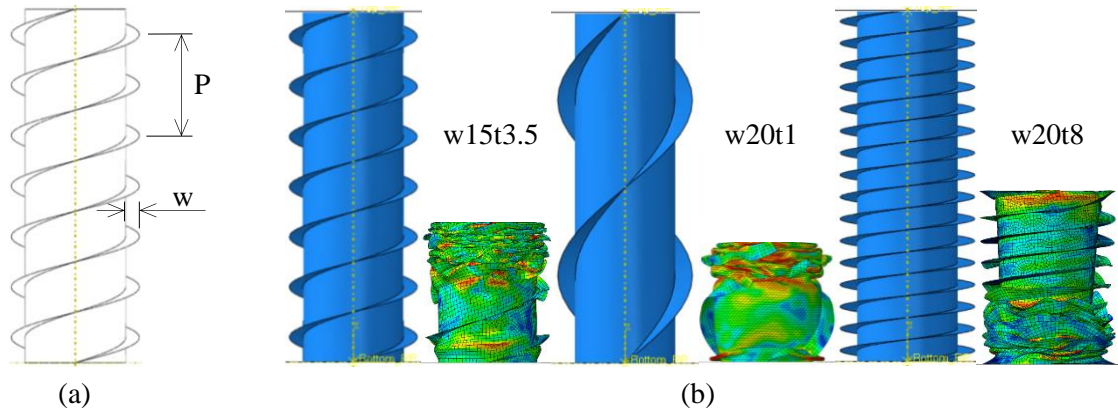


Figure 5.14: (a) Circular tubes supported by spiral blades; (b) deformation pattern.

The samples became heavier with the increase in the number of turns and width of spiral blades. The EA per unit mass of the tubes was plotted to compare their performance, as shown in Figure 5.15. The w15t4 model had the best performance among the samples.

The w15t4 model absorbed approximately 31.93 kJ of energy after the impact. This value was approximately 7% more than the EA of the simple tube (without spiral supports). However, the mass of this sample was approximately 7% more than the simple tube. Therefore, the SEA remained the same. SEA rapidly decreased for heavy tubes after the optimum point because the EA value remained nearly the same. Considerable deformation was observed at the bottom of the tubes with the increase of NORs, as shown in the right image in Figure 5.14.b.

Another simulation was performed on the w15t4 model to determine the effects of supporting blades on the EA of the simple tubes. Here, the material of the tube was kept as the base material; however, the material of the blade was changed to the clad material, as shown in Figure 5.1. The result is shown in Figure 5.16.a.

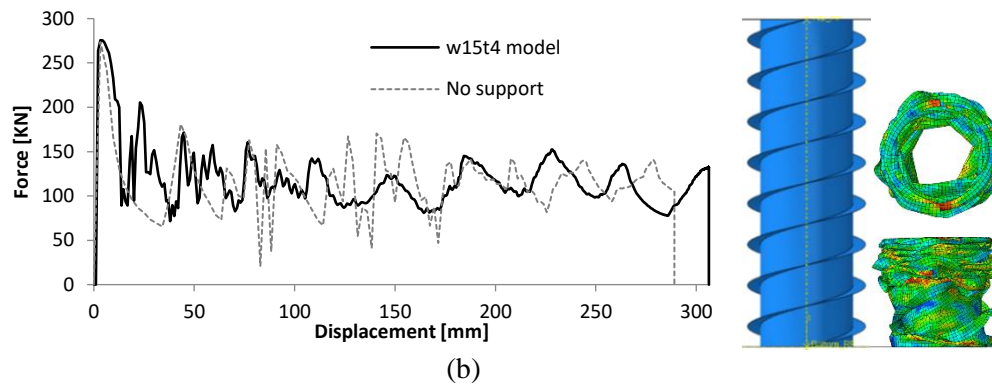
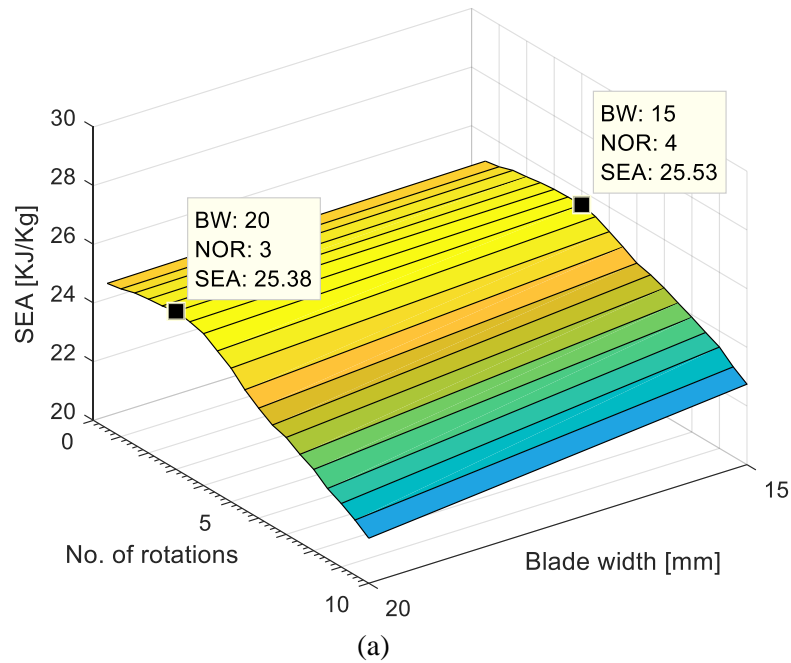


Figure 5.15: (a) Performance of supported tubes; (b) f–d curve and deformation of w15t4.

The total EA remained the same, which could be attributed to the fact that the volume fraction of the blade was less than 6% of the total volume of the model. The total area of the blades was approximately 30% of the area of the thin-walled tube ($54,000 \text{ mm}^2$ compared with $180,000 \text{ mm}^2$). The deformation pattern became slightly different. The f–d curve of the two models were the same up to 50% of the total deformation (153 mm). The

curves were different after this point. The bottom of the model with the soft blade began to fold from 65% of the total displacement, as shown in Figure 5.16.b. The model with the hard blade did not fold from the bottom until 88% of displacement, as shown in Figure 5.16.c. The total stroke of both models was approximately 306 mm, as shown in Figure 5.16.d. The hard blades (modeled by the base material) were good supports for this geometry on the basis of the f–d diagram.

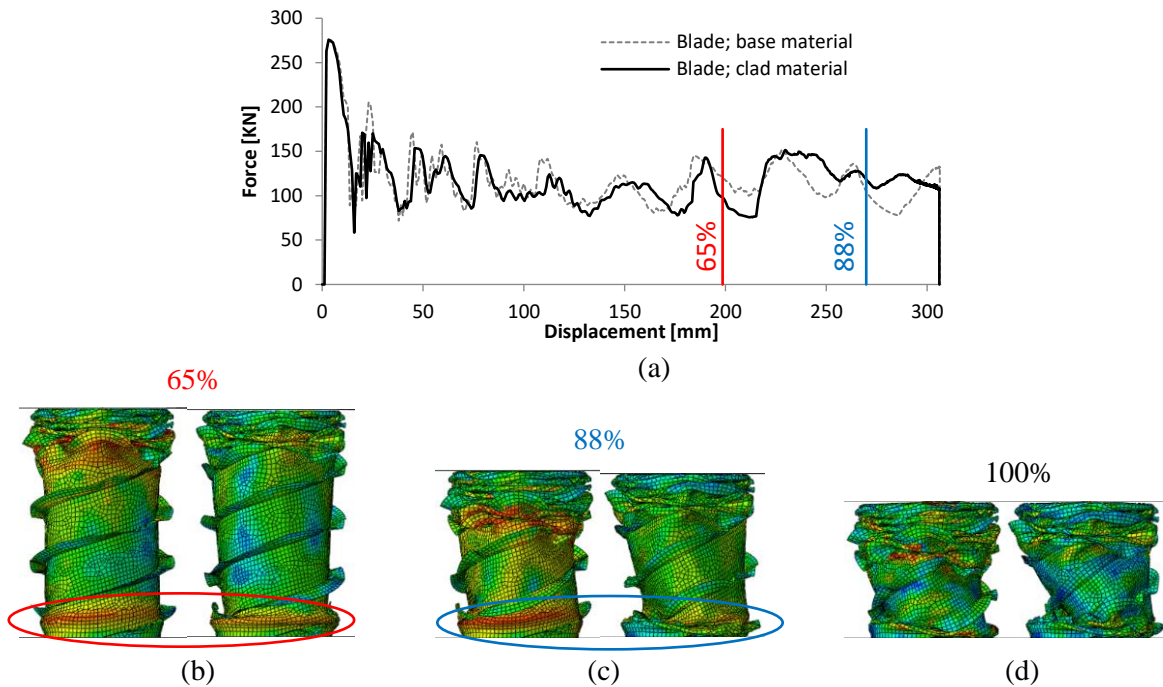


Figure 5.16: (a) F–d curve of the w15t4 model with different blade materials; (b)–(d) deformation at 65%, 88%, and 100% of displacement, respectively.

5.3.3 Circular tubes with oriented ductile layers

The base circular model with perimeter of 400 mm, height of 450 mm, and wall thickness of 2.5 mm was used in this section. The tube had a base material model with different layers of clad material. The layers of the clad material were oriented in different directions, as shown in Figure 5.17. As stated in Section 5.3.1, 25% of clad material is the best selection

for this tube. This ratio was used here for the volume fraction of clad to the base material. Three different directions of 0° , 45° , and 90° were used for the rotation of the clad layers. Another model was constructed on the basis of the spiral path of the w15t4 model from the previous section. This model is shown in the right image in Figure 5.17. The width of the clad layers was kept constant in the models. Figure 5.18 shows the deformation of the four models under axial dynamic loading. The deformation pattern of the L45 model (layers at 45° angle) was similar to the one with 25% clad at the inner surface (as discussed in Section 5.3.1).

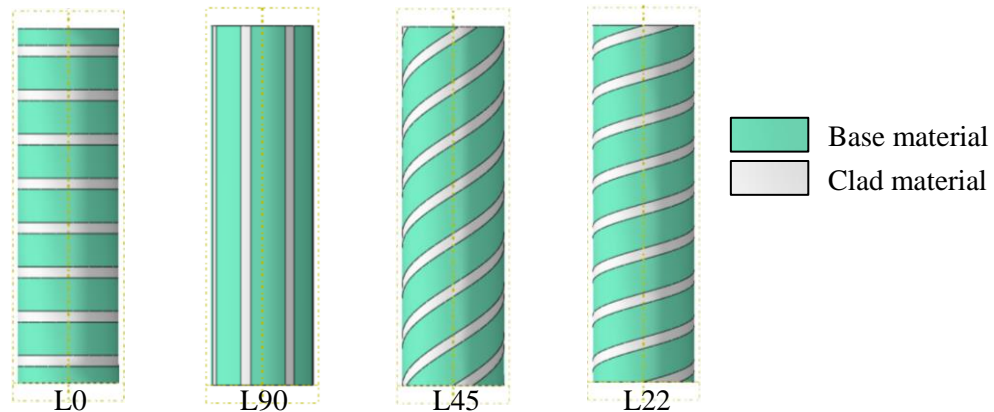


Figure 5.17: Circular tubes with 75% base material and 25% clad material along different directions.

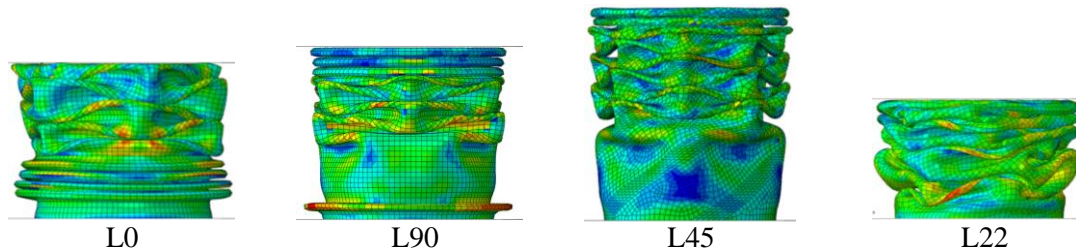


Figure 5.18: Deformation of circular tubes with 25% clad material.

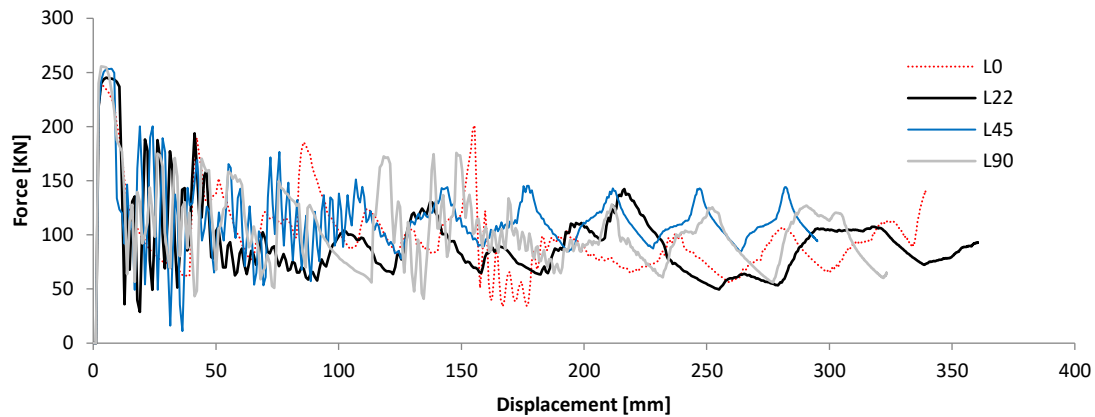


Figure 5.19: F–d diagram of circular tubes with 25% clad material at different angles.

Table 5.2. Effect of 25% cladding with different orientation of layers on EA and CFE.

Model	Crush Length [mm]	Stroke Efficiency [%]	Peak Force [kN]	Mean Force [kN]	CFE	Energy Absorbed [kJ]
Pure base (0% clad)	289.09	64.2	273.58	114.34	0.42	29.82
25% clad (inner surface)	292.38	65.0	256.10	109.28	0.43	31.02
25%-L0	339.28	75.4	239.16	98.10	0.41	31.33
25%-L22	360.60	80.1	245.28	96.89	0.39	31.35
25%-L45	295.09	65.6	253.46	110.36	0.44	32.07
25%-L90	322.98	71.8	255.65	97.52	0.38	31.74

The L45 model provided the highest EA value. The efficiency of this model was approximately 8% more than the model with pure base material. The CFE of this model was higher than the other models. L0 and L22 models with more than 75% of stroke efficiency were softer than L45 and L90 models. L22 and L90 models had the least CFE values because one of them was relatively soft and had a low value of mean force, whereas the other was relatively hard and had a high value of peak force. Considering that the layers

of the model with the highest EA (L45) were at 45° angle, adding horizontal and vertical layers of soft material or their combination could increase the performance of energy absorbers.

5.4 Conclusion

In this chapter, the effect of cladding a ductile layer on f–d diagram, the deformation of compressed rings, and the EA and deformation of thin-wall circular tubes were investigated. The base material had high yield stress and low strain hardening rate, whereas the clad material was soft and had a low yield stress with high strain hardening rate.

In the first part of this chapter, the clad material was assigned to the diagonal of the cross section of a 6:3:2 ring subjected to static axial loading. In the beginning and up to 12% of compression, the f–d curve of the X-sectioned model was located below the one with only the base material. At the end of compression, the maximum force of the X-sectioned ring was more than the maximum force of the model with the base material. Approximately 1% more energy was required to compress the X-sectioned ring at 30% compression compared with the base model. The geometry of the ductile section did not considerably affect the f–d curves of the models. The overall behavior remained the same for different friction coefficients.

The clad material was assigned to the inner and outer walls of the rings. The tensile radial stress at the corners of the inner wall disappeared with the presence of the cladding layer regardless of its location. The corners of the outer wall experienced less tangential tensile

stress in the model with cladded outer wall compared with the base model. Cladding the outer wall of the ring with a soft material could delay the crack initiation.

In the second part of this chapter, the effect of cladding on the EA of circular tubes was investigated. Tubes with layers of clad material on their inner surface were subjected to dynamic axial loading. An optimum value existed for the volume fraction of the clad material in which the highest performance of the energy absorber could be achieved. The results were different when the outer surface was cladded. The EA value reduced by approximately 1%, the CFE value decreased by approximately 4%, and the deformation pattern completely changed compared with the cladded inner wall.

In the last part of this chapter, circular tubes with layers of clad material oriented at different angles were subjected to dynamic axial loading. The model with layers at 45° angle showed the best performance and had the highest values of EA and CFE. After this model, the one with vertical stripes of clad material absorbed the most energy. Cladding a ductile material could improve the performance of energy absorbers.

Chapter 6 Conclusions

In the ring compression test, the calibration curves remain constant under different geometries with the same geometric ratio and shape factor when no friction exists between the contact surfaces. When friction exists, the calibration curves of the large rings with the same geometric ratio and shape factor are located lower on the diagram. The above conclusion is unsuitable for the rings with the same shape factor but different geometric ratios. The calibration curves of the rings with different geometric ratios can be located lower or higher on the diagram regardless of the ring size.

The calibration curves become closer together on the diagram with the increase of friction coefficient. The outer wall constantly moves outward. The friction coefficient has a certain value in which the inner wall moves outward at the beginning until a certain compression rate and then moves inward. This condition should be considered when the direction of material flow is not physically controlled during formation.

The application of hydrostatic pressure on the inner and outer walls of the ring can improve compressibility. Hydrostatic pressure changes the stress distribution at the cross section of the ring. The tensile tangential and radial stresses can be minimized with the presence of hydraulic pressure. The radial stress can be easily changed from tensile to compressive compared with the tangential stress.

Different parameters of material model and test conditions play important roles on the crashworthiness of energy-absorbing devices. The use of less strain rate sensitive materials results in high EA. An optimum value exists for strain hardening parameter in which the

model has the best efficiency. Otherwise, large values of this parameter could result in considerable EA capacity and large CFE.

High SEA values are not constantly obtained with high values of CFE. Stroke efficiency alone is ineffective for evaluating the crashworthiness of structures. However, the structure with higher stroke efficiency is more favorable when the SEA and CFE values are the same for two different structures.

The f - d diagram of energy absorbers can be divided into different parts. The model can have the best performance when the area is the same under the curve of each part. If the peak force is located in the first part of the diagram, then it can be controlled, moved, or even omitted in the presence of slots or triggers in the model. The size and shape of these triggers should be optimized. The model with regular fluctuations and without any peak force is the optimum.

The addition of layers of a ductile material to the base model can improve compressibility and crashworthiness. The volume fraction of the clad material and its location should be optimized. In the ring compression test, compressibility can be high when the outer wall is clad. For circular tubes as energy absorbers, the addition of some layers at 45° angle can increase EA and CFE.

Bibliography

- ABAQUS Analysis User's Manual, Version 6.14, 2014. Dassault Systèmes Simulia Corp., Providence.
- Abramowicz, W., & Jones, N. (1986). Dynamic progressive buckling of circular and square tubes. *International Journal of Impact Engineering*, 4(4), 243-270.
- Abramowicz, W. (1983). The effective crushing distance in axially compressed thin-walled metal columns. *International Journal of Impact Engineering*, 1, 309-317.
- Abramowicz, W., & Jones, N. (1984a). Dynamic axial crushing of circular tubes. *International Journal of Impact Engineering*, 2(3), 263–281.
- Abramowicz, W., & Jones, N. (1984b). Dynamic axial crushing of square tubes. *International Journal of Impact Engineering*, 2(2), 179–208.
- Abramowicz, W., & Jones, N. (1997). Transition from initial global bending to progressive buckling of tubes loaded statically and dynamically. *International Journal of Impact Engineering*, 19(5-6), 415–437.
- Abramowicz, W., & Wierzbicki, T. (1989). Axial crushing of multicorner sheet metal columns. *Journal of Applied Mechanics*, 56(1), 113–20.
- Alexander, J. M. (1960). An approximate analysis of the collapse of thin cylindrical shells under axial loading. *The Quarterly Journal of Mechanics and Applied Mathematics*, 13(1), 10–15.
- Alghamdi, A. A. (2001). Collapsible impact energy absorbers: An overview. *Thin-Walled Structures*, 39, 189-213.
- Andrews, K. F., England, G. L., & Ghani, E. (1983). Classification of the axial collapse of cylindrical tubes under quasi-static loading. *International Journal of Mechanical Sciences*, 25(9-10), 687–696.
- Avitzur, B. (1964). Forging of hollow discs. *Israel Journal of Technology*, 2(3), 295-304.
- Beatty, M. F. (1987). Topics in finite elasticity: hyperelasticity of rubber, elastomers, and biological tissues—with examples. *Applied Mechanics Reviews*, 40(12), 1699-1734.
- Bhattacharyya, D., & Moltschaniwskyj, G. (1986). Measurement of anisotropy by the ring compression test. *Journal of mechanical working technology*, 13(3), 325-330.
- Bontcheva, N., & Todorov, S. (1992). Numerical investigation of plastic localization bands in aluminium rings subjected to static axial compression. *International journal of plasticity*, 8(8), 893-901.

- Carter Jr, W. T., & Lee, D. (1985). A finite element analysis of cylinder and ring compression and its experimental verification. *Computers & Structures*, 21(1-2), 1-19.
- Chahardoli, S., & Nia, A. A. (2017). Experimental and numerical investigations on collapse properties of capped-end frusta tubes with circular triggers under axial quasi-static loading. *International Journal of Mechanical Sciences*, 134, 545-561.
- Chan, W. L., Fu, W., M., & Lu, J. (2011). The size effect on micro deformation behaviour in micro-scale plastic deformation. *Materials & Design*, 32(1), 198-206.
- Chen, X. X., Wu, P. D., Lloyd, D. J., Embury, J. D., & Huang, Y. (2010). Enhanced ductility in sheet metals produced by cladding a ductile layer. *Journal of Applied Mechanics*, 77, 041015-1-7.
- Cristino, V. A., Rosa, P. A., & Martins, P. A. (2015). The role of interfaces in the evaluation of friction by ring compression testing. *Experimental Techniques*, 39(4), 47-56.
- Desalegn, W., Davidson, M. J., & Khanra, A. K. (2014). Friction Factor Evaluation Using Experimental and Finite Element Methods for Al-4% Cu Preforms. *Journal of materials engineering and performance*, 23(8), 3058-3068.
- El-Hage, H., Mallick, P., & Zamani, N. (2005). A numerical study on the quasi-static axial crush characteristics of square aluminum tubes with chamfering and other triggering mechanisms. *International Journal of Crashworthiness*, (10), 183-196.
- Eyvazian, A., Habibi, M. K., Hamouda, A. M., & Hedayati, R. (2014). Axial crushing behavior and energy absorption efficiency of corrugated tubes. *Materials & Design (1980-2015)*, 54, 1028-1038.
- Falkenreck, T. E., Klein, M., & Bollinghaus, T. (2017). Dynamic compressive behaviour of weld joints. *Material Science & Engineering A*, 702, 322-330.
- Fann, K. J., & Chen, C. C. (2017). Grain Size in Aluminum Alloy 6061 under Hot Ring Compression Test and after T6 Temper . *Applied Sciences*, 7(4), 372-390.
- Guillow, S. R., Lu, G., & Grzebieta, R. H. (2001). Quasi-static axial compression of thin-walled circular aluminium tubes. *International Journal of Mechanical Sciences*, 43(9), 2103-2123.
- Hartley, P., Sturgess, C. E., Lees, A., & Rowe, G. W. (1981). The static axial compression of tall hollow cylinders with high interfacial friction. *International Journal of Mechanical Sciences*, 23(8), 473-485.
- Hawkyard, J. B., & Johnson, W. (1967). An analysis of the changes in geometry of a short hollow cylinder during axial compression. *International Journal of Mechanical Sciences*, 9(4), 163-182.

- Hsu, S., & Jones, N. (2004). Quasi-static and dynamic axial crushing of thin-walled circular stainless steel, mild steel and aluminium alloy tubes. *International Journal of Crashworthiness*, 9(2), 195-217.
- Hu, X. H., Wu, P. D., Lloyd, D. J., & Embury, J. D. (2014). Enhanced formability in sheet metals produced by cladding a high strain-rate sensitive layer. *Journal of Applied Mechanics*, 81(2), 021007.
- Janardhana, M. N., & Biswas, S. K. (1979). Modes of deformation in aluminium rings subjected to static axial compression. *International Journal of Mechanical Sciences*, 21(12), 699-712.
- Johnson, G. R., & Cook, W. H. (1983). A constitutive model and data for metals subjected to large strains, high strain rates and high temperatures. In *Proceedings of the seventh international symposium on ballistics*, (pp. 541-547). The Hague.
- Johnson, W., & Mamalis, A. G. (1978). *Crashworthiness of vehicles*. London: Mechanical Engineering Publications Limited.
- Jones, N. (2012). *Structural Impact*. Cambridge: Cambridge University Press.
- Jones, N., & Abramowicz, W. (1985). Static and dynamic axial crushing of circular and square tubes. In: Reid SR, editor. *Metal forming and impact mechanics*. New York: Pergamon, 225-247.
- Jones, N., & Wierzbicki, T. (1993). *Structural crashworthiness and failure*. London: Elsevier Applied Science.
- Karagiozova, D., & Jones, N. (2008). On the mechanics of the global bending collapse of circular tubes under dynamic axial load—Dynamic buckling transition. *International Journal of Impact Engineering*, 35(5), 397-424.
- Kim, Y. H., Gy, Z., & Tisza, M. (1990). Theoretical and Experimental Investigation of Subcritical Superplastic Forming of Low-Alloyed Tool Steels. Theoretical and Experimental Investigation of Subcritical Superplastic FormiIn: *Proceedings of the Twenty-eighth International*, London: Palgrave Macmillan, 405-410.
- Kohar, C. P., Zhumagulov, A., Brahme, A., Worswick, M. J., Mishra, R. K., & Inal, K. (2016). Development of high crush efficient, extrudable aluminium front rails for vehicle lightweighting. *International Journal of Impact Engineering*, 95, 17-34.
- Kunogi, M. (1954). On the plastic deformation of the hollow cylinder under axial load. *Journal of The Scientific Research Institute*, 30(2), 63-92.
- Lesuer, D. R., Kay, G. J., & LeBlanc, M. M. (2001). Modeling large-strain, high-rate deformation in metals. Modeling the performane of engineering structural materials II. . In *Proceedings of a symposium sponsored by the SMD of TMS, Indianapolis*, 75-86.

- Li, F., Li, J. H., Chu, G. N., & Liu, X. J. (2010). Investigation of the diffidence mechanism of an aluminium alloy ring under compression. *Proceedings of the Institution of Mechanical Engineers, Part C: Journal of Mechanical Engineering Science*, 224(4), 771-776.
- Liu, G., Wang, L. L., Yuan, S. J., & Wang, Z. R. (2006). Compressive formability of 7075 aluminum alloy rings under hydrostatic pressure. *Transactions of Nonferrous Metals Society of China*, 16(5), 1103-1109.
- Mahbod, M., & Asgari, M. (2018). Energy absorption analysis of a novel foam-filled corrugated composite tube under axial and ablique loading. *Thin-Walled Structure*, 129, 58-73.
- Male, A. T., & Cockcroft, M. G. (1964-65). A Method for the Determination of the Coefficient of Friction of Metals under Conditions of Bulk Plastic Deformation. *Journal of the Institute of Metals*, 93, 38-46.
- Mamalis, A. G., Manolakos, D. E., Siagal, S., Viegelahn, G., & Johnson, W. (1986). Extensible plastic collapse of thin-wall frusta as energy absorbers. *International Journal of Mechanical Sciences*, 28(4), 219-229.
- Mamalis, W., & Johnson, W. (1983). The quasi-static crumpling of thin-walled circular cylinders and frusta under axial compression. *International Journal of Mechanical Sciences*, 25(9-10), 713-732.
- Meguid, S. A., Attia, M. S., Stranart, J. C., & Wang, W. (2007). Solution stability in the dynamic collapse of square aluminium columns. *International journal of impact engineering*, 34(2), 348-359.
- Mirahmadi, S. J., Hamed, M., & Cheraghzadeh, M. (2015). Investigating friction factor in forging of Ti-6Al-4V through isothermal ring compression test. *Tribology Transactions*, 58(5), 778-785.
- Mirzaie, M., Shakeri, M., Sadighi, M., & Akbarshahi, H. (2012). Experimental and analytical assessment of axial crushing of circular hybrid tubes under quasi-static load. *Journal of Composite Structure*, 94, 1959-1966.
- Morris, E., Olabi, A., & Hashmi, S. (2005). Experimental and numerical analysis of the static lateral compression of tube type energy absorbers with different indenters. *The Engineer journal*, 59(8), 505-510.
- Olabi, A. G., Morris, E., & Hashmi, M. S. (2007). Metallic tube type energy absorbers: A synopsis. *Thin-Walled Structure*, 45, 706-726.
- Postlethwaite, H., & Mills, B. (1970). Use of collapsible structural elements as impact isolators, with special reference to automotive applications. *Journal of strain analysis*, 5(1), 58-73.
- Pugsley, A. G. (1979). On the crumpling of thin tubular struts. *The Quarterly Journal of Mechanics and Applied Mathematics*, 32(1), 1-7.

- Pugsley, A. G., & Macaulay, M. (1960). The Large-scale crumpling of thin cylindrical columns. *The Quarterly Journal of Mechanics and Applied Mathematics*, 13(1), 1–9.
- Rao, K. P., & Sivaram, K. (1993). A review of ring-compression testing and applicability of the calibration curves. *Journal of Materials Processing Technology*, 37, 295-318.
- Reid, S. R. (1993). Plastic deformation mechanisms in axially compressed metal tubes used as impact energy absorbers. *International Journal of Mechanical Sciences*, 35(12), 1035–1052.
- Robinson, T., Ou, H., & Armstrong, C. G. (2004). Study on ring compression test using physical modelling and FE simulation. *Journal of Materials Processing Technology*, 153, 54-59.
- Sadeghi, M. M. (1984). Design of heavy duty energy absorbers. In G. Davies , & J. Morton, *Structural impact and crashworthiness* (pp. 588–604). New York: Elsevier.
- Sahi, M., Rahouadj, R., Herbach, R., & Choulier, D. (1996). The influence of viscoplasticity in the interpretation of the ring test. *Journal of materials processing technology*, 58(2-3), 286-292.
- Shi, Y., Wu, P. D., Lloyd, D. J., & Li, D. Y. (2014). Effect of rate sensitivity on necking behavior of a laminated tube under dynamic loading. *Journal of Applied Mechanics*, 81(5), 051010.
- Shinde, R. B., & Mali, K. D. (2018). An overview on impact behaviour and energy absorption of collapsible metallic and non-metallic energy absorbers used in automotive applications. In *IOP Conference Series: Materials Science and Engineering*, 346, 012054-1-12.
- Singh, A. P., & Padmanabhan, K. A. (1991). Axi-symmetric compression of solid cylinders. *Journal of Materials Science*, 26(20), 5481-5487.
- Sofuoglu, H., & Rasty, J. (1999). On the measurement of friction coefficient utilizing the ring compression test. *Tribology International*, 32(6), 327-335.
- Systèmes, D. (2012). Simulation of the ballistic perforation of aluminium plates with Abaqus/Explicit. *Abaqus Technology Brief*.
- Tarlochan, F., Samer, F., Hamouda, A., Ramesh, S., & Khalid, K. (2013). Design of thin wall structures for energy absorption applications: Enhancement of crashworthiness due to axial and oblique impact forces. *Thin-Walled Structures*, 71, 7-17.
- Thornton, P. H., & Magee, C. L. (1977). The interplay of geometric and material variables in energy absorption. *J. Engng Mat. Tech., Trans, ASME* 99, 114-120.
- Veganzones, M., Camacho, A. M., García-Prada, J. C., & Sebastián, M. A. (2014). Contact pressure profiles in axisymmetric compression considering friction and geometrical factors. *Procedia Engineering*, 69, 72-80.

- Webber, G., & Anand, L. (1990). Finite deformation constitutive equations and a time integration procedure for isotropic, hyperelastic-viscoplastic solids. *Computer Methods in Applied Mechanics and Engineering*, 79(2), 173-202.
- Wierzbicki, T., & Abramowicz, W. (1983). On the crushing mechanics of thin-walled structures. *Journal of Applied Mechanics*, 50(4), 727–734.
- Wierzbicki, T., & Jones, N. (1989). *Structural failure*. New York: John Wiley.
- Willis, A. H. (1948). Instability in hollow rubber cylinders subjected to axial loads. *Int. Cong. Appl. Mech. Lond*, 1, 280-296.
- Yuen, S., & Nuric, G. N. (2008). The energy-absorbing characteristics of tubular structures with geometric and material modifications: An overview. *Thin-walled Structures*, 020802-1-15.
- Zhang, D. W., Yang, H., Li, H. W., & Fan, X. G. (2012). Friction factor evaluation by FEM and experiment for TA15 titanium alloy in isothermal forming process. *The International Journal of Advanced Manufacturing Technology*, 60(5-8), 527-536.
- Zhu, Y., Zeng, W., Ma, X., Tai, Q., Li, Z., & Li, X. (2011). Determination of the friction factor of Ti-6Al-4V titanium alloy in hot forging by means of ring-compression test using FEM. *Tribology International*, 44(12), 2074-2080.